DOKUZ EYLÜL UNIVERSITY
GRADUATE SCHOOL OF NATURAL AND APPLIED SCIENCES

TESTING AND REDUCING ELECTROMAGNETIC INTERFERENCES IN SWITCHED MODE POWER SUPPLIES

by
Gökhan ÇABUK

August, 2010
İZMİR

TESTING AND REDUCING ELECTROMAGNETIC INTERFERENCES IN SWITCHED MODE POWER SUPPLIES

A Thesis Submitted to the
Graduate School of Natural and Applied Sciences of Dokuz Eylül University
In Partial Fulfillment of the Requirements for the Degree of Master of Science
in Electrical and Electronics Engineering Department

by
Gökhan ÇABUK

August, 2010
İZMİR

M. Sc THESIS EXAMINATION RESULT FORM

We have read the thesis entitled **"TESTING AND REDUCING ELECTROMAGNETIC INTERFERENCES IN SWITCHED MODE POWER SUPPLIES"** completed by **GÖKHAN ÇABUK** under supervision of **ASSIST. PROF. DR. SELÇUK KILINÇ** and we certify that in our opinion it is fully adequate, in scope and in quality, as a thesis for the degree of Master of Science.

Assist. Prof. Dr. Selçuk KILINÇ

Supervisor

(Jury Member) (Jury Member)

Prof. Dr. Mustafa SABUNCU
Director
Graduate School of Natural and Applied Sciences

ACKNOWLEDGMENTS

First I would like to express my gratitude to my advisor Assist.Prof.Dr. Selçuk Kılınç, for his support and guidance throughout my research. Also, I would like to thank VESTEL Elektronik A.Ş family for their support during my research.

I am thankful to my family for their faith in me and for their encouragement throughout my life. Special thanks to my friends in my office for their valuable support and help.

Finally, I want to thank my best friend and my beloved wife, Sinem. I would not have completed this study without her patience, support and love.

Gökhan ÇABUK

TESTING AND REDUCING ELECTROMAGNETIC INTERFERENCES IN SWITCHED MODE POWER SUPPLIES

ABSTRACT

One of the most preferable types of the switched mode power supplies (SMPS) is the flyback converter due to its wide application areas. The properties such as low cost, providing multiple output terminals, higher efficiencies make it important, hence its usage in cell phone chargers, PCs, set-top boxes, TVs, etc. increases. Due to its working principles and electromagnetic interference (EMI) performance, this type of converter requires extra care in the design process. This thesis reviews the most common methods of mitigating EMI in SMPS and discusses the spread spectrum frequency modulation (FM) technique, which is increasingly used in recent years to achieve this goal. The modulation technique that is applied to the pulse width modulation (PWM) switching signal of the flyback converter is analyzed and the effect on EMI performance is discussed. The spectrum of a frequency modulated PWM signal has theoretically been derived by using Fourier analysis. Based on the FM theory and the operation principle of the flyback converter, two application circuits have been built in this work. A 24W AC-DC flyback converter with the L6566B integrated circuit which has a dedicated FM pin, has been built as a prototype. A 5W DC-DC flyback converter that is driven by an FM modulated PWM signal has also been designed. The EMI spectrums of these two converters have been measured and test results are given. According to these results, FM technique provides better EMI performance.

Keywords: Electromagnetic compatibility (EMC), Electromagnetic interference (EMI), Flyback converter, Frequency modulation (FM), Spread spectrum technique, Switched mode power supply (SMPS).

ANAHTARLAMALI GÜÇ KAYNAKLARINDA ELEKTROMANYETİK GİRİŞİMLERİN ÖLÇÜLMESİ VE AZALTILMASI

ÖZ

Çapraz çevirici, geniş uygulama alanlarından dolayı anahtarlamalı güç kaynakları (SMPS) çeşitleri arasında en çok tercih edilenlerden biridir. Düşük güç harcaması, düşük maliyet oranı, birden fazla çıkış gerilimi vermesi gibi özellikleri önem kazandırmış, bu nedenle cep telefonu şarj aletleri, bilgisayarlar, masa üstü set cihazları, televizyonlar gibi birçok alanda kullanılırlığı artmıştır. Bu tip çeviriciler, çalışma prensipleri ve elektromanyetik girişim (EMI) performansından dolayı tasarım esnasında fazladan dikkat gerektirirler. Bu tez SMPS'lerdeki EMI'yi azaltma yöntemlerini incelemekte ve son dönemlerde yaygın olarak kullanılan yayılmış spektrum frekans modulasyonu (FM) tekniğini tartışmaktadır. Çapraz çeviricinin darbe genişlik modulasyonlu (PWM) anahtarlama sinyaline uygulanan modulasyon tekniği analiz edilmiş ve EMI performansı üzerine etkileri araştırılmıştır. FM uygulanmış PWM sinyalinin spektrumu Fourier analizi kullanılarak teorik olarak hesaplanmıştır. FM teorisi ve çapraz çevirici çalışma prensipleri esas alınarak iki adet uygulama devresi tasarlanmıştır. FM ucu bulunan L6566B entegre devresi kullanılarak 24W'lık bir AC-DC çapraz çevirici tasarlanmıştır. Frekans modulasyonlu PWM sinyali ile sürülen 5W'lık bir DC-DC çapraz çevirici de tasarlanmıştır. Bu iki çeviricinin EMI spektrumu ölçülmüş ve test sonuçları verilmiştir. Bu sonuçlara göre FM tekniği daha iyi EMI performansı sağlamıştır.

Anahtar sözcükler: Elektromanyetik uyumluluk (EMC), Elektromanyetik girişim (EMI), Çapraz çevirici, Frekans modulasyonu (FM), Yayılmış spectrum tekniği, Anahtarlamalı güç kaynağı (SMPS).

CONTENTS

Page

CHAPTER ONE
INTRODUCTION

In recent years the energy requirements increase because of the rapid improvement of the technology. The most important part of the required energy is occupied by the electrical energy. Despite of the limited electrical energy sources the number of devices that use this energy increase. So, the efficient usage of the existing electrical energy is the most important subject nowadays. As a result devices are started to be designed in order to get higher efficiencies. As the technology improves the usage of the electrical energy by the basic loads is replaced with the complex loads such as the switched drivers, AC to DC converters, etc. Thus, the power supply requirements are tended to fulfill by the use of switched mode power supplies (SMPS) instead of using the linear power supplies.

AC-DC and DC-DC SMPS have been preferred in many systems due to their advantages of higher frequency switching property. High frequency switching reduces the size of the components, the weight of the transformer and increases the efficiency in comparison with the linear power supplies (Kaewchai, Khangern, &Nitta, 2002; Nagrial, & Helany, 2001). On the other hand, switching current on and off increases the efficiency whereas it generates conducted and radiated electromagnetic interference (EMI) (Antonini, Cristina, & Orlandi, 1996; Balcells, et al., 2005). Generation of the conducted emission and radiated emission are the undesirable features of these converters. If they are not mitigated, EMI currents and voltages can corrupt the power source to the converter and interfere with the operation of other adjacent equipments supplied from the same source (Mweene, 2006). They might constitute unexpected operating conditions for these equipments. In order to prevent this situation, the EMI noise limits are determined for the converters. EMI noises of the designed converters must be in these limits determined by the regulatory institutions such as the International Special Committee on Radio Interference (CISPR) which is a special committee under the sponsorship of the International Electrotechnical Commissions (IEC).

1.1 Literature Review

Most pulse width modulation (PWM) converters are designed to switch at a fixed frequency with a variable duty cycle. The main source of EMI in power converters comes from the switching of the voltage and current (Mweene, 2006). Electrical transitions with sharp edges produce electromagnetic radiation. The sharp edge transients contain most of the frequency components. The most significant contributions to the EMI spectrum are at the fundamental switching frequency and its harmonics (Balcells, et al., 2005).

EMI is linearly proportional to current, the area of the current loop, and with the square of frequency. EMI is defined as EMI = $k \; I \; A \; f^2$, where I is the current, A is the loop area, f is the frequency, and k is the constant depending on PCB materials and other factors (Katrai, & Arcus, 1998, s. 59).

As pointed out above, EMI can be classified into two categories as conducted EMI and radiated EMI. The conducted EMI noise consists of two modes; differential mode (DM) and common mode (CM) (Chen, & Qian, 2004). In all circuits both CM and DM currents are present. Both types of current determine the amount of radio frequency energy propagated between circuits and radiated into space. However, there is a significant difference between these two types. DM signals carry data or a signal of information. DM mode interference is the EMI noise present on the phase line reference to the neutral due to the DM current. CM is an undesired side effect from DM transmission and is most troublesome for electromagnetic compatibility (EMC). CM interferences are EMI noise present on the line and neutral referenced to ground due to CM current. These currents has a path from the leakage capacitance between the line and reference ground. Most noise problems are caused by this mode (Montrose, & Nakauchi, 2004).

In order to attenuate EMI by the time they reach the power source, the switching currents are low-pass filtered by the input capacitor and input EMI filter. This is the most common method used (Çadirci, Saka, & Eristiren, 2005). However most of the time the filtering is not perfect, and often leaves enough residual switching currents to cause the system to fail conducted EMI tests (Mweene, 2006). To greatly improve the conducted EMI performance of the system, a filter is used with larger component values or more complexity, but these measures usually increase the weight of the devices and the filter's cost.

Some EMI reduction methods have been proposed in the past. Sigma-delta (ΣΔ) modulation is proposed as an alternative switching technique to reduce conducted EMI in SMPS. The result of using ΣΔ modulation is a spread in the spectrum of the conducted emissions so that large concentrations of power at discrete frequencies are avoided (Paramesh, & Jouanne, 2001). It has the advantage of being a synchronous switching scheme which could be exploited in resonant converters.

Son, & Seung (2006) analyzed and generalized the active filters used for EMI reduction. Insertion loss and input impedance of various types of active-filter topologies are described with applicable requirements and limitations. An appropriate topology of an active filter for a specific application can be selected.

The use of soft switching techniques allows a reduction of conducted noise. Soft-switching technique provides a useful solution to reduce EMI emission from SMPS (Chung, Hui, & Tse, 1998). The soft-switched circuits are similar to their hard-switched counterparts, except that they consist of extra resonant components and an auxiliary switch. Also they are unsuitable for suppressing conducted EMI caused by switching frequency related emissions.

Resonance technique is also used for reduction of EMI from SMPS (R. Bera, J. Bera, Sen, & Dasgupta, 1999). Resonant technology drastically reduces the switching losses and removes 30 to 40 % of losses within a comparable PWM type SMPS. The designer can then increase the operating frequency in order to reduce the component sizes. As a result, SMPS with high operating frequency adds advantage of significant reduction in ripple and EMI.

Katzir, & Singer, (2006) has presented a method of CM EMI reduction, based on a negative feedback which implies compensating current flow. More specifically, desired EMI reduction in the family of isolated DC-DC converters is achieved by means of a compensating transformer winding and a capacitor.

An anti phase technique is presented to suppress the common mode noise in boost converter. However, an additional second winding of the boost inductor and an additional mosfet must be used, which increases the cost of the converter (Kchikach, WU Xin, Qian, & Pang, 2001).

The node pair with the dynamic potential balance has been constructed to suppress the CM noise; however, it is difficult to apply to the circuit (Sheng, & Qian, 2002).

These approaches are important steps in dealing with the conducted EMI issue. One powerful method to reduce the EMI is the frequency modulation (FM) technique which modulates the switching signal and spreads the energy over a wider frequency range. In FM technique, the energy of each harmonic is spread into a band of frequencies, giving a wider spectrum with lower amplitudes (Balcells, et al., 2005). By using this method, the frequency of the switching signal is modulated and the EMI noise is reduced in SMPS.

1.2 Thesis Outline

In this thesis, FM technique is investigated as the EMI reduction method in SMPS. The frequency spectrum of an FM modulated PWM signal is derived by using Fourier analysis. Some theoretical simulations are achieved in order to examine the FM basics. The FM technique is applied to the switching signal of an AC-DC and a DC-DC flyback converter. A 24W AC-DC flyback converter with the L6566B integrated circuit has been built as a prototype which has a dedicated FM pin allowing the designer to modulate the switching frequency and hence reducing the peak value of EMI by means of spread spectrum technique. Also, a 5W DC-DC flyback converter that is driven by an FM modulated PWM signal has been designed. A signal generator is used in order to modulate the switching signal and the frequency spectrum of this power converter is measured with a spectrum analyzer. The EMI performances of each converter are tested and the results are presented. The FM scheme is compared with the standard fixed frequency switching scheme and spectral performances show that FM technique has better EMI suppression than the fixed frequency scheme.

This thesis is organized as follows. The EMI and EMC concepts are described in Chapter 2. Basic EMC standards are also given in this chapter. The operating principles of the SMPS and flyback converter are pointed out in Chapter 3 together with the related EMI issues. FM theory is presented in Chapter 4 and frequency spectrum of an FM modulated PWM signal is obtained. The operation and the EMI performance of the AC-DC converter are presented in Chapter 5. Chapter 6 introduces the design of the DC-DC flyback converter and the measurement of the conducted emission noises from it. Conclusions are drawn in Chapter 7.

CHAPTER TWO
ELECTROMAGNETIC INTERFERENCE AND COMPATIBILITY

There are various complex systems in the environment, which can produce electrical noises during their operation; therefore they can cause potential problems with EMI. EMI consists of any unwanted conducted or radiated signals of electrical origin that can cause degradation in equipment performance. In order not to have performance problems, all components must comply with specifications to ensure EMC and there are numerous design methods that can be used to prevent EMI (Tran, 1999).

EMC has become more important over the past two decades. Europe required a reduction in the level of the radiated and conducted emission in products to be sold in the region in the mid 90s. After that, the products have been designed to comply with EMC standards and testing the products for EMC have become compulsory in those countries.

2.1 Electromagnetic Interference (EMI)

Electrical and electronic products often generate radio-frequency (RF) energy. Every device has the potential of causing unintentional interference to other electrical devices. EMI is the process by which disruptive electromagnetic energy is transmitted from one electronic device to another via radiated or conducted paths (Montrose, & Nakauchi, 2004). The phenomena that we face in our daily life such as clipping on the computer monitors when the light is on, resetting digital display on the video device when the air conditioner starts to run, locking the ABS in the cars when the mobile phone rings, etc. are the effects of the EMI.

Three essential elements must exist for EMI to occur: An electrical noise (EMI) source, a coupling path and a victim receptor. Coupling path of EMI can be classified in two categories, radiated and conducted. Coupling can also result from a combination of both two paths. The various mechanisms in which EMI can travel from its source to the receptor are illustrated in Figure 2.1. Path 1 shows the direct radiation from source to receptor so called radiated coupling. Path 2 shows the direct radiation (radiated coupling) from source picked up by the electrical power cables or the signal cables connected to the receptor, which reaches the receptor via conduction. Path 3 shown in Figure 2.1 represents the EMI radiated (radiated coupling) by the electrical power, signal, or control cables of the source. EMI directly conducted (conducted coupling) from its source to the receptor via common electrical power supply lines or via common signal/control cables is the path 4 (Montrose, & Nakauchi, 2004).

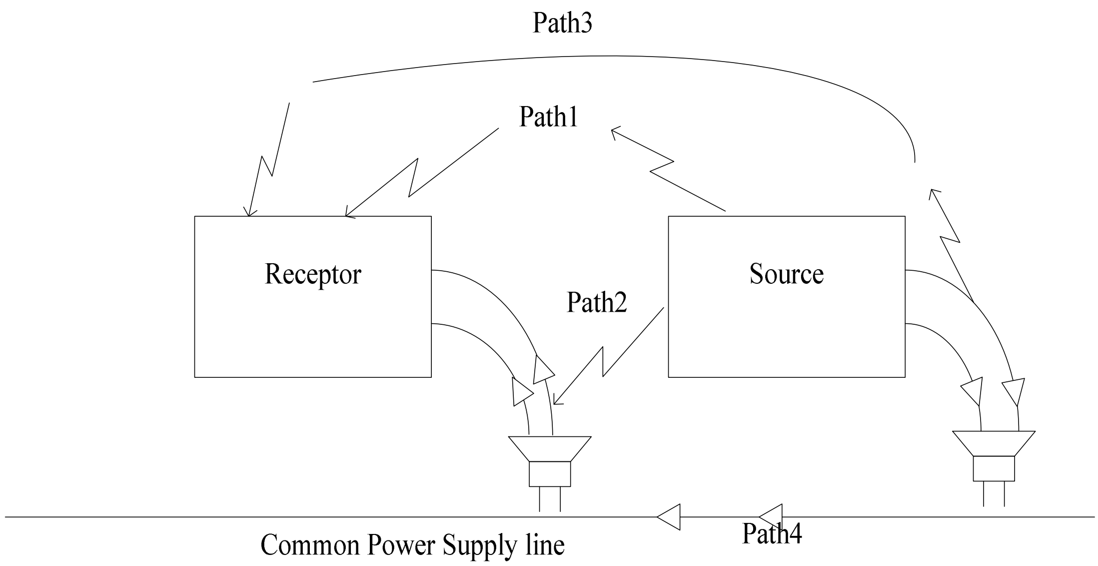

Figure 2.1 Coupling paths of EMI.

In addition to the four primary coupling paths, there are four transfer mechanisms that exist for each path: Conductively (electric current), magnetic field dominant (inductive coupled), electric field dominant (capacitive coupled), electromagnetic field. Conductively coupling is the process of conducting the noise to another circuit via a conductor which picks up the noise while running through a noisy environment. The common example of this coupling is the interference between systems plugged in to the same power supply. Magnetic coupling occurs when a portion of magnetic flux created by one current loop passes through the flux pattern of a second loop formed by another current path. The current flowing in a conductor (source) creates a magnetic flux which will couple with a nearby conductor hence induces a noise voltage in the victim circuit. Magnetic flux coupling exists due to mutual inductance between the two loops shown in Figure 2.2 (Montrose, & Nakauchi, 2004; Williams, 1996).

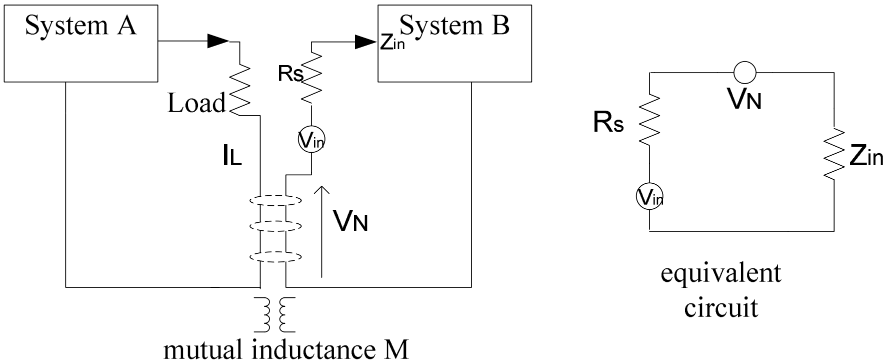

Figure 2.2 Magnetic field coupling and its equivalent circuit.

Changing voltage on one conductor (source) creates an electric field which may couple with a nearby conductor (victim) hence induces a voltage on it. Electric field coupling is capacitive as shown in Figure 2.3 and can be modeled as a noise current source that is produced between the victim and its ground (Williams, 1996). Electromagnetic field coupling is a combination of both magnetic and electric fields affecting a circuit simultaneously. Depending on the distance between source and receptor, the electric field and magnetic field may be operatively dominant, depending on whether we are in the near field or far field. This is the most common transfer mechanism observed by measurement with an antenna (Montrose, & Nakauchi, 2004).

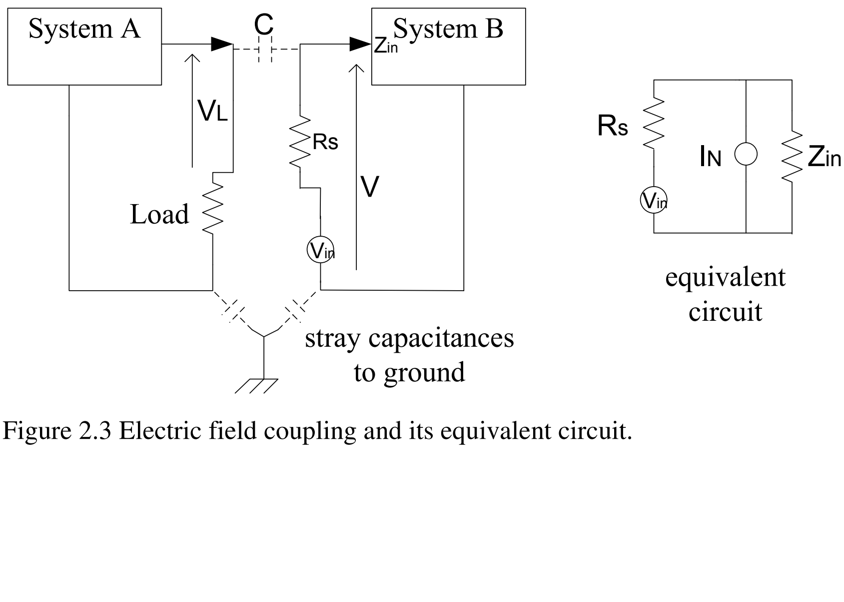

Figure 2.3 Electric field coupling and its equivalent circuit.

2.1.1 Common Mode vs. Differential Mode Currents

As pointed out above, EMI can be in the form of radiated or conducted. The radiated and conducted EMI noises can be generated by either differential mode (DM) currents or common mode (CM) currents flow. In all circuits both CM and DM currents are present. Both types of current determine the amount of RF energy propagated between circuits or radiated into free space (Montrose, & Nakauchi, 2004).

If the interference currents propagate from a source to a receptor through a conductor such as transmission line, AC mains power cable, data lines then conducted interference occurs. Conducted interference can be caused by DM currents or CM currents. The DM current is the RF noise between wires that goes from signal lines to the neutral connections without reference to earth connection in the circuit and cause EMI if there is an unbalanced between signal paths. DM emissions are generally associated with low frequency switching noise from the power supply. The CM current is RF noise between line/neutral and chassis ground and causes EMI due to the parasitic element in the line. Because of the higher frequency switching components, CM emission occupies in the circuit (Montrose, & Nakauchi, 2004).

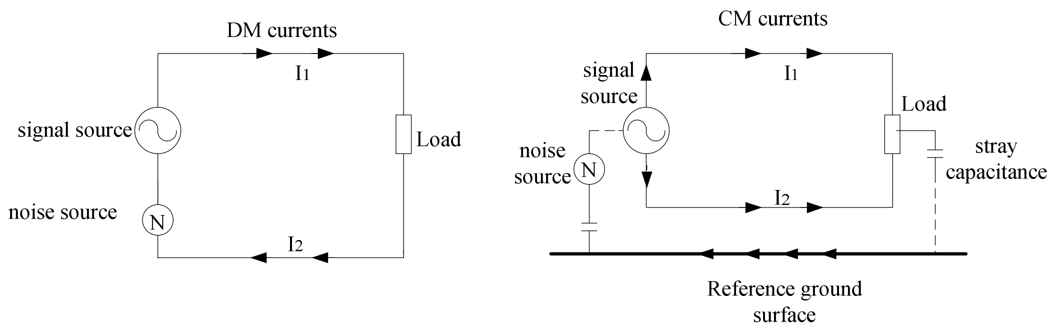

Figure 2.4 Differential and common mode currents.

If the electric and magnetic fields are transmitted through space from source to receptor then radiated interference emanates. Radiation from electrical circuits also occurs due to the DM and CM currents. DM radiation is the result of current flowing around loops formed by the conductors of the circuit as shown in Figure 2.5. For a small-loop receiving antenna operating in an open field over a ground plane, the radiation from product is described approximately as (Ott, 1988).

$$E = 263x10^{-16}(f^2 AI_s)(\frac{1}{r}) \text{ V/m} \tag{2.1}$$

where A is the area (m^2) of small loop that is carrying current I_s in amperes and r is the distance (m) from radiating element to receiving antenna and f is the frequency of current in Hz.

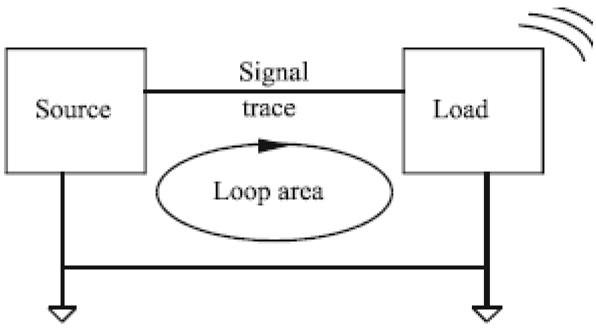

Figure 2.5 Loop area between components.

The maximum loop area that will not exceed a specific emission level is described by Equation 2.2. (Ott, 1988)

$$A = \frac{380rE}{f^2 I_s} \tag{2.2}$$

where E is the radiation limit in µV/m, r is the distance between loop and measuring antenna in meters, f is the frequency in MHz, I_s is the current in mA, A is the loop area in cm^2.

CM radiation originates from the cables in the system. The model for the cable radiation at lower frequencies is a short monopole antenna over a ground plane. The maximum field strength is described as (Ott, 1988 & Williams, 1996)

$$E \approx \frac{1.26\times10^{-7}(fI_{CM}L)}{r} \quad \text{(V/m)} \tag{2.3}$$

where L is the antenna length in meters, I_{CM} is the common-mode current in amperes, f is the frequency of current in Hz, r is the distance in the field in meters.

2.2 Electromagnetic Compatibility (EMC)

EMC is the branch of engineering, which studies the operation of equipment in their electromagnetic environment. EMC is the capability of electrical and electronic systems, equipment, and devices to operate in their intended electromagnetic environment within a defined margin of safety and at design levels or performance without suffering or causing unacceptable degradation as a result of EMI (American National Standards Institute (ANSI) C64.14, 1992; Montrose, & Nakauchi, 2004).

There are two main groups of measurements in order to determine the EMC of the systems: Emission and Immunity. Emission measurement determines whether the system works without producing EMI level which leads to malfunction or faulty operation of any other devices or not. Immunity is a relative measure of a device or system’s ability to withstand EMI exposure while preserving a predefined performance level (Montrose, & Nakauchi, 2004).

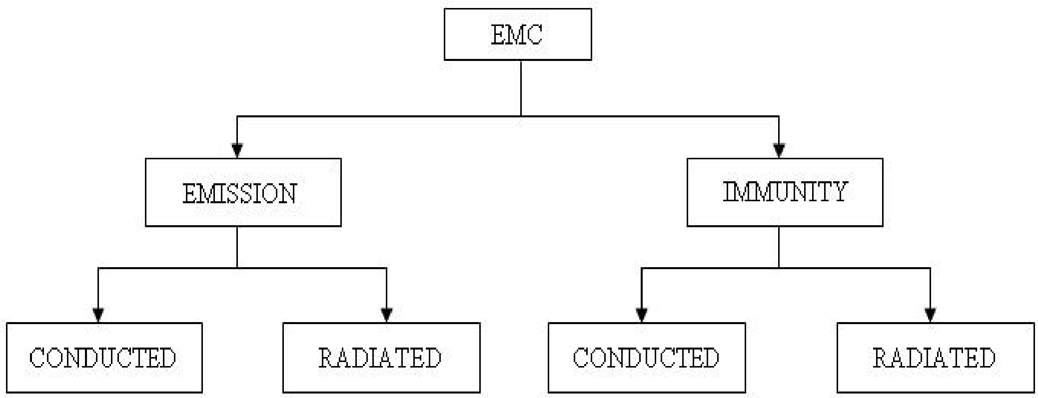

Figure 2.6 EMC test contents.

EMC has standards that must be followed and regulated by the IEC and CISPR. There are three main points for the EMC test: Firstly, the standard which the device is supervised must be known. Secondly, it must be known what functions device have during the test procedure. Lastly, test must be done and measurements should be taken according to the standards.

In order to design an EMI compliant device, all EMI sources should be suppressed enough, coupling paths should be reduced and immunity of this design should be strong enough to work in the noisy environment. In order to meet the EMC requirements, immunity of the device should be strong as much as not to be affected by the EMI coming from the environment and EMI that it emits should not cause any failure at the performance of the other devices.

Basic emission standards are listed below:

- EN 55011 – Industrial, scientific and medical;
- EN 55013 – Broadcast receivers;
- EN 55014 – Household appliances;
- EN 55015 – Lighting apparatus;
- EN 55022 – Information Technology Equipment.

Basic immunity standards are as listed below:

- EN 55020 – Broadcast receivers;
- EN 61000-4-2 – Immunity to electrostatic discharge
- EN 61000-4-3 – Radiated immunity;
- EN 61000-4-4 – Immunity to electrical fast transient (EFT)/Burst;
- EN 61000-4-5 – Immunity to surge;
- EN 61000-4-6 – Conducted RF immunity;
- EN 61000-4-8 – Power frequency magnetic immunity;
- EN 61000-4-11 – Voltage dips and interruptions.

CHAPTER THREE
ELECTROMAGNETIC INTERFERENCES IN SMPS

3.1 Switched Mode Power Supplies (SMPS)

The industry has divided into areas where linear and switching power supplies are employed. An SMPS is an electronic power supply unit that the energy flow is controlled with semiconductors that are continuously switching on and off at high frequency. A linear power supply contains a main transformer and a dissipative series regulator to provide the proper output energy. The choice of whether to use an SMPS or a linear power supply in a design is based on the needs of the application. In order to use the more appropriate power supply type in a particular design, it is necessary to understand the electrical requirement and the cost of the entire product and select the type of the power supply that best satisfies the requirements. However, the SMPS has advantages compared to the linear power supply. The main drawbacks of the linear power supply are having an extremely large and heavy 50/60 Hz transformer, very poor power conversion efficiency and heating problem during the typical operating condition. The SMPS has overcome all of these shortcomings. The energy stored by an inductor in an SMPS can be converted to output voltages that can be greater than the input, to negative voltages, or can even be transferred through a transformer to provide electrical isolation with the input. Additional windings can be added to the transformer to provide more than one output voltage. Higher switching frequency in SMPS reduces the size of the transformer and other energy storage elements hence the cost and weight of the system reduce in comparison to linear power supply. Since less energy is lost in the transfer, less thermal management is required. There are admittedly some drawbacks of the SMPS. Radiation and conduction of noise due to the switching of the voltage and current require extra care during the design process and make the design more complicated (Brown, 1990).

In summary, because of its high efficiency, low power dissipation, lower heat generation, small size and low cost, power supply design has seen a gradual movement away from the use of linear power supply to the more practical SMPS (Ham, Hammerton, & Sharples, 1994).

3.2 Operation of an SMPS

The AC supply is first rectified and then filtered by the input capacitor to produce a rough dc input supply which can fluctuate in time due to variations in AC mains. The capacitance on the rectification circuit has to be large to hold up the supply in case of an unexpected drop in the AC mains. The SMPS can also be configured to operate from any suitable DC input; in this case the supply is called a DC-DC converter. The block diagram of an SMPS is shown in Figure 3.1 (Ham, Hammerton, & Sharples, 1994).

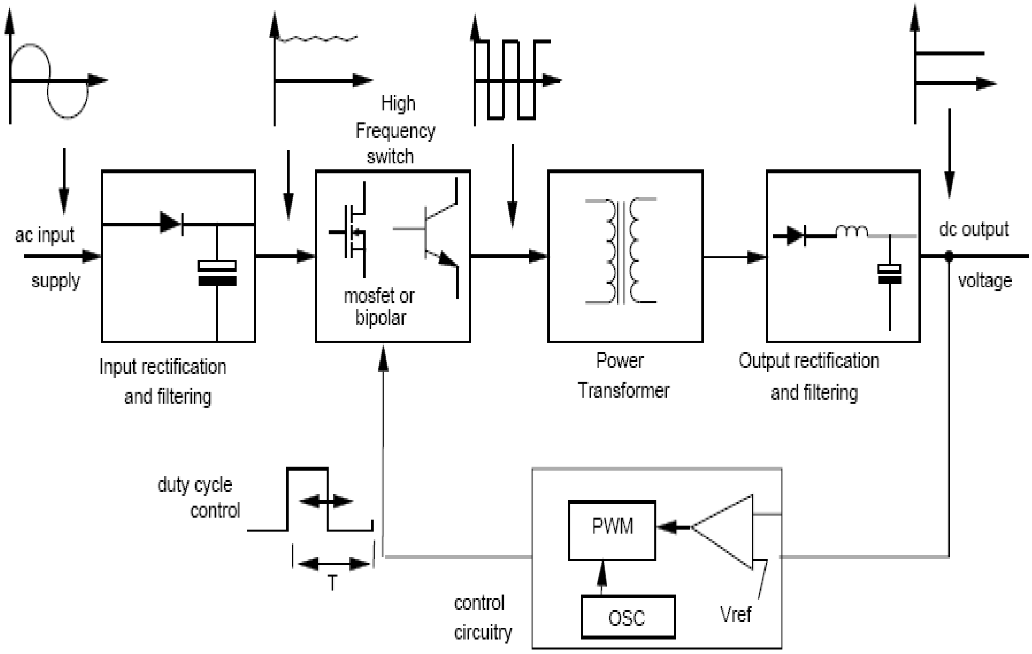

Figure 3.1 Block diagram of an SMPS.

High frequency power switching part is supplied by the unregulated DC voltage. Fast switching devices such as MOSFETs are driven on and off, and input voltage is switched across the primary side of the transformer. The drive pulses are normally fixed frequency and variable duty cycle related with the load. Hence, a voltage pulse train of suitable magnitude and duty cycle appears on secondary side of the transformer. The resultant output voltage is appropriately rectified, and then smoothed by the output filter, which is either a capacitor or capacitor/inductor arrangement, depending upon the topology used. This transfer of power from primary to secondary has to be carried out with the lowest losses possible, to obtain higher efficiency. Thus, optimum design of the passive and magnetic components, and selection of the correct switching component is critical (Ham, Hammerton, & Sharples, 1994).

Feedback or control block carries out the regulation of the output to provide a stabilized DC supply. Generally, most SMPS systems operate on a fixed frequency PWM basis. The output voltage is compared to an accurate reference supply, and the error voltage produced by the comparator is used by the dedicated control logic to produce a drive train to control the power switch. Correctly designed, this will provide a very stable DC output supply. An opto-isolator is used in the feedback to keep the isolation between primary and secondary sides (Ham, Hammerton, & Sharples, 1994).

In most applications, the SMPS topology contains a power transformer. This provides isolation, voltage scaling through the turns ratio and the ability to provide multiple outputs. Flyback, forward, push-pull, half-bridge and full-bridge converters are the isolated types of SMSP. However, there are non-isolated topologies (without transformers) where the power processing is achieved by inductive energy transfer alone. Non-isolated converter types are buck, boost and buck-boost converters (Ham, Hammerton, & Sharples, 1994). Figure 3.2 shows the approximate range of usage for the converters.

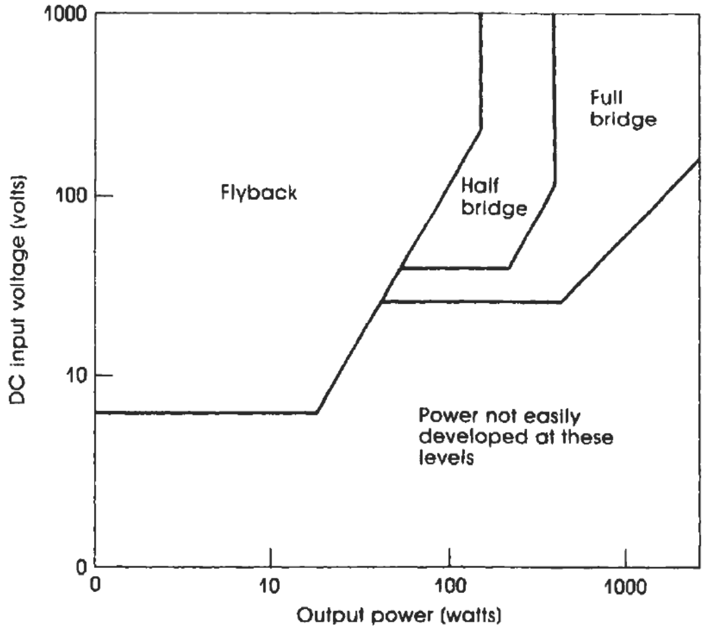

Figure 3.2 SMPS power limits due to their usage areas (Brown, 1990).

In this thesis the flyback converter which is an isolated type, is used. Working principle of the flyback converter is revealed in the following subsection.

3.2.1 Flyback Converter

Flyback converter is one of the most commonly used SMPS type for low cost and low output voltage applications in the power range from about less than 5W to 100W. The output voltage needs to be isolated from the input mains supply. Input to the circuit is generally unregulated DC voltage obtained by rectifying the utility AC voltage followed by a simple capacitor filter. The circuit can be designed for single or multiple isolated output voltages and can operate over wide range of input voltages (Lecture Notes, EE IIT). Figure 3.3 shows the basic topology of the flyback converter.

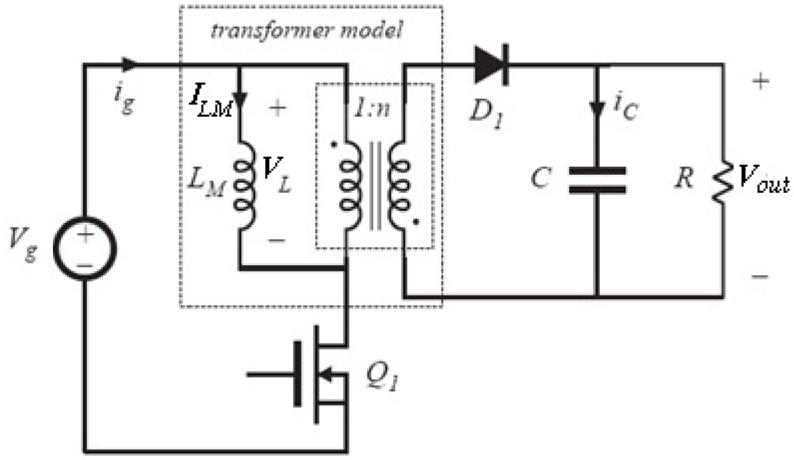

Figure 3.3 Flyback converter topology.

A fast switching MOSFET (Q1) is controlled by PWM signal to obtain the desired output voltage. The transformer is used as an energy storage element and for voltage isolation. Since primary and secondary windings of the flyback transformer do not carry current simultaneously they are more like two magnetically coupled inductors (Lecture Notes, EE IIT). The secondary side of the flyback converter is occupied by a diode and a capacitor which rectifies and filters the secondary winding voltage. As shown in Figure 3.3, voltage across this filter capacitor is the output voltage of the flyback converter.

A controller circuit also exists in the converter in order to determine the duty cycle of the PWM. A feedback voltage taken from one of the dedicated secondary outputs helps to the controller circuit for the PWM duty cycle. A snubber circuit is required to dissipate the energy stored in the leakage inductance of the primary winding when switch Q1 is turned off (Lecture Notes, EE IIT).

There are two different operation modes for the flyback converter: Continuous mode, discontinuous mode. In discontinuous mode, the secondary current falls to zero in each switching period, and all of the energy is removed from the transformer. In continuous mode, there is current flowing in the coupled inductor at all times, resulting in trapezoidal current waveforms. The complete analysis of the flyback converter can be made by dividing its operations into two parts where the position of switch is on and off.

When the switch Q1 is on, the converter circuit model reduces to Figure 3.4. The primary winding of the transformer gets connected to the input supply hence its dotted end is connected to the positive side. At this time the diode connected in series with the secondary winding gets reverse biased due to the induced voltage in the secondary (dotted end potential being higher). Thus, primary winding is able to carry current I_{Lm}, but current in the secondary winding is blocked due to the reverse biased diode (Lecture Notes, EE IIT).

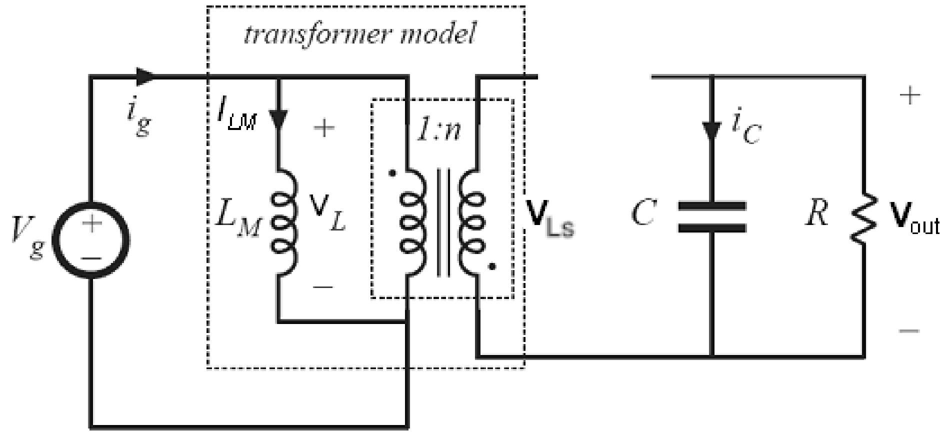

Figure 3.4 During the on time, the output capacitor supplies the load on its own.

At this mode, the input supply voltage appears across the primary winding inductance and the primary current rises linearly. The current in the primary winding increases at a rate defined by (Akpınar, Lecture Notes)

$$V_g = V_L = L_m \frac{dI_{L_m}}{dt} \tag{3.1}$$

where V_g is the mains supply voltage, V_L is the voltage of the primary winding, I_{Lm} is the primary windings current.(I_{Lm}=I_g)

$$\frac{dI_{L_m}}{dt} = \frac{\Delta I_{L_m}}{\Delta t} = \frac{\Delta I_{L_m}}{T_{on}} = \frac{V_g}{L_m} \tag{3.2}$$

where T_{on} is on time of the switch. Then current change on primary winding during on time,

$$(\Delta I_{L_m})_{on} = \frac{V_g}{L_m} T_{on} \tag{3.3}$$

During T_{on} time there is no current flowing in the secondary winding. Because of the winding dot configuration the current enters the dotted terminal of the primary side and should leave the dotted terminal of the secondary side as well. The dot arrangement on the transformer makes the diode anode swing negative, thus blocking it.

$$V_{Ls} = V_g \frac{N_s}{N_p} \tag{3.4}$$

$$V_{diode} = -V_{out} - V_g \frac{N_s}{N_p} < 0 \tag{3.5}$$

where N_p and N_s are the number of turns of the primary and secondary side of the transformer, V_{Ls} is the voltage produced on the secondary windings, V_{out} is the output voltage of the converter, V_{diode} is the voltage across the terminals of the diode located at the secondary side.

When the PWM controller instructs power switch to turn off, the voltage across the primary inductor suddenly reverses, in an attempt to keep the ampere-turns constant. The voltage developed across L_m, now appears in series with the input voltage, forcing the switch terminal V_{ds} voltage to jump to

$$V_{ds} = V_g - V_L \tag{3.6}$$

$$V_{ds} = V_g + V_{out} \frac{N_p}{N_s} \tag{3.7}$$

The diode now senses a positive voltage on its anode and it conducts. One n^{th} of voltage also appears on the primary side, across the primary inductor L_m. The voltage flies back across the transformer during the off time, hence the name is flyback. Therefore, the output voltage becomes equal to the negative of V_{Ls}.

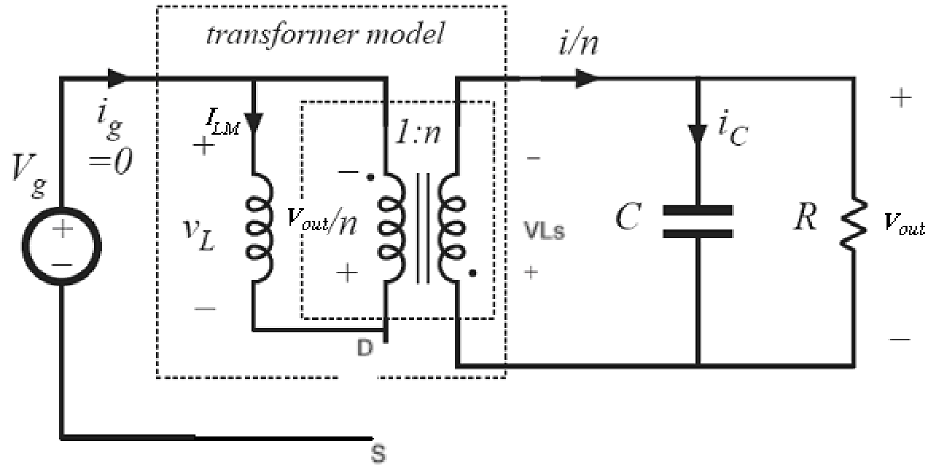

Figure 3.5 The flyback topology during the off time.

$$V_{Ls} = -V_{out} \tag{3.8}$$

$$\frac{dI_{L_m}}{dt} = \frac{\Delta I_{L_m}}{\Delta t} = -\frac{V_{out}}{L_m}\frac{N_p}{N_s} \tag{3.9}$$

$$(\Delta I_{L_m})_{off} = -\frac{V_{out}}{L_m}\frac{N_p}{N_s}T_{off} \tag{3.10}$$

During one switching period of the continuous mode operation, the change of current must be zero. So by combining Equations (3.3) and (3.10);

$$(\Delta I_{L_m})_{on} + (\Delta I_{L_m})_{off} = 0 \tag{3.11}$$

$$\frac{V_{out}}{L_m}\frac{N_p}{N_s}T_{off} = \frac{V_g}{L_m}T_{on} \tag{3.12}$$

$$\frac{V_{out}}{V_g} = \frac{N_s}{N_p}\frac{T_{on}}{T_{off}} \tag{3.13}$$

Expressing duty cycle D in relation to the on and off time $D=T_{on}/T_{on}+T_{off}$, the Equation 3.13 reduces to

$$\frac{V_{out}}{V_g} = \frac{N_s}{N_p}\frac{D}{1-D} \tag{3.14}$$

The current of the flyback at the secondary side when the switch is off;

$$I_{diode} = I_{L_m}\left(\frac{N_p}{N_s}\right) \tag{3.15}$$

The average current that is supplied from the source for the continuous current mode is

$$I_g = I_{L_m} D \tag{3.16}$$

The total power that goes the secondary side is given by;

$$V_g I_g = V_g I_{L_m} D = \frac{V_{out}^{\;2}}{R} \tag{3.17}$$

By using Equation (3.14) and (3.17), following relation is obtained.

$$I_{L_m} = \frac{V_{out}}{(1-D)R} \frac{N_s}{N_p} \tag{3.18}$$

The maximum and minimum of the primary side inductance current can be found as

$$I_{L_m,\max} = I_{L_m} + \frac{\Delta I_{L_m}}{2} \text{ and } I_{L_m,\min} = I_{L_m} - \frac{\Delta I_{L_m}}{2} \tag{3.19}$$

For discontinuous mode the average current supplied from the source is

$$I_g = \frac{1}{T_{on} + T_{off}} \int_0^{T_{on}} \frac{V_g}{L_m} t dt = \frac{1}{T_{on} + T_{off}} \frac{V_g}{2L_m} T_{on}^2 \tag{3.20}$$

The total power that is transferred to the secondary side is given by;

$$V_g I_g = \frac{V_{out}^{\;2}}{R} \tag{3.21}$$

then V_{out} is found as

$$V_{out} = V_g D \sqrt{\frac{(T_{on} + T_{off})R}{2L_m}} \tag{3.22}$$

Figures 3.6 and 3.7 show the discontinuous and continuous mode waveforms of the converter.

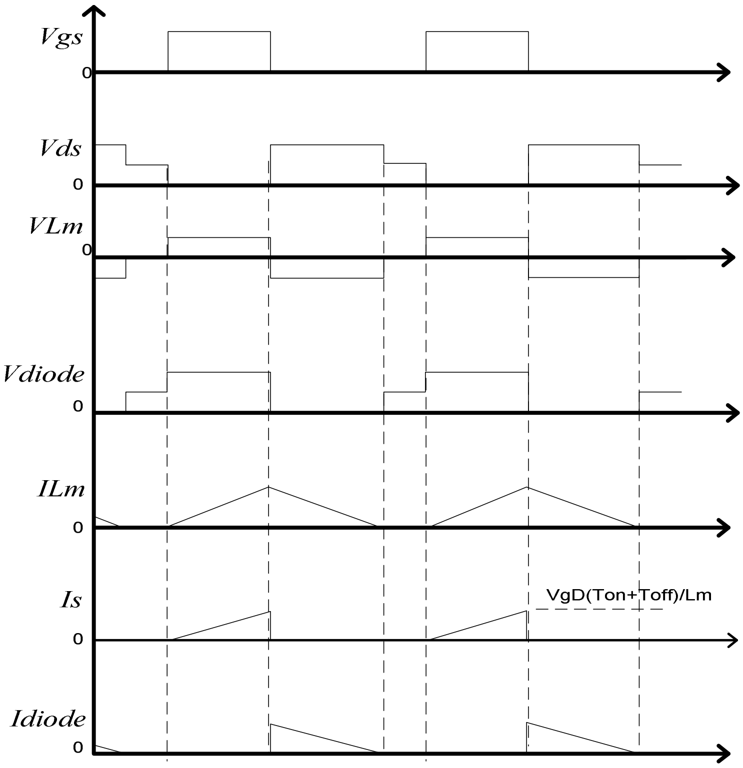

Figure 3.6 The discontinuous mode waveforms. The inductor current becomes zero during switching cycle.

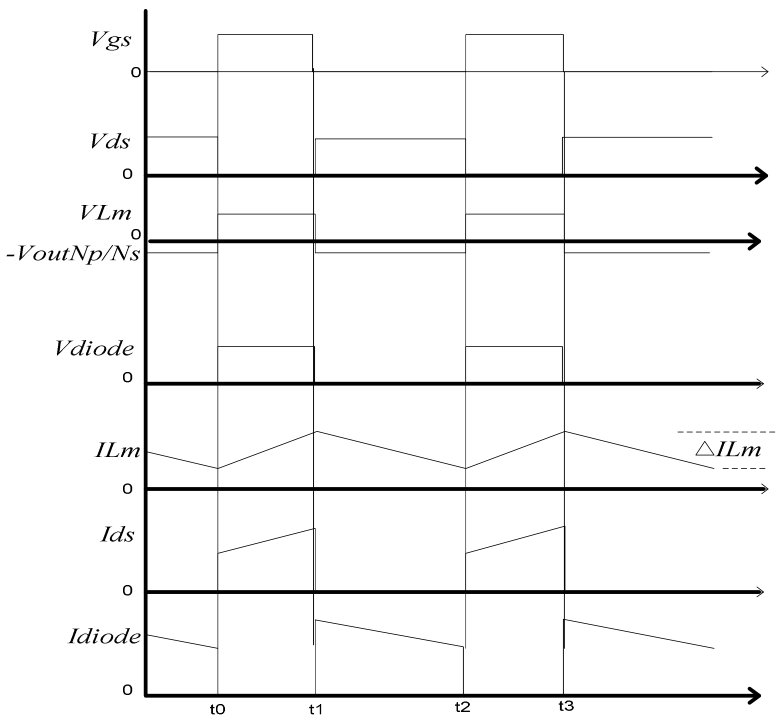

Figure 3.7 The continuous mode waveforms. The current on the inductor always greater than zero.

3.2.1.1 General Consideration of Control Mechanism

In order to adjust the required output voltage and power for the load, the duty cycle of the PWM signal is modified by a control circuit. This circuit produces a switching algorithm at the constant frequency by adjusting the on and off time duration of the switching to control the average output voltage. The control voltage V_c is generated by amplifying the error signal which is the difference between the actual voltage and its desired value that is obtained by taking one of the secondary output voltages as a reference. By comparing the sawtooth signal with the control voltage (Figure 3.8), a PWM signal with the frequency of the sawtooth is produced whose duty cycle is determined by the ratio;

$$D = \frac{T_{on}}{T} = \frac{V_c - V_L}{V_H - V_L} \tag{3.23}$$

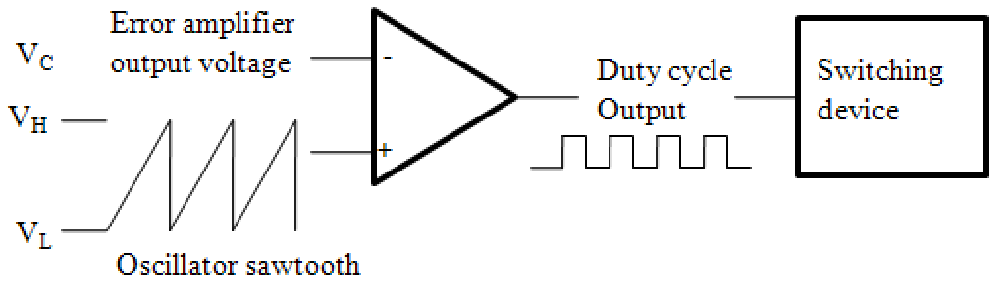

Figure 3.8 Control mechanism block diagram.

where $T=T_{on}+T_{off}$ and, V_H and V_L is the maximum and minimum voltages levels of the sawtooth signal, respectively.

The output voltage of the comparator is high during the time where control voltage is higher than the voltage level of the sawtooh signal, hence the switching component of the controller conducts. Figure 3.9 shows the resulted PWM signal by comparing the sawtooh signal with a control signal which has variable voltage levels.

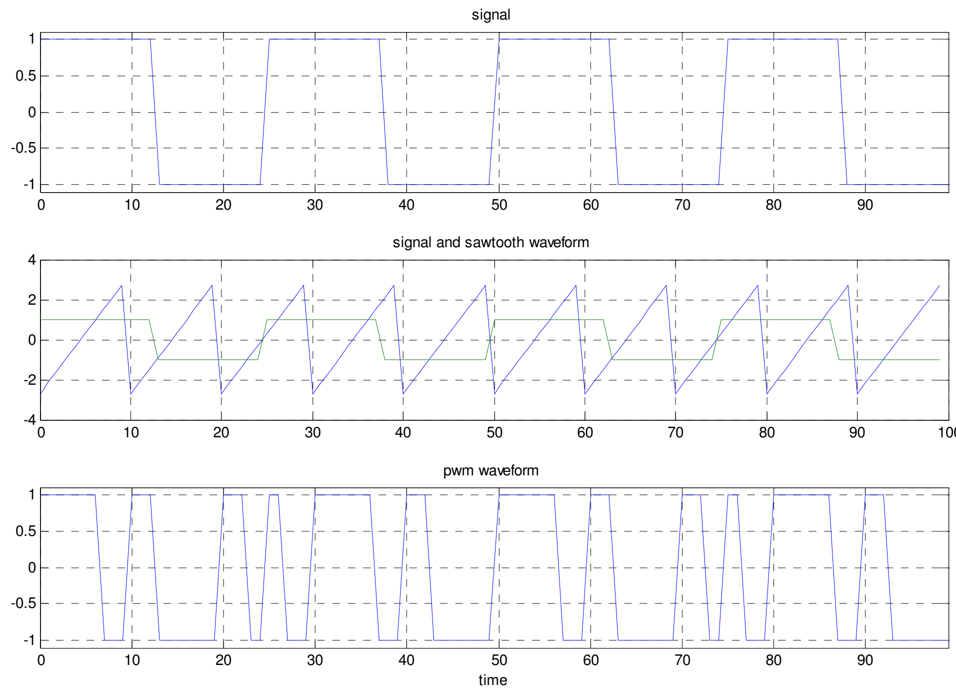

Figure 3.9 The error signal compared with sawtooth waveform to obtain PWM switching signal.

3.2.1.2 Transformer Design Consideration

The transformer is the most important component that determines the performance such as the efficiency, output regulation and EMI of the flyback converter (Hang-Seok, 2003). Ferrite core is the most widely used core material for commercial SMPS. The type of the core should be chosen with regard to system requirements including number of outputs, physical size, and cost. EER type core is used generally for the set top box applications.

Once the core type and size are determined, the following variables are obtained from the data sheet of the core.

- A_e: The cross-sectional area of the core (mm^2)
- A_w: Winding window area (mm^2)
- B_{sat}: Core saturation flux density (tesla)(Usually B_{sat} =0.3~0.35 T)

In order to determine the primary side inductance, the following variables should be determined first.

- P_{in}: Maximum input power
- f_s: Switching frequency of MOSFET
- $V_{DC,\,min}$: Minimum DC link voltage
- D_{max}: Maximum duty cycle
- K_{RF}: Ripple factor, which is defined at the minimum input voltage and full load condition

For discontinuous mode operation, $K_{RF} = 1$ and for continuous mode operation $K_{RF} < 1$. The ripple factor is closely related with the transformer size and the rms value of the MOSFET current (McLyman, 1988).

With the given variables, the primary side inductance, L_m, is obtained as (Hang-Seok, 2003)

$$L_m = \frac{(V_{DC,\min} D_{\max})^2}{2P_{in} f_s K_{RF}} \tag{3.24}$$

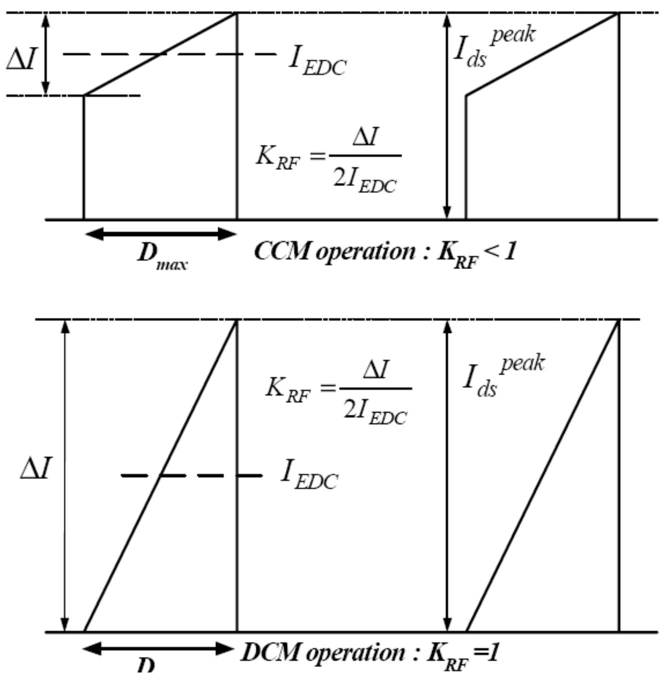

Figure 3.10 MOSFET drain current and ripple factor (K_{RF}).

Once L_m is determined, the maximum peak current $I_{ds,\ peak}$ and rms current $I_{ds,rms}$ of the MOSFET in normal operation are obtained as (Hang-Seok, 2003)

$$I_{ds,peak} = (I_{EDC}) + (\frac{\Delta I}{2}) \tag{3.25}$$

$$I_{ds}^{rms} = \sqrt{\left[3(I_{EDC})^2 + (\frac{\Delta I}{2})^2\right]\frac{D_{\max}}{3}} \tag{3.26}$$

where

$$I_{EDC} = \frac{P_{in}}{V_{DC,\min} D_{\max}} \tag{3.27}$$

and

$$\Delta I = \frac{V_{DC,\min} D_{\max}}{L_m f_s} \tag{3.28}$$

With the chosen core, the minimum number of turns of the primary side to avoid the core saturation is given by (Hang-Seok, 2003)

$$N_{P,\min} = \frac{L_m I_{over}}{B_{sat} A_e} \times 10^6 \tag{3.29}$$

where I_{over} is the pulse-by-pulse current limit level.

In order to determine the number of turns in the secondary sides for each output, firstly the turns ratio (n) of the transformer should be found out as a reference.

$$n = \frac{V_{RO}}{V_{o1} + V_{F1}} = \frac{N_P}{N_{s1}} \tag{3.30}$$

where V_{RO}= V_L used in the previous equations, N_p and N_{s1} are the number of turns for primary side and reference output, respectively, V_{o1} is the output voltage and V_{F1} is the diode forward voltage drop of the reference output that is regulated by the feedback control.

Then, the proper integer for N_{s1} is determined so that the resulting N_p is larger than $N_{p,min}$ obtained by Equation (3.29). The number of turns for the other output (n-th output) and the number of turns for V_{cc} winding are determined by (Hang-Seok, 2003)

$$N_{s(n)} = \frac{V_{o(n)} + V_{F(n)}}{V_{o1} + V_{F1}} . N_{s1} \tag{3.31}$$

$$N_a = \frac{V_{cc} + V_{Fa}}{V_{o1} + V_{F1}} . N_{s1} \tag{3.32}$$

where V_{cc} is the auxiliary voltage used to supply the control circuit shown in Figure 3.11 and V_{Fa} is the forward voltage drop that is placed on auxiliary output, N_a is the number of turns for the auxiliary side.

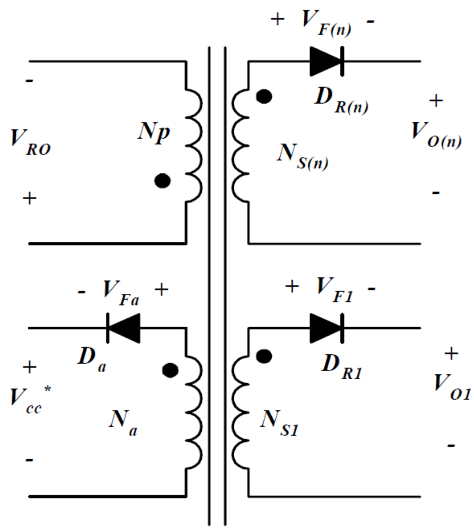

Figure 3.11 Simplified diagram of the transformer.

Once the number of turns on the primary side has been determined, the gap length of the core is obtained in mm through approximation as (Hang-Seok, 2003)

$$G = 40\pi A_e \left(\frac{N_P^2}{1000 L_m} - \frac{1}{A_L} \right) \tag{3.33}$$

where A_L is the AL-value with no gap in nH/turns^2 given in the datasheet of the core, A_e is the cross sectional area of the core in cm^2, L_m is in µH specified in Equation 3.28 and N_p is the number of turns for the primary side of the transformer.

3.2.2 EMI Sources in Flyback Converters

SMPS generates EMI due to the switching operation. The switching device is a MOSFET operating at high frequency. It leads to generate high *dv/dt* and *di/dt* that are the main causes of EMI. EMI may cause distortion of control circuitry within the converter itself and it may also interfere with other electronic equipments.

Rapid transient voltage and current changes during turn-on and turn-off operations are the main sources of conducted and radiated EMI. The RF energy that is radiated by the circuits of the control section is not enough to create a serious hazard for the correct operation of the converter section. However, knowledge of the converter section's radiated near field is extremely important for correcting EMC design of the device, because this electromagnetic radiation has enough energy to affect the operations of the control section or other circuit boards nearby, possibly causing malfunctions. Radiated EMI can be divided in to near field and far field in an SMPS. Feng, Xia & Dong (2006) has investigated and studied on radiated emissions in SMPS.

In an SMPS the conducted EMI is divided into DM and CM EMI. CM and DM currents are responsible to create conducted noise emission from power cord, so it is important to reduce this noise to meet EMC requirements (Wei, & Zhaoming, 2004). The leakage capacitance between the switching device and its heat-sink, parasitic capacitance between the heat-sink and the grounded chassis and parasitic capacitances between other devices or wires, which carry pulsating voltage waveform and the grounded chassis, are the CM noise source impedances of the converter. The major components of DM noise source impedance are the turned-on resistance of rectifying diodes, the equivalent series resistance and equivalent series inductance of the bulk capacitor (See, & Deng, 2003).

In the flyback power converter, the transformer primary current (IPRI), drain voltage (VDRAIN), diode voltage (VDIODE) and transformer secondary current (ISEC) waveforms may generate emissions current (Figure 3.12). The waveforms produced are nearly a square wave as shown in the second waveform of Figure 3.13.

However, in practice this wave can take many shapes, the most common one is unsymmetrical trapezoid wave. The waveform generated by the switching on and off consists of significant harmonics up to several megahertz as shown in Figure 3.13 that is obtained from Microcap simulations.

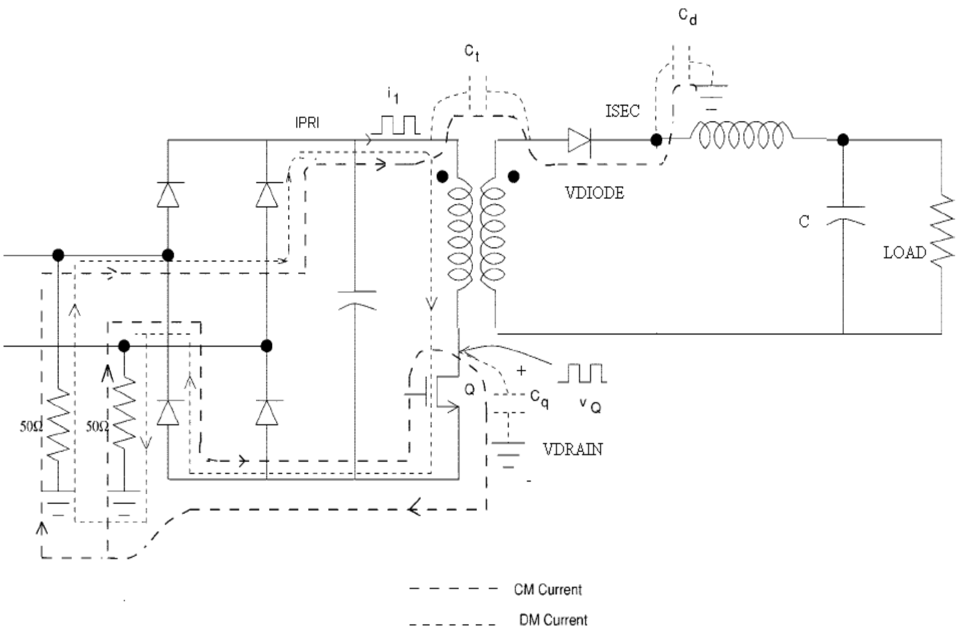

Figure 3.12 Sources and paths of conducted EMI. 50Ω resistors represent the spectrum analyzer.

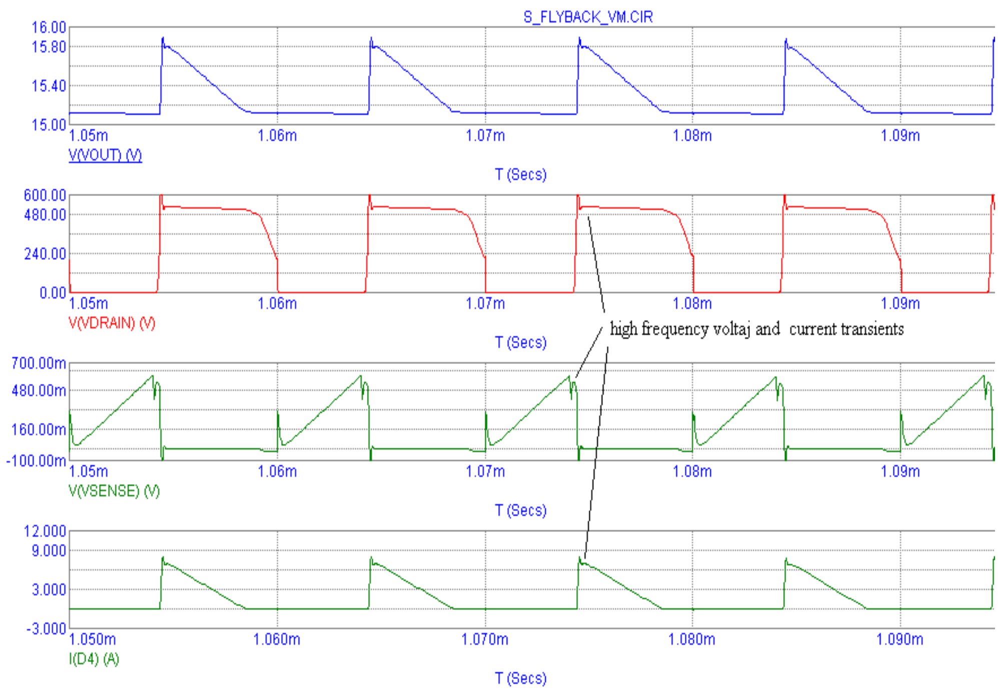

Figure 3.13 Voltage and current for a flyback SMPS.VOUT is the output voltage, I (D4) are the series diode located on the secondary side, VDRAIN is the drain voltage of the MOSFET.

The primary current waveform causes primarily DM emission currents to circulate between the AC mains and the power supply input. It can also create CM emissions due to radiated magnetic fields if the current path defined by the printed circuit board layout encircles a large physical area (Patel, 2008).

The drain-source voltage, VDRAIN, waveform is characterized by high dv/dt transitions. Parasitic circuit elements such as leakage inductance, MOSFET output capacitance and transformer capacitance cause additional voltage peaking and ringing in a certain frequency range. The MOSFET drain, transformer primary and drain clamping components connected to the drain terminal may drive displacement currents to earth ground through transformer capacitance or stray capacitance. This displacement current returns backward through the line and neutral conductors back to the MOSFET drain driving terminal as a CM emission current. The displacement currents generated by the drain voltage waveform cause spectral energy in the form of a CM conducted emission currents (Power Integrations AN-15, 2005).

Figures 3.14 and 3.15 show the CM noises in the charging and discharging paths in flyback converter.

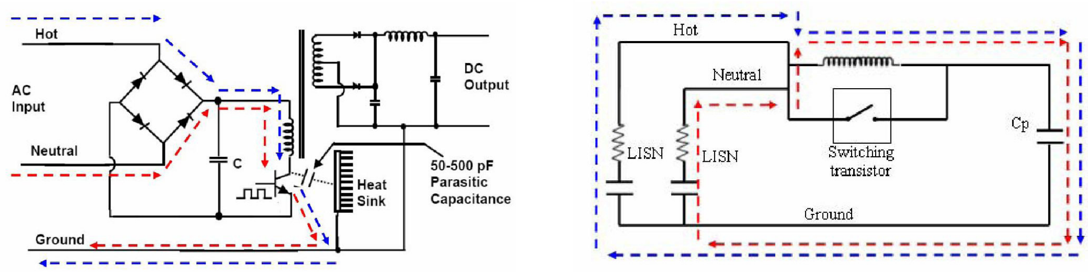

Figure 3.14 CM noise charging path in flyback converter (Katzir, & Singer, 2006).

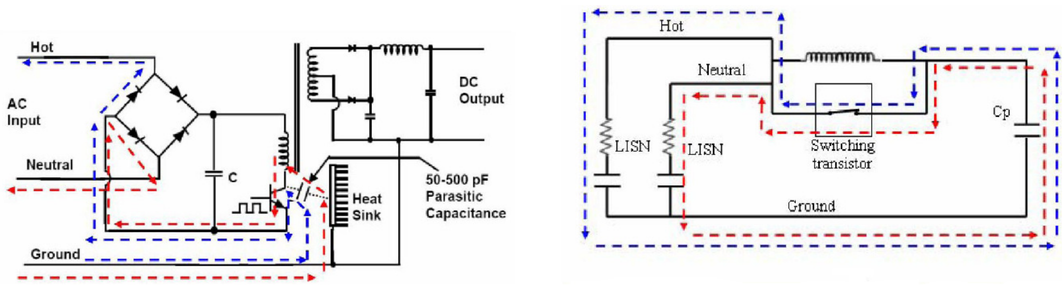

Figure 3.15 CM noise discharging path in flyback converter (Katzir, & Singer, 2006).

The diode voltage waveform VDIODE is also characterized by fast voltage changes and fast rise and fall times. Parasitic circuit elements such as transformer leakage inductance and diode capacitance cause additional voltage peaking and ringing at frequencies typically between 20 MHz and 30 MHz. The diode voltage waveform will drive displacement currents to earth ground through transformer capacitance or stray capacitance. The displacement currents generated by the diode voltage waveform cause spectral energy in the form of CM emission currents (Power Integrations AN-15, 2005).

Secondary current ISEC begins to flow as soon as MOSFET turns off. Current starts at a peak value and decreases linearly at a rate determined by secondary inductance and output voltage This trapezoidal (or triangular) current waveform is characterized in the frequency domain by a spectrum with a fundamental at the switching frequency and harmonics determined by the relative squareness of the waveform. Additional ringing superimposed on the waveform is related to the drain source voltage VDRAIN waveform previously discussed. This composite current waveform can cause significant magnetic fields to radiate if the current path defined by the printed circuit board layout encircles a large physical area (Power Integrations AN-15, 2005).

3.2.3 EMI Measurements in Flyback Converters

Radiated and conducted emissions are the two forms of the transmission of EMI in the circuit as mentioned in Chapter 2. Radiated emission is measured in the range of 30MHz -1GHz. Radiated emission requires the measurement of magnetic or electric fields in free space, which makes the test much more complex to do.

The conducted EMI is measured with line impedance stabilization network (LISN), in the frequency range of 150 kHz to 30 MHz. LISN is used to provide the 50Ω standard impedance in order to measure the EMI for different power supplies accurately and to make the repeated measurements reliable. LISN performs three functions. It suppresses all on the incoming noises from supply. Also it extracts the

RF noise from device under test (DUT) supply and stabilizes the impedance at 50Ω for measurement purposes.

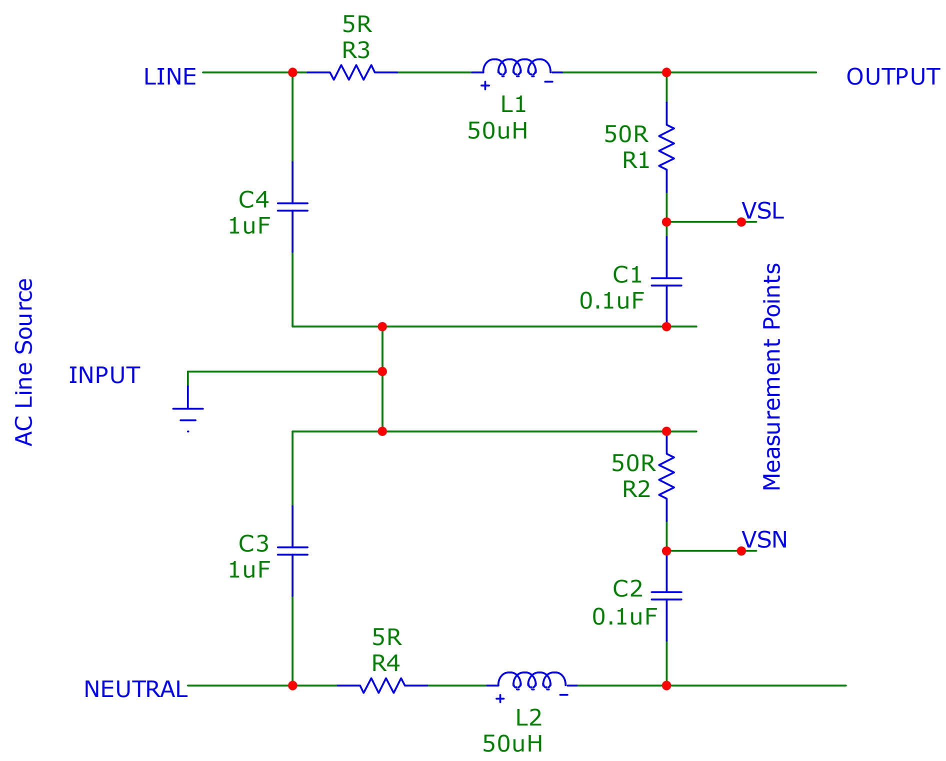

Figure 3.16 Line impedance stabilization network (LISN).

Figure 3.16 shows the effective filter, represented by L_1, L_2 and C_3, C_4 inside the LISN which passes line frequency currents but forces higher frequency power supply conducted emission currents to flow through coupling capacitors C_1, C_2 and sense resistors R_1, R_2. For 50Hz line frequency, the inductors are basically shorted; the capacitors are open and the power passes through the supply of the DUT. A spectrum analyzer or EMI receiver reads the magnitude of the current emission as sensed voltages V_{SL} and V_{SN} across R_1 and R_2 in dBµV (Power Integrations AN-15, 2005).

As mentioned above the conducted emission signal is applied to the spectrum analyzer or EMI receiver detector input. Standards specify three principal detectors type; peak, quasi peak (QP), and average (AV). The majority of signals that are measured use the peak detector. The peak detector responds almost instantly to the peak value of the interference signal. Regulatory standards define emission compliance levels using the QP detector, although some standards still require use of the peak detector. The emissions limits for AC mains interference voltage (line conducted interference) is specified for both QP and AV detectors. The difference between detectors is how they respond to pulsed or modulated signals. An illustration of these detector features is provided in Figure 3.17 (Montrose, & Nakauchi, 2004). All three types of detectors provide the same response to unmodulated continuous signals, such as clock.

The QP detector weights the measured value in terms of its perceived annoyance factor. This annoyance factor is defined for low-pulse-repetition frequencies. These low-pulse-repetition frequencies are less annoying when experienced on broadcast radio and television than higher pulse repetition frequencies. The QP detector is specified in terms of its attack and decay time constants. The average detector simply returns the average value rather than the peak of the interference signal as measured. The average filter is simply a low-pass filter whose time constant is slower than the slowest pulse repetition frequency of the input (Montrose, & Nakauchi, 2004).

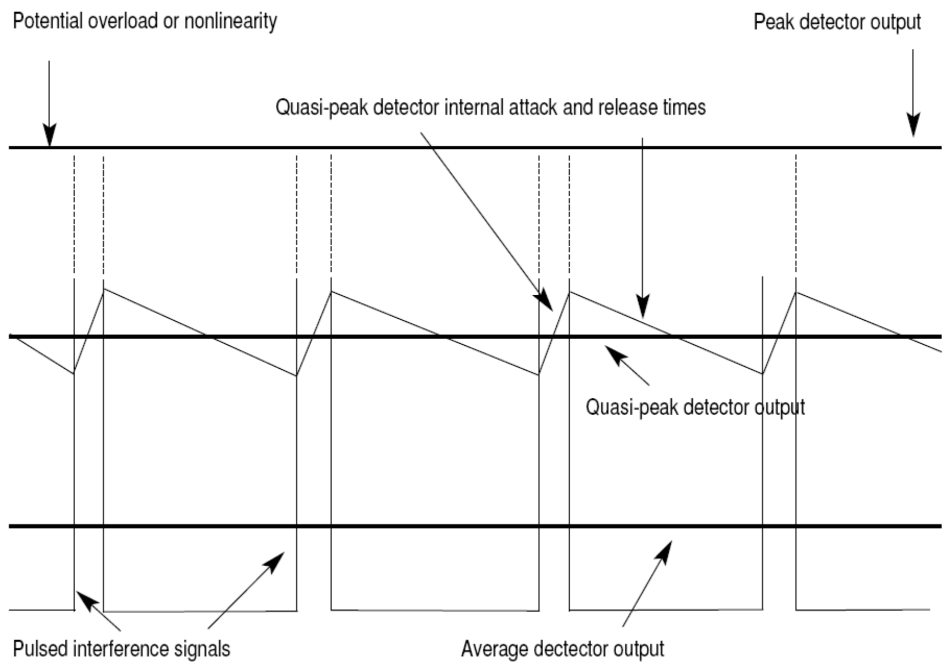

Figure 3.17 CISPR 16-1 detector responses to pulsed interference.

Typically, a large size of EMI suppression filter is needed if we want to suppress the EMI noise in the input line. This filter is typically made of an inductor (choke coil) and capacitance to ground. However, there is a need to keep leakage current from the line and into the ground plane for safety reasons, so the filter capacitance is normally limited to small values at the order of a few thousand picofarads. This means a large choke inductance is needed to meet the requirement. Furthermore, all the power has to pass through the choke meaning that the copper wire of the choke has to handle the power current (Katzir, & Singer, 2006). In order to reduce the size and cost of the EMI suppression filter, noise cancellation techniques have been introduced to the area of EMI.

CHAPTER FOUR
FM TECHNIQUE TO REDUCE EMI IN SMPS

There are many methods to reduce the EMI in SMPS as mentioned in Chapter 1. In this thesis, we use the FM technique for mitigating the EMI. This Chapter gives the FM theory and the spectrum of an FM modulated PWM signal.

4.1 Frequency Modulation

A modulator systematically alters the carrier wave in correspondence with the variation of the modulation signal. The signals in a modulation process are:

- Carrier signal: Periodic waveform of constant frequency (f_c) and constant amplitude.
- Modulating signal: Waveform, $s_m(t)$, represent the message and responsible for changing the initially constant characteristics of the carrier signal.
- Modulated signal: The resulted modulated wave carries the message information.

Modulation profile is the shape of the waveform used to modulate carrier signal and define the shape of the resulting modulated wave spectrum. In this thesis two modulation profiles (sinusoidal and triangular) are analyzed. The modulation profile determines the power spectrum of the FM modulated signal.

The effect of FM can be derived from the study of a sinusoidal wave that is modulated with the desired modulation profile (Balcells, & etc, 2005). The general expression, in time domain, of a frequency or phase modulated sinusoidal signal following a certain modulation profile is given by (Carlson, Crilly, & Rutledge, 2002)

$$X(t) = A_c.\cos[\theta_c(t)] \tag{4.1}$$

where A_c is the carrier amplitude and $\theta_c(t)$ is the total instantaneous angle of the modulated signal, given by

$$\theta_c(t) = \omega_c t + \phi(t) \tag{4.2}$$

where ω_c is the carrier frequency and $\phi(t)$ is the time dependent phase angle. If we take the derivatives of both sides of Equation (4.2), the instantaneous frequency of the modulated signal is obtained as

$$\frac{1}{2\pi}\frac{d}{dt}\theta_c(t) = f(t) = f_c + \frac{1}{2\pi}\frac{d}{dt}\phi(t) \tag{4.3}$$

The deviation of the instantaneous frequency directly depends on the amplitude of the modulating signal given by;

$$\frac{d}{dt}\phi(t) = 2\pi.k_w.s_m(t) \tag{4.4}$$

where $s_m(t)$ is modulating signal and k_w is the modulation sensitivity factor expressed in Hz/V. From this equation, $\phi(t)$ can be expressed as

$$\phi(t) = 2\pi\int_0^t k_w.s_m(\lambda).d\lambda \tag{4.5}$$

Therefore, the general expression of a frequency modulated sinusoidal waveform $X(t)$ takes the below form

$$X(t) = A_c.\cos[\omega_c.t + 2\pi.k_w\int_0^t s_m(\lambda).d\lambda] \tag{4.6}$$

By considering a sinusoidal modulating signal at the frequency of f_m defined by

$$s_m(t) = A_m \cos(2\pi f_m t) \tag{4.7}$$

The instantaneous frequency of the resulting FM signal equals

$$f(t) = f_c + k_w A_m \cos(2\pi f_m t) \tag{4.8}$$

where

$$\Delta f_c = k_w A_m \tag{4.9}$$

The quantity Δf_c is called the frequency deviation, representing the maximum departure of instantaneous frequency of the FM signal from the f_c. So by taking reference to the above equations it can be said that the Δf_c is proportional to the amplitude of the modulating signal and is independent of the f_m (Haykin, 2000).

Important parameters to describe the characteristics of the modulated signal are the modulation index (β) and the rate of modulation (δ) given by (Haykin, 2002);

$$\beta = \frac{\Delta f_c}{f_m} \tag{4.10}$$

$$\delta = \frac{\Delta f_c}{f_c} \tag{4.11}$$

The rate of modulation gives an idea on how wide the energy of a single harmonic will be spread relative to f_c (Figure 4.1). According to Carson's rule (Carson, 1922), the bandwidth of the FM signal can be calculated by

$$B = 2f_m(1+\beta) = 2(\Delta f_c + f_m) \tag{4.12}$$

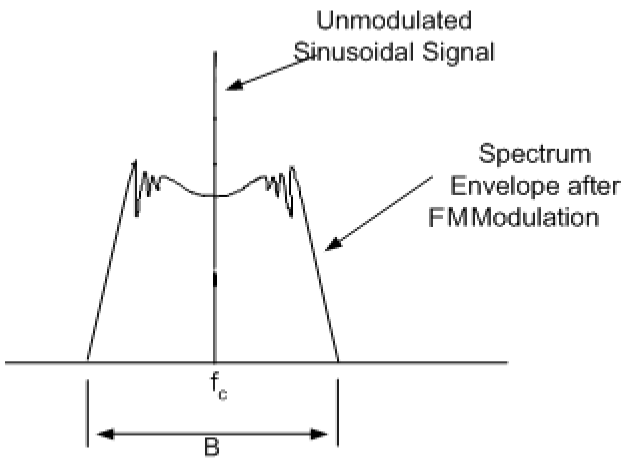

Figure 4.1 The effect of the FM on sinusoidal waveform.

4.2 Analysis for the Spectrum of the FM Modulated PWM Signal

In switching power converters the carrier (switching frequency, f_s) is not a sinusoidal waveform but it is a PWM signal. So it contains infinite number of harmonics. In order to analyze the effect of modulation, firstly the Fourier analysis of a periodic square waveform can be considered. One of the ways to obtain the PWM signal in the switching power converters is to compare the error signal (feedback signal obtained from secondary side of the converter) with a sawtooth waveform (Figure 4.2). The frequency of the sawtooth signal and the voltage level of the error signal in Figure 4.2 are constant.

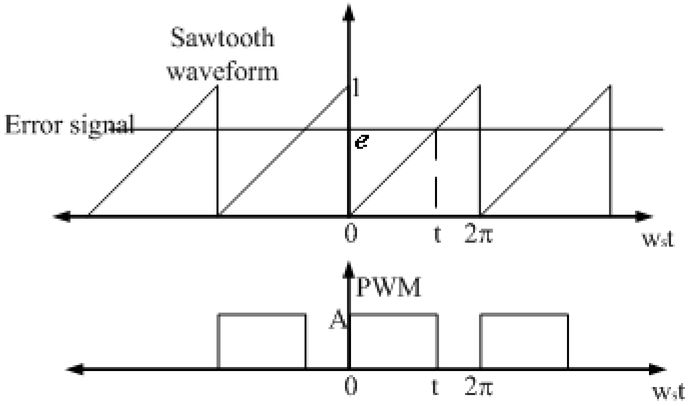

Figure 4.2 Generation of PWM signal by comparison of sawtooth carrier and constant error signal.

Any periodic function can be represented as an infinite sum of harmonic sinusoids multiplied by appropriate coefficients. Using the Fourier series representation, PWM signal *g(t)* in Figure 4.2 can be expressed as

$$g(t) = a_0 + \sum_{n=1}^{\infty} a_n \cos n\omega_s t + b_n \sin n\omega_s t \tag{4.13}$$

where ω_s is the switching frequency. The Fourier coefficients are given by

$$a_0 = \frac{1}{2\pi}\int_0^{t_0} g(t)dx = Ae \tag{4.14}$$

$$a_n = \frac{1}{\pi}\int_0^{t_0} g(t)\cos nxdx = \frac{A}{\pi n}(\sin n2\pi e) \tag{4.15}$$

$$b_n = \frac{1}{\pi}\int_0^{t_0} g(t)\sin nxdx = \frac{A}{\pi n}(1-\cos n2\pi e) \tag{4.16}$$

$$g(t) = Ae + \frac{A}{\pi}\sum_{n=1}^{\infty}\left[\frac{1}{n}(\sin n2\pi e)\cos n\omega_s t + \frac{1}{n}(1-\cos n2\pi e)\sin n\omega_s t\right] \tag{4.17}$$

For *e*=0.5 the frequency components of the square wave can be written as;

$$g(t) = \frac{A}{2} + \frac{A}{\pi}\sum_{n=odd}^{\infty}\frac{2}{n}\sin n\omega_s t \tag{4.18}$$

Taking the Fourier transform of this signal yields

$$G(f) = \frac{A}{2}\delta(f) + \sum_{n=odd}^{\infty}\frac{A}{j\pi n}\left[\delta(f-nf_s)-\delta(f+nf_s)\right] \tag{4.19}$$

For a square-wave signal, there are components at the switching frequency and its odd harmonics as it is evident from the above equation. Figure 4.3 is obtained by adding many sinusoids at different frequencies using MATLAB program. The spectrum of the resultant square wave signal is plotted in Figure 4.4.

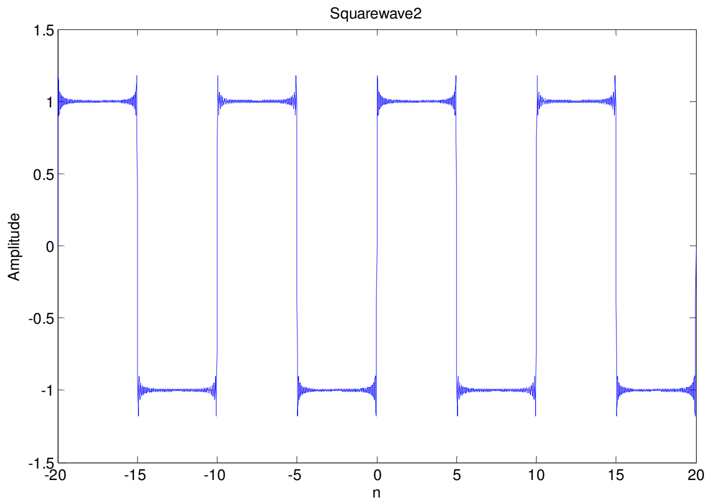

Figure 4.3 An infinite sum of sinusoids.

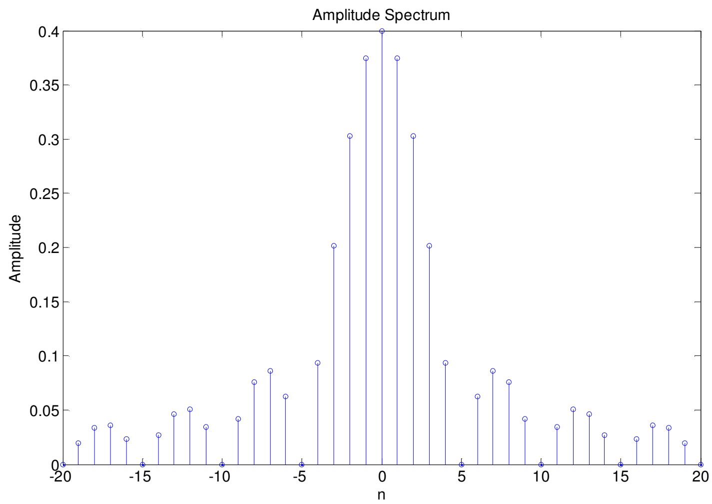

Figure 4.4 Two-sided magnitude spectrum and frequency domain representation of a square wave.

It is seen from the spectrum, the distance between two consecutive harmonics is given as the frequency of the carrier signal, f_c. The frequency of the nth harmonic, f_n, is expressed as (Balcells, & etc, 2005);

$$f_n = nf_c \tag{4.20}$$

The coefficients of Fourier series can change according to the on-off time or period of the PWM (Figure 4.5).

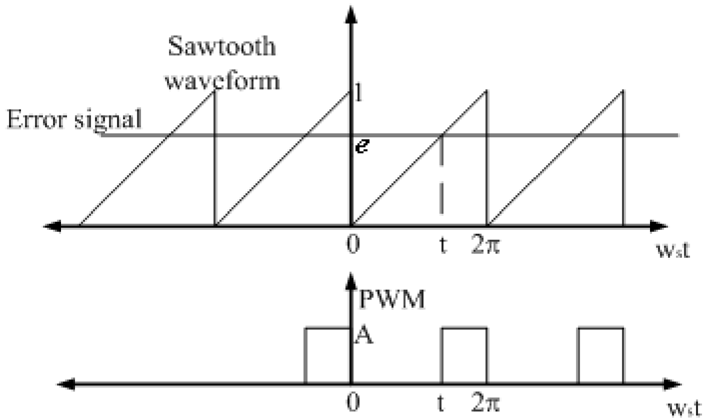

Figure 4.5 Production of PWM signals with a different on and off time.

$$a_0 = \frac{1}{2\pi}\int_t^{2\pi} g(t)dx == A(1-e) \tag{4.21}$$

$$a_n = \frac{1}{\pi}\int_t^{2\pi} g(t)\cos nxdx = \frac{A}{\pi n}(\sin n2\pi - \sin n2\pi e) \tag{4.22}$$

$$b_n = \frac{1}{\pi}\int_t^{2\pi} g(t)\sin nxdx = \frac{A}{\pi n}(-\cos n2\pi + \cos n2\pi e) \tag{4.23}$$

$$\begin{aligned} g(t) &= A(1-e) + \sum_{n=1}^{\infty}\left[\begin{array}{l} (\frac{A}{\pi n}(\sin n2\pi - \sin n2\pi e)\cos n\omega_s t \\ +\frac{A}{\pi n}(-\cos n2\pi + \cos n2\pi e)\sin n\omega_s t) \end{array}\right] \\ &= A(1-e) - \frac{A}{\pi}\sum_{n=1}^{\infty}\frac{1}{n}(\sin n2\pi e)\cos n\omega_s t - \frac{A}{\pi}\sum_{n=1}^{\infty}\frac{1}{n}(1-\cos n2\pi e)\sin n\omega_s t \end{aligned} \tag{4.24}$$

The result is the same with the Equation (1) given by Kaboli & Mahdavi (2007). It is seen from Equation (4.24), the frequency spectrum again contains the switching frequency and also its harmonic components.

In reality, the error signal e, which is applied to one of the inputs of the comparator, is not constant during the operation of the converter. Its value depends on the changes in the load and modulates the duty cycle of the PWM. In order to make the mathematical calculations, it is assumed that the error signal is a low frequency sinusoidal signal, that is $e(t)=E\sin\omega_{er}t$, where ω_{er} is the frequency of the error signal. In practice ω_{er} is much smaller than ω_s, i.e, $\omega_{er} << \omega_s$ (Figure 4.6).

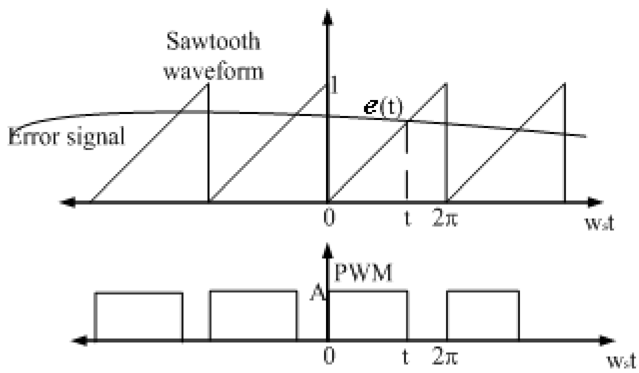

Figure 4.6 Production of PWM signal by comparing the sawtooth carrier and low frequency sinusoidal error signal.

The Fourier series coefficient of this signal can be written as

$$a_0 = \frac{1}{2\pi}\int_0^t g(t)dx = AE\sin\omega_{er}t \tag{4.25}$$

$$a_n = \frac{1}{\pi}\int_0^{2\pi e(t)} g(t)\cos nx dx = \frac{A}{n\pi}\sin(n2\pi E\sin\omega_{er}t) \tag{4.26}$$

$$b_n = \frac{1}{\pi}\int_0^{2\pi e(t)} g(t)\sin nx dx = \frac{A}{n\pi}(1-\cos(n2\pi E\sin\omega_{er}t)) \tag{4.27}$$

$$g(t) = AE\sin\omega_{er}t + \frac{A}{\pi}\sum_{n=1}^{\infty}\begin{bmatrix}\frac{1}{n}\sin(n2\pi E\sin\omega_{er}t)\cos(n\omega_s t) \\ +\frac{1}{n}(1-\cos(n2\pi E\sin\omega_{er}t)\sin n\omega_s t\end{bmatrix} \tag{4.28}$$

$$g(t) = AE\sin\omega_{er}t + \frac{A}{\pi}\sum_{n=1}^{\infty}\frac{1}{n}\sin(n2\pi E\sin\omega_{er}t)\cos(n\omega_s t) + \frac{1}{n}\sin n\omega_s t - \frac{1}{n}\cos(n2\pi E\sin\omega_{er}t)\sin n\omega_s t \tag{4.29}$$

$$g(t) = AE\sin\omega_{er}t + \frac{A}{\pi}\sum_{n=1}^{\infty}\frac{1}{n}\sin n\omega_s t + \frac{A}{\pi}\sum_{n=1}^{\infty}\frac{1}{n}\sin(n2\pi E\sin\omega_{er}t - n\omega_s t) \tag{4.30}$$

$$g(t) = AE\sin\omega_{er}t + \frac{A}{\pi}\sum_{n=1}^{\infty}\frac{1}{n}\sin n\omega_s t - \frac{A}{\pi}\sum_{n=1}^{\infty}\frac{1}{n}\sin(n\omega_s t - n2\pi E\sin\omega_{er}t) \tag{4.31}$$

We expand the terms by applying the Bessel identities,

$$\cos(z\sin\theta) = \sum_{n=-\infty}^{\infty} J_n(z)\cos(n\theta) \tag{4.32}$$

$$\sin(z\sin\theta) = \sum_{n=-\infty}^{\infty} J_n(z)\sin(n\theta) \tag{4.33}$$

where we have used the results $J_{-n}(z) = (-1)^n J_n(z)$ to simplify the summations. From these equations the term in Equation (4.31) expands as

$$\sin(n\omega_s t - n2\pi E\sin\omega_{er}t) = \sum_{h=-\infty}^{\infty} J_h(n2\pi E)\sin((n\omega_s - h\omega_{er})t) \tag{4.34}$$

$$g(t) = AE\sin\omega_{er}t + \frac{A}{\pi}\sum_{n=1}^{\infty}\frac{1}{n}\sin n\omega_s t - \frac{A}{\pi}\sum_{n=1}^{\infty}\frac{1}{n}\sum_{h=-\infty}^{\infty} J_h(n2\pi E)\sin((n\omega_s - h\omega_{er})t) \tag{4.35}$$

$$\begin{aligned} g(t) = {} & AE\sin\omega_{er}t + \frac{A}{\pi}\sum_{n=1}^{\infty}\frac{1}{n}\sin n\omega_s t - \frac{A}{\pi}\sum_{n=1}^{\infty}\frac{1}{n}J_0(n2\pi E)\sin(n\omega_s t) \\ & - \frac{A}{\pi}\sum_{n=1}^{\infty}\frac{1}{n}\sum_{h=1}^{\infty} J_h(n2\pi E)\left[\sin((n\omega_s - h\omega_{er})t) + (-1)^h\sin((n\omega_s + h\omega_{er})t)\right] \end{aligned} \tag{4.36}$$

$$\begin{aligned} g(t) = {} & AE\sin\omega_{er}t + \frac{A}{\pi}\sum_{n=1}^{\infty}\frac{1}{n}(1 - J_0(n2\pi E))\sin n\omega_s t \\ & - \frac{A}{\pi}\sum_{n=1}^{\infty}\frac{1}{n}\sum_{h=1}^{\infty} J_h(n2\pi E)\left[\sin((n\omega_s - h\omega_{er})t) + (-1)^h\sin((n\omega_s + h\omega_{er})t)\right] \end{aligned} \tag{4.37}$$

The spectrum of the PWM signal includes the frequency and magnitude of:

$$G(f)=\frac{AE}{2j}\left[\delta(f-f_{er})-\delta(f+f_{er})\right]+\frac{A}{2\pi j}\sum_{n=1}^{\infty}\frac{1}{n}(1-J_0(n2\pi E))\left[\delta(f-nf_s)-\delta(f+nf_s)\right]$$
$$-\frac{A}{2j\pi}\sum_{n=1}^{\infty}\frac{1}{n}\sum_{h=1}^{\infty}J_h(n2\pi E)\begin{bmatrix}\{\delta(f-(nf_s-hf_{er}))-\delta(f+(nf_s-hf_{er}))\} \\ +(-1)^h\{\delta(f-(nf_s+hf_{er}))-\delta(f+(nf_s+hf_{er}))\}\end{bmatrix} \tag{4.38}$$

It is seen from the Equation (4.38), the frequency spectrum contains the frequency of the error signal, switching frequency and its harmonics and also contains the error signal frequency at the upper and lower side of the switching frequency and its harmonics.

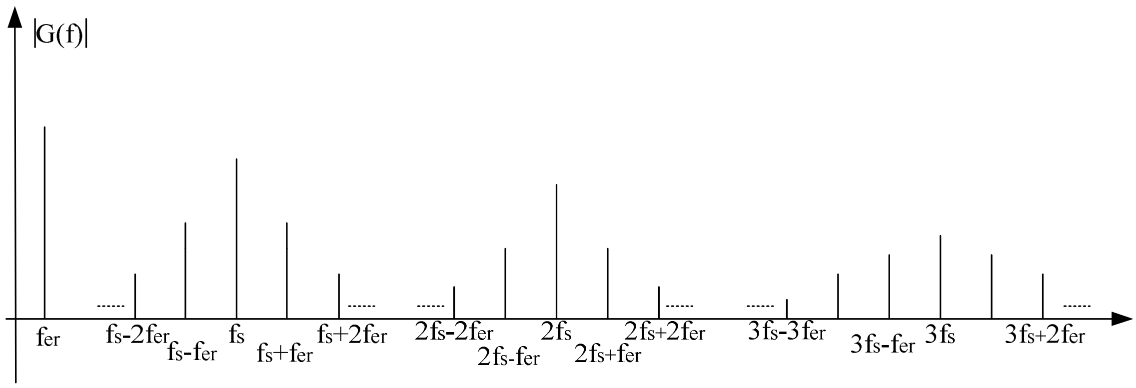

Figure 4.7 Spectrum of unmodulated PWM signal.

When $g(t)$ is modulated by a sinusoidal function with a frequency of f_m, the total instantaneous angle can be written as using Equation (4.6);

$$\theta(t)=\omega_s t+\beta\sin\omega_m t \tag{4.39}$$

After modulation, the ω_s is no longer constant, and the effect of ω_s can be mathematically replaced by phase angle modulation (Boys, 1993; Kaboli & Mahdavi, 2007)

$$g(t)=a_0+\sum_{n=1}^{\infty}a_n\cos n\left[\theta(t)\right]+b_n\sin n\left[\theta(t)\right] \tag{4.40}$$

In the following formulations the frequency of the PWM signal is not constant. It changes with the frequency and amplitude of the modulating signal of frequency f_m. The duty cycle of the PWM signal changes according to the voltage level of the error signal. Then for the FM modulated PWM signal Equation (4.30) can be rewritten as;

$$g(t) = AE\sin\omega_{er}t + \frac{A}{\pi}\sum_{n=1}^{\infty}\frac{1}{n}\sin n(\omega_s t + \beta\sin\omega_m t) + \frac{A}{\pi}\sum_{n=1}^{\infty}\frac{1}{n}\sin(n2\pi E\sin\omega_{er}t - n\omega_s t - n\beta\sin\omega_m t) \tag{4.41}$$

$$\begin{aligned} g(t) &= AE\sin\omega_{er}t + \frac{A}{\pi}\sum_{n=1}^{\infty}\frac{1}{n}\sin n(\omega_s t + \beta\sin\omega_m t) \\ &+ \frac{A}{\pi}\sum_{n=1}^{\infty}\frac{1}{n}\begin{bmatrix} \sin(n2\pi E\sin\omega_{er}t)\cos(n\omega_s t + n\beta\sin\omega_m t) \\ -\cos(n2\pi E\sin\omega_{er}t)\sin(n\omega_s t + n\beta\sin\omega_m t) \end{bmatrix} \end{aligned} \tag{4.42}$$

$$\begin{aligned} g(t) &= AE\sin\omega_{er}t + \frac{A}{\pi}\sum_{n=1}^{\infty}\frac{1}{n}\sum_{m=-\infty}^{\infty}J_h(n\beta)\sin(n\omega_s t + h\omega_m t) \\ &+ \frac{A}{\pi}\sum_{n=1}^{\infty}\frac{1}{n}\begin{bmatrix} \sum_{k=-\infty}^{\infty}J_k(n2\pi E)\sin(k\omega_{er}t)\sum_{h=-\infty}^{\infty}J_h(n\beta)\cos(n\omega_s t + h\omega_m t) \\ -\sum_{k=-\infty}^{\infty}J_k(n2\pi E)\cos(k\omega_{er}t)\sum_{h=-\infty}^{\infty}J_h(n\beta)\sin(n\omega_s t + h\omega_m t) \end{bmatrix} \end{aligned} \tag{4.43}$$

$$\begin{aligned} g(t) &= AE\sin\omega_{er}t + \frac{A}{\pi}\sum_{n=1}^{\infty}\frac{1}{n}\sum_{h=-\infty}^{\infty}J_h(n\beta)\sin(n\omega_s t + h\omega_m t) \\ &+ \frac{A}{\pi}\sum_{n=1}^{\infty}\frac{1}{n}\begin{bmatrix} \sum_{k=-\infty}^{\infty}\sum_{h=-\infty}^{\infty}J_k(n2\pi E)\sin(k\omega_{er}t)J_h(n\beta)\cos(n\omega_s t + h\omega_m t) \\ -\sum_{k=-\infty}^{\infty}\sum_{h=-\infty}^{\infty}J_k(n2\pi E)\cos(k\omega_{er}t)J_h(n\beta)\sin(n\omega_s t + h\omega_m t) \end{bmatrix} \end{aligned} \tag{4.44}$$

$$\begin{aligned} g(t) &= AE\sin\omega_{er}t + \frac{A}{\pi}\sum_{n=1}^{\infty}\frac{1}{n}\sum_{h=-\infty}^{\infty}J_h(n\beta)\sin(n\omega_s t + h\omega_m t) \\ &- \frac{A}{\pi}\sum_{n=1}^{\infty}\frac{1}{n}\left[\sum_{k=-\infty}^{\infty}\sum_{h=-\infty}^{\infty}J_k(n2\pi E)J_h(n\beta)\sin(n\omega_s t + h\omega_m t - k\omega_{er}t)\right] \end{aligned} \tag{4.45}$$

$$\begin{aligned} g(t) &= AE\sin\omega_{er}t + \frac{A}{\pi}\sum_{n=1}^{\infty}\frac{1}{n}\left\{J_0(n\beta)\sin(n\omega_s t) + \sum_{h=1}^{\infty}J_h(n\beta)\begin{bmatrix} (\sin n\omega_s t + h\omega_m t) \\ +(-1)^h\sin(n\omega_s - h\omega_m t) \end{bmatrix}\right\} \\ &- \frac{A}{\pi}\sum_{n=1}^{\infty}\frac{1}{n}\left\{\sum_{k=-\infty}^{\infty}J_k(n2\pi E)\begin{bmatrix} J_0(n\beta)\sin(n\omega_s t - k\omega_{er}t) \\ +\sum_{h=1}^{\infty}J_h(n\beta)\begin{pmatrix} \sin(n\omega_s t + h\omega_m t - k\omega_{er}t) \\ +(-1)^h\sin(n\omega_s t - h\omega_m t - k\omega_{er}t) \end{pmatrix} \end{bmatrix}\right\} \end{aligned} \tag{4.46}$$

$$
\begin{aligned}
g(t) = {} & AE\sin\omega_{er}t + \frac{A}{\pi}\sum_{n=1}^{\infty}\frac{1}{n}\left\{J_0(n\beta)\sin(n\omega_s t) + \sum_{h=1}^{\infty}J_h(n\beta)\left[\sin(n\omega_s t + h\omega_m t) + (-1)^h\sin(n\omega_s - h\omega_m t)\right]\right\} \\
& - \frac{A}{\pi}\sum_{n=1}^{\infty}\frac{1}{n}\left\{J_0(n2\pi E)J_0(n\beta)\sin(n\omega_s t) + \sum_{k=1}^{\infty}J_k(n2\pi E)J_0(n\beta)\left[\sin(n\omega_s t - k\omega_{er}t) + (-1)^k\sin(n\omega_s t + k\omega_{er}t)\right]\right\} \\
& - \frac{A}{\pi}\sum_{n=1}^{\infty}\frac{1}{n}\sum_{h=1}^{\infty}J_0(n2\pi E)J_h(n\beta)\sin(n\omega_s t + h\omega_m t) - \frac{A}{\pi}\sum_{n=1}^{\infty}\frac{1}{n}\sum_{h=1}^{\infty}J_0(n2\pi E)J_h(n\beta)(-1)^h\sin(n\omega_s t - h\omega_m t) \\
& - \frac{A}{\pi}\sum_{n=1}^{\infty}\frac{1}{n}\sum_{h=1}^{\infty}J_h(n\beta)\sum_{k=1}^{\infty}J_k(n2\pi E)\left[\sin(n\omega_s t + h\omega_m t - k\omega_{er}t) + (-1)^k\sin(n\omega_s t + h\omega_m t + k\omega_{er}t)\right] \\
& - \frac{A}{\pi}\sum_{n=1}^{\infty}\frac{1}{n}\sum_{h=1}^{\infty}J_h(n\beta)(-1)^h\sum_{k=1}^{\infty}J_k(n2\pi E)\left[\sin(n\omega_s t - h\omega_m t - k\omega_{er}t) + (-1)^k\sin(n\omega_s t - h\omega_m t + k\omega_{er}t)\right]
\end{aligned}
\tag{4.47}
$$

$$
\begin{aligned}
g(t) = {} & AE\sin\omega_{er}t + \frac{A}{\pi}\sum_{n=1}^{\infty}\frac{1}{n}J_0(n\beta)\left[1 - J_0(n2\pi E)\right]\sin(n\omega_s t) \\
& + \frac{A}{\pi}\sum_{n=1}^{\infty}\frac{1}{n}\left[1 - J_0(n2\pi E)\right]\sum_{h=1}^{\infty}J_h(n\beta)\left[\sin(n\omega_s t + h\omega_m t) + (-1)^h\sin(n\omega_s - h\omega_m t)\right] \\
& - \frac{A}{\pi}\sum_{n=1}^{\infty}\frac{1}{n}J_0(n\beta)\sum_{k=1}^{\infty}J_k(n2\pi E)\left[\sin(n\omega_s t - k\omega_{er}t) + (-1)^k\sin(n\omega_s t + k\omega_{er}t)\right] \\
& - \frac{A}{\pi}\sum_{n=1}^{\infty}\frac{1}{n}\sum_{h=1}^{\infty}J_h(n\beta)\sum_{k=1}^{\infty}J_k(n2\pi E)\left[\begin{aligned}&\sin(n\omega_s t + h\omega_m t - k\omega_{er}t) + (-1)^k\sin(n\omega_s t + h\omega_m t + k\omega_{er}t) \\ &+ (-1)^h\sin(n\omega_s t - h\omega_m t - k\omega_{er}t) + (-1)^{h+k}\sin(n\omega_s t - h\omega_m t + k\omega_{er}t)\end{aligned}\right]
\end{aligned}
\tag{4.48}
$$

Taking the Fourier transform yields

$$
\begin{aligned}
G(f) = {} & \frac{AE}{2j}\left[\delta(f - f_{er}) - \delta(f + f_{er})\right] + \frac{A}{2\pi j}\sum_{n=1}^{\infty}\frac{1}{n}J_0(n\beta)\left[1 - J_0(n2\pi E)\right]\left[\delta(f - nf_s) - \delta(f + nf_s)\right] \\
& + \frac{A}{2\pi j}\sum_{n=1}^{\infty}\frac{1}{n}\left[1 - J_0(n2\pi E)\right]\sum_{h=1}^{\infty}J_h(n\beta)\left\{\begin{aligned}&\left[\delta(f - nf_s - hf_m) - \delta(f + nf_s + hf_m)\right] \\ &+ (-1)^h\left[\delta(f - nf_s + hf_m) - \delta(f + nf_s - hf_m)\right]\end{aligned}\right\} \\
& - \frac{A}{2\pi j}\sum_{n=1}^{\infty}\frac{1}{n}J_0(n\beta)\sum_{k=1}^{\infty}J_k(n2\pi E)\left\{\begin{aligned}&\left[\delta(f - nf_s + kf_{er}) - \delta(f + nf_s - kf_{er})\right] \\ &+ (-1)^k\left[\delta(f - nf_s - kf_{er}) - \delta(f + nf_s + kf_{er})\right]\end{aligned}\right\} \\
& - \frac{A}{2\pi j}\sum_{n=1}^{\infty}\frac{1}{n}\sum_{h=1}^{\infty}J_h(n\beta)\sum_{k=1}^{\infty}J_k(n2\pi E)\left\{\begin{aligned}&\left[\delta(f - nf_s - hf_m + kf_{er}) - \delta(f + nf_s + hf_m - kf_{er})\right] \\ &+ (-1)^k\left[\delta(f - nf_s - hf_m - kf_{er}) - \delta(f + nf_s + hf_m + kf_{er})\right] \\ &+ (-1)^h\left[\delta(f - nf_s + hf_m + kf_{er}) - \delta(f + nf_s - hf_m - kf_{er})\right] \\ &+ (-1)^{h+k}\left[\delta(f - nf_s + hf_m - kf_{er}) - \delta(f + nf_s - hf_m + kf_{er})\right]\end{aligned}\right\}
\end{aligned}
\tag{4.49}
$$

FM modulated PWM signal includes the harmonics of the switching frequency, upper and lower side band frequencies at the multiples of the switching frequency which are located apart from the frequency of modulating signal. The error signal also modulates the PWM signal hence spectrum includes both the frequencies of the error signal and its multiples which are located as side band harmonics of the modulated frequencies (Figure 4.8).

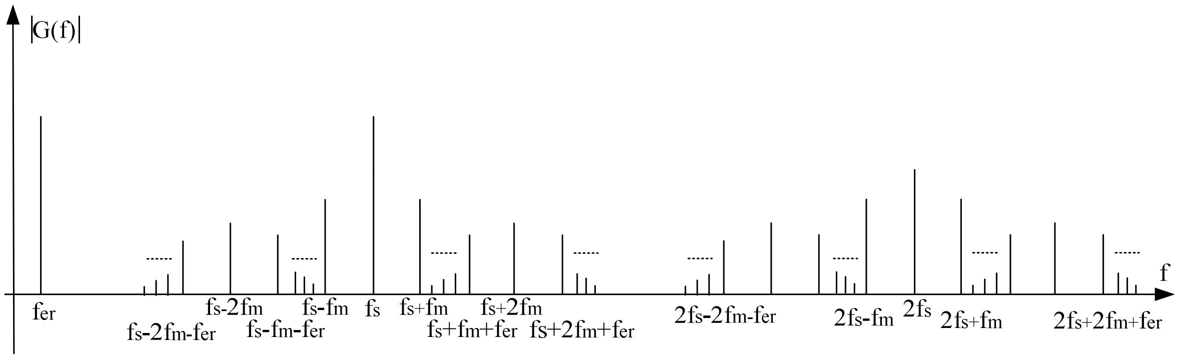

Figure 4.8 Spectrum of FM modulated PWM signal.

If it is assumed that the load of the converter is stable, then it can be said that the error signal is constant during whole operation. Therefore Equation (4.17) can be rewritten as;

$$g(t) = Ae + \frac{A}{\pi}\sum_{n=1}^{\infty}\left[\begin{array}{l}\frac{1}{n}(\sin n2\pi e)\cos n(\omega_s t + \beta \sin \omega_m t) + \frac{1}{n}\sin n(\omega_s t + \beta \sin \omega_m t) \\ -\frac{1}{n}\sin n(\omega_s t + \beta \sin \omega_m t)(\cos n2\pi e)\end{array}\right] \quad (4.50)$$

$$g(t) = Ae + \frac{A}{\pi}\sum_{n=1}^{\infty}\frac{1}{n}\sin n(\omega_s t + \beta \sin \omega_m t) + \frac{A}{\pi}\sum_{n=1}^{\infty}\frac{1}{n}\sin(n2\pi e - n(\omega_s t + \beta \sin \omega_m t)) \quad (4.51)$$

$$g(t) = Ae + \frac{A}{\pi}\sum_{n=1}^{\infty}\frac{1}{n}\sum_{h=-\infty}^{\infty}J_h(n\beta)\sin(n\omega_s t + h\omega_m t) + \frac{A}{\pi}\sum_{n=1}^{\infty}\frac{1}{n}\left[\sin(n2\pi e)\cos n(\omega_s t + \beta \sin \omega_m t)) - \cos(n2\pi e)\sin n(\omega_s t + \beta \sin \omega_m t)\right] \quad (4.52)$$

$$g(t) = Ae + \frac{A}{\pi}\sum_{n=1}^{\infty}\frac{1}{n}\left[J_0(n\beta)\sin n\omega_s t + \sum_{h=1}^{\infty}J_h(n\beta)\left(\sin(nw_s t + hw_m t) + (-1)^h \sin(n\omega_s t - h\omega_m t)\right)\right] + \frac{A}{\pi}\sum_{n=1}^{\infty}\frac{1}{n}\left[\sin(n2\pi e)\sum_{h=-\infty}^{\infty}J_h(n\beta)\cos(n\omega_s t + h\omega_m t) - \cos(n2\pi e)\sum_{h=-\infty}^{\infty}J_h(n\beta)\sin(n\omega_s t + h\omega_m t)\right] \quad (4.53)$$

$$g(t)=Ae+\frac{A}{\pi}\sum_{n=1}^{\infty}\frac{1}{n}J_0(n\beta)\sin n\omega_s t+\frac{A}{\pi}\sum_{n=1}^{\infty}\frac{1}{n}\sum_{h=1}^{\infty}J_h(n\beta)\left(\sin(n\omega_s t+h\omega_m t)+(-1)^h\sin(n\omega_s t-h\omega_m t)\right)$$
$$+\frac{A}{\pi}\sum_{n=1}^{\infty}\frac{1}{n}\left[\begin{array}{l}\sin(n2\pi e)J_0(n\beta)\cos n\omega_s t-\cos(n2\pi e)J_0(n\beta)\sin n\omega_s t\\+\sin(n2\pi e)\sum_{h=1}^{\infty}J_h(n\beta)(\cos(n\omega_s t+h\omega_m t)+(-1)^h\cos(n\omega_s t-h\omega_m t))\\-\cos(n2\pi e)\sum_{h=1}^{\infty}J_h(n\beta)(\sin(n\omega_s t+h\omega_m t)+(-1)^h\sin(n\omega_s t-h\omega_m t))\end{array}\right]$$
(4.54)

$$g(t)=Ae+\frac{A}{\pi}\sum_{n=1}^{\infty}\frac{1}{n}J_0(n\beta)\sin n\omega_s t+\frac{A}{\pi}\sum_{n=1}^{\infty}\frac{1}{n}\sum_{h=1}^{\infty}J_h(n\beta)\left(\sin(n\omega_s t+h\omega_m t)+(-1)^h\sin(n\omega_s t-h\omega_m t)\right)$$
$$+\frac{A}{\pi}\sum_{n=1}^{\infty}\frac{1}{n}\sin(n2\pi e)J_0(n\beta)\cos n\omega_s t-\frac{A}{\pi}\sum_{n=1}^{\infty}\frac{1}{n}\cos(n2\pi e)J_0(n\beta)\sin n\omega_s t$$
$$+\frac{A}{\pi}\sum_{n=1}^{\infty}\frac{1}{n}\sin(n2\pi e)\sum_{h=1}^{\infty}J_h(n\beta)(\cos(n\omega_s t+h\omega_m t)+(-1)^h\cos(n\omega_s t-h\omega_m t))$$
$$-\frac{A}{\pi}\sum_{n=1}^{\infty}\frac{1}{n}\cos(n2\pi e)\sum_{h=1}^{\infty}J_h(n\beta)(\sin(n\omega_s t+h\omega_m t)+(-1)^h\sin(n\omega_s t-h\omega_m t))$$
(4.55)

$$g(t)=Ae+\frac{A}{\pi}\sum_{n=1}^{\infty}\frac{1}{n}J_0(n\beta)\left[1-\cos(n2\pi e)\right]\sin n\omega_s t+\frac{A}{\pi}\sum_{n=1}^{\infty}\frac{1}{n}\sin(n2\pi e)J_0(n\beta)\cos n\omega_s t$$
$$+\frac{A}{\pi}\sum_{n=1}^{\infty}\frac{1}{n}\left[1-\cos(n2\pi e)\right]\sum_{h=1}^{\infty}J_h(n\beta)\left[\sin(n\omega_s t+h\omega_m t)+(-1)^h\sin(n\omega_s t-h\omega_m t)\right]$$
$$+\frac{A}{\pi}\sum_{n=1}^{\infty}\frac{1}{n}\sin(n2\pi e)\sum_{h=1}^{\infty}J_h(n\beta)\left[\cos(n\omega_s t+h\omega_m t)+(-1)^h\cos(n\omega_s t-h\omega_m t)\right]$$
(4.56)

The Fourier transform of this signal is found as

$$G(f)=Ae\delta(f)+\frac{A}{2\pi}\sum_{n=1}^{\infty}\frac{1}{n}J_0(n\beta)\left\{\begin{array}{l}\left[\sin(n2\pi e)+j\left(\cos(n2\pi e)-1\right)\right]\delta(f-nf_s)\\+\left[\sin(n2\pi e)-j\left(\cos(n2\pi e)-1\right)\right]\delta(f+nf_s)\end{array}\right\}$$
$$+\frac{A}{2\pi}\sum_{n=1}^{\infty}\frac{1}{n}\sum_{h=1}^{\infty}J_h(n\beta)\left\{\begin{array}{l}\left[\sin(n2\pi e)+j\left(\cos(n2\pi e)-1\right)\right]\left[\begin{array}{l}\delta(f-nf_s-hf_m)\\+(-1)^h\delta(f-nf_s+hf_m)\end{array}\right]\\+\left[\sin(n2\pi e)-j\left(\cos(n2\pi e)-1\right)\right]\left[\begin{array}{l}\delta(f+nf_s+hf_m)\\+(-1)^h\delta(f+nf_s-hf_m)\end{array}\right]\end{array}\right\}$$
(4.57)

For the duty cycle of d=0.5, the equation is rewritten as;

$$g(t)=\frac{A}{2}+\frac{A}{\pi}\sum_{n=odd}^{\infty}\frac{2}{n}J_0(n\beta)\sin n\omega_s t+\frac{A}{\pi}\sum_{n=odd}^{\infty}\frac{2}{n}\sum_{h=1}^{\infty}J_h(n\beta)\left(\sin(n\omega_s t+h\omega_m t)+(-1)^h\sin(n\omega_s t-h\omega_m t)\right)$$
(4.58)

The magnitude and frequency component of the *g(t)* can be shown as;

$$G(f,\beta)=\frac{A}{2}\delta(f)+\sum_{n=odd}^{\infty}\frac{A}{j\pi n}J_0(n\beta)(\delta(f-nf_s)-\delta(f+nf_s))$$
$$+\sum_{n=odd}^{\infty}\frac{A}{j\pi n}\sum_{h=1}^{\infty}J_h(n\beta)\left[\begin{array}{l}\delta(f-(nf_s+hf_m))-\delta(f+(nf_s+hf_m))\\+(-1)^h(\delta(f-(nf_s-hf_m))-\delta(f+(nf_s-hf_m)))\end{array}\right] \tag{4.59}$$

For a square-wave signal, $\beta=0$ and $J_0(0)$ exist only; then it reduces to Equation (4.19).

The power spectrum consist of discrete harmonics of the switching frequency and it also contains the upper and lower sidebands harmonics at the multiples of switching frequency that is located apart from the frequency of modulating signal. When the fundamental frequency of a square wave is modulated, each individual harmonic is spread into a certain frequency band (Figure 4.9).

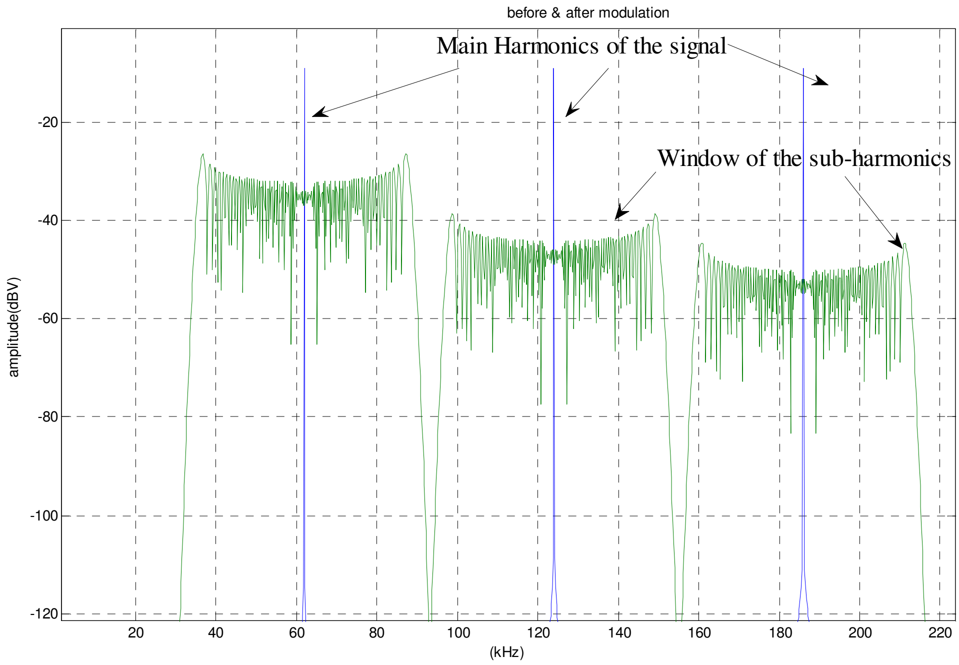

Figure 4.9 Spectrum of an FM modulated square-wave. (Modulating signal modulates the every harmonics of the carrier signal).

The bandwidth of the frequency modulated harmonic component n is written as;

$$B_n=2f_m(1+n\beta) \tag{4.60}$$

Equation (4.60) shows how the bandwidth of the harmonics increases as the number of harmonic getting higher. This may cause the spectrum to overlap at high frequencies, and hence reducing the efficiency of FM.

As β increases, the amplitude of the side band harmonics at the spectrum decreases. However, the degree of the increment in β is limited with the variation of the switching frequency where the converter operates. Considering two successive spectrums at the nth and (n+1)th harmonics one can determine the order of harmonic at which overlap begins.(see Figure 4.10).

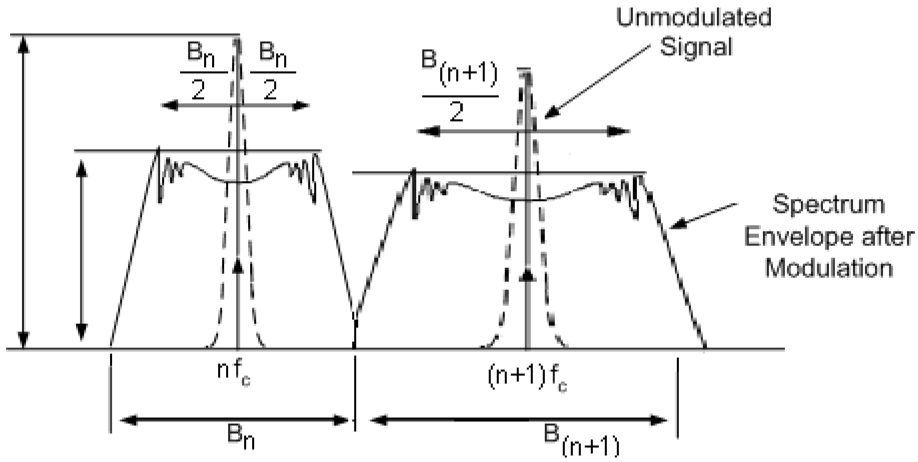

Figure 4.10 Spectrum for the harmonics at which overlap begins.

For overlap,

$$nf_c + \frac{B_n}{2} = (n+1)f_c - \frac{B_{n+1}}{2} \tag{4.61}$$

From this equation,

$$n_{overlap} = \frac{1}{2\delta} - \frac{1}{\beta} - \frac{1}{2} \tag{4.62}$$

Figure 4.11 shows the spectrum obtained from MATLAB for the case of overlapping which occurs at high frequencies.

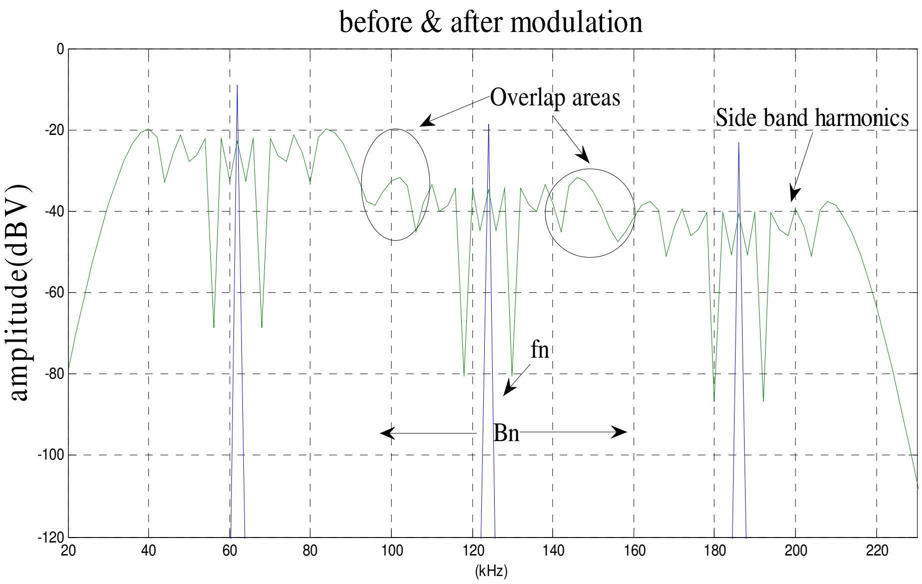

Figure 4.11 Side bands harmonics overlap.

4.3 Effects of the Modulation Parameters on the Spectrum

For the efficient EMI noise reduction in FM technique the parameters of the modulation are important. Each parameter and their values should be selected and determined carefully for the designed system. One of the most important parameter for FM is modulating signal. In order to investigate the effect of the modulating signal, two basic modulating signals, triangular and sinusoidal, have been studied. The typical frequency spectrums of signals modulated by these two signals are shown in Figures 4.12 - 4.14 which are obtained by using MATLAB program.

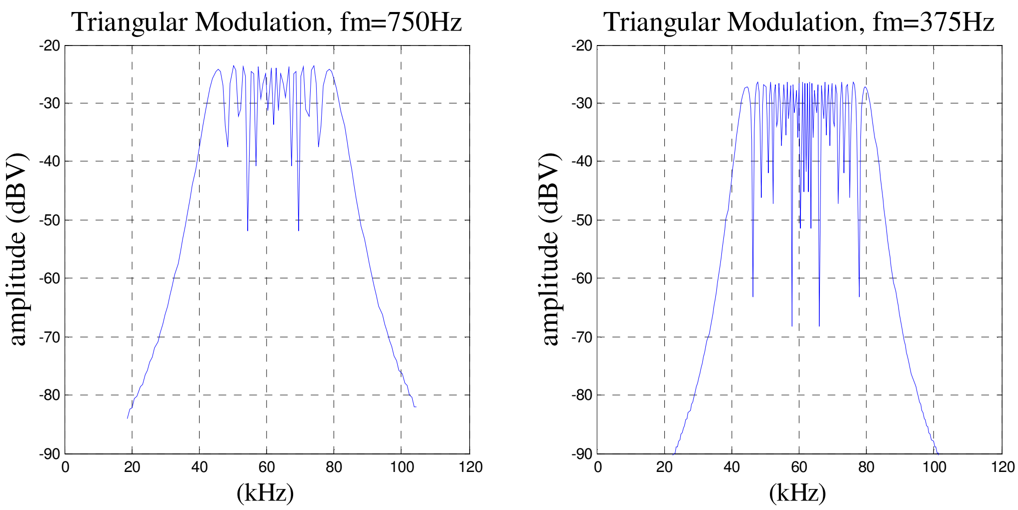

Figure 4.12 Evolution of side band harmonic with triangular modulating signal, f_c=62 kHz Δf_c=20kHz.

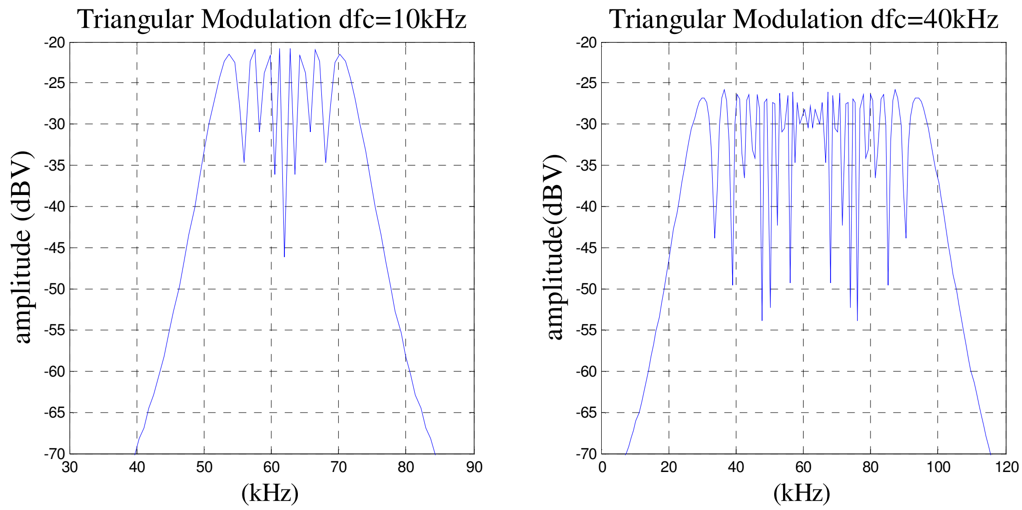

Figure 4.13 Evolution of side band harmonic with triangular modulating signal, fc=62 kHz fm=750Hz.

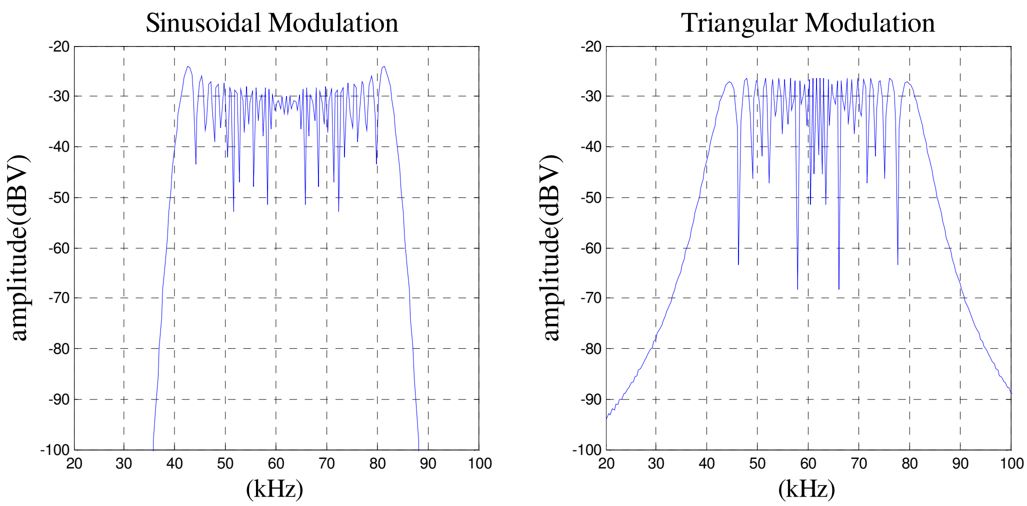

Figure 4.14 Frequency spectrum of a sinus signal modulated by sinusoidal and triangular modulating signals, f_c=62 kHz Δf_c=20kHz f_m=375Hz.

As shown in Figure 4.14 triangular modulating profile produce a complete flat spectrum shape. If the modulation profile has a constant slope during the modulation process, the resulting spectrum will have a flat distribution of side band harmonics. If the slopes are outside the area of the triangular waveform, i.e. sinusoidal signal, the side bands locate around the bandwidth limits of the spectrum (Figure 4.14). Higher modulation index produce larger attenuations regardless from the type of the modulation. This can be done by increasing the modulation ratio or the carrier frequency or decreasing the modulating frequency. For every modulation profile, amplitude reduction of the side band harmonics only depends on the modulation index (Figures 4.12 and 4.13).

By comparing the spectrums shown Figure 4.14 it is noticed that the triangular modulating signal gives the maximum amplitude reduction in the spectrum. Also it provides flat distribution which is preferable. Therefore, for the flyback power converter, the triangular profile is selected. The triangular modulating frequency is used in order to modulate the sawtooth waveform that is used in control mechanism of the controller explained in Section 3.2.1.1. So a variable frequency sawtooth waveform is obtained in order to produce a FM system.

CHAPTER FIVE
APPLICATION OF FREQUENCY MODULATION TECHNIQUE TO AC-DC FLYBACK CONVERTER

Most SMPS operate with constant switching frequency and variable duty cycle PWM signal. The spectrum of the sinusoidal waveform that is modulated by different modulating signals and the spectrum of a modulated PWM signal were discussed in Chapter 4. In this chapter, the PWM switching signal is modulated by using the triangular modulation profile in order to spread the each harmonic energy into an amount of side band harmonics that the advantages of it were explained in Chapter 4. A 24W flyback converter with the L6566B is built as a prototype which has a dedicated FM pin allowing the designer to modulate the switching frequency and so reduces the peak value of EMI. The conducted noise that is produced by the power converter is measured by using LISN and reported by the EMI receiver. Tests are repeated with different modulation parameters in order to see the effect of them.

5.1 Circuit Description Built with L6566B

In order to investigate the FM technique, a flyback converter board has been developed by using L6566B PWM controller IC (ST, 2008). The board accepts a wide range of input supply voltages (88V to 264V AC) and delivers 12V DC output voltage. Block diagram of the circuit is given in Figure 5.1.

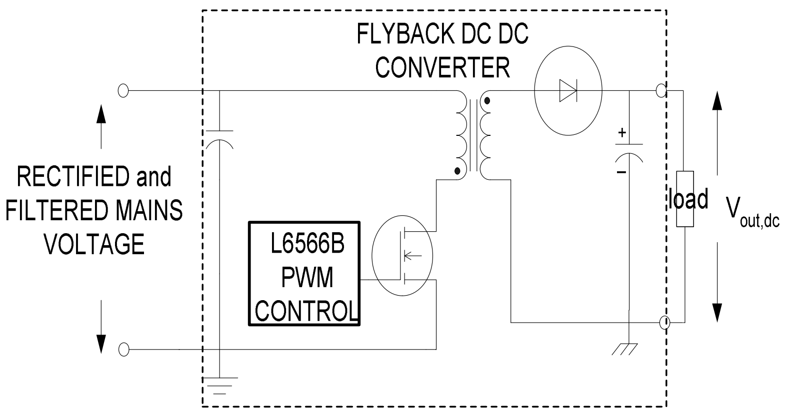

Figure 5.1 System Block Diagram (ST, 2008).

This AC-DC converter can work in continuous and discontinuous conduction mode with fixed frequency and variable duty cycle PWM. The nominal switching frequency is nearly 62 kHz. This switching frequency is chosen to arrive at a compromise between the transformer size and the harmonics of the switching frequency, minimizing the size of the input filter and reducing its cost. The oscillator is programmed externally by means of a resistor (R_T) connected between the OSC pin and the ground. With good approximation the oscillation frequency f_{OSC} is given by (ST, 2008)

$$f_{osc} \approx \frac{2.10^3}{R_T} \tag{5.1}$$

with f_{OSC} in kHz and R_T in kΩ.

The input of the converter is filtered with EMI Pi-filter. The switching component is a standard MOSFET that has a maximum of 600V-2Ω ratings requiring a small heat sink. The transformer is layer type that uses a standard ferrite type EER28L. The snubber circuit network consisting of the elements D7, R7, C21 in Figure 5.6 clamps the peak of the leakage inductance voltage spike. The energy stored in the leakage inductance is transferred to the capacitor C21, and when MOSFET is on it dissipated on resistor R7. The output rectifier diode has been selected according to the maximum reverse voltage, forward-voltage drop and power dissipation. So Schottky diode is used due to its low voltage drop and minimum power dissipation in comparison with the standard types. A small LC filter has been added to all output terminals in order to filter the high frequency ripple without increasing the output capacitors. The output voltage regulation is performed by secondary feedback sensing via the 12V output voltage. As implemented in Figure 5.2 TL431 is used in the feedback circuit as an error amplifier. TL431 drives an optocoupler SFH617A-4, insuring the required insulation between primary and secondary of the converter. The opto-transistor modulates directly the voltage on COMP pin of the L6566B (ST, 2008).

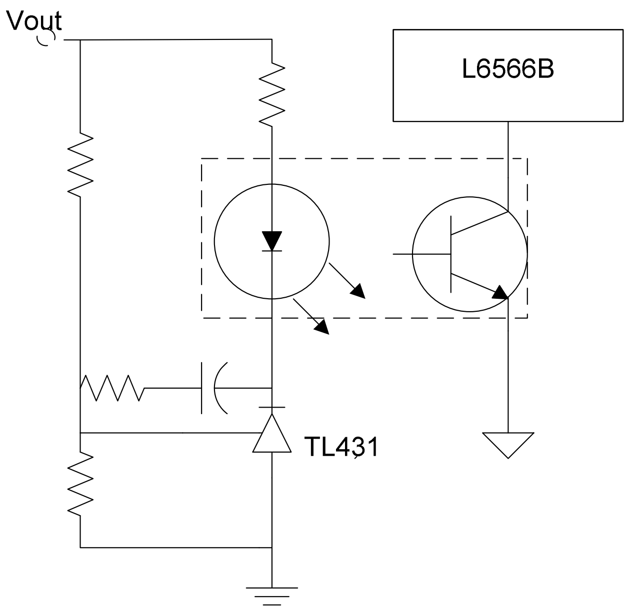

Figure 5.2 PWM Control Block for L6566B.

5.1.1 Electrical Characteristics of the Transformer

The parameters of the transformer are calculated by using the formulas given in section 3.2.1.2. The transformer is a layer type, using a standard ferrite type EER28L. It has been designed according to the EN60065 norms. The operating frequency is typically 62 kHz. The primary inductance is 910 µH at 1 kHz - 0.25 V when measured between pin 1 and 3. The leakage inductance is 15 µH at 100 kHz - 0.25 V when measured between pin 1 and 3. Maximum peak primary current is 1.02 ampere. Figure 5.3 and Table 5.1 give the electrical diagram and winding characteristic of the transformer for the power converter designed with L6566B.

Table 5.1 Transformer winding characteristics

Pins	Winding	RMS current	Number of turns
3-1	Primary	0.30	95
12-10	12V	2	16
5-6	Auxiliary	0.05	17

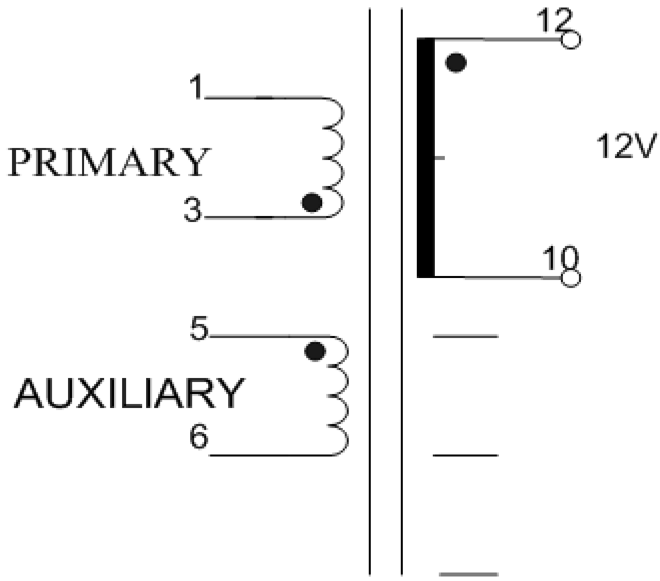

Figure 5.3 Transformer electrical diagrams.

5.1.2 Start-up Operation of the Circuit

The L6566B pin 1 (HVS) shown in Figure 5.4 is directly connected to the DC bulk voltage and at start-up, an internal high voltage current source charges C19 until the L6566B turn-on voltage threshold is reached, then the high voltage current source is automatically switched off. As the L6566B starts switching, it is initially supplied by the V_{CC} capacitor, and then the transformer auxiliary winding provides the voltage to power the IC. Because the L6566B integrated high voltage start-up circuit is turned off, it is not dissipative during normal operation and has a significant role to reduce the power consumption when the power supply operates at light load.

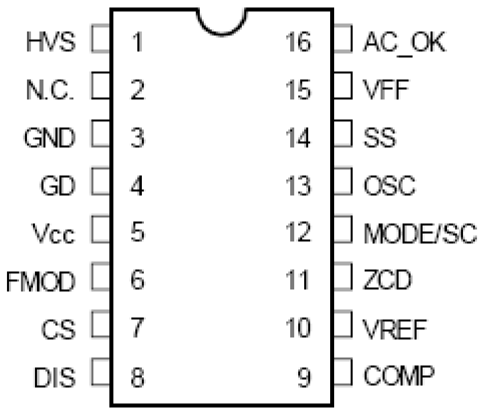

Figure 5.4 Pin connections (ST, 2008).

5.1.3 Frequency Modulation Circuit

To improve the EMI behavior of the application and to minimize the size of the EMI filter, the L6566B is provided with a dedicated pin. This pin allows the designer to modulate the oscillator frequency and gives the possibility to select both the modulation frequency and the modulation index. It is advantageous to modulate its switching frequency, so that the resulting spread-spectrum behavior distributes the energy of each harmonic of the switching frequency over a number of side-band harmonics as mentioned in Chapter 4 (ST, 2008).

As it is depicted in Figure 5.5, the capacitor C_{MOD} is connected between the FMOD pin and the ground and is alternately charged and discharged between 0.5 and 1.5 V by internal current generators sourcing and sinking the same current (three times the current defined by the resistor R_T at the OSC pin) (ST, 2008).

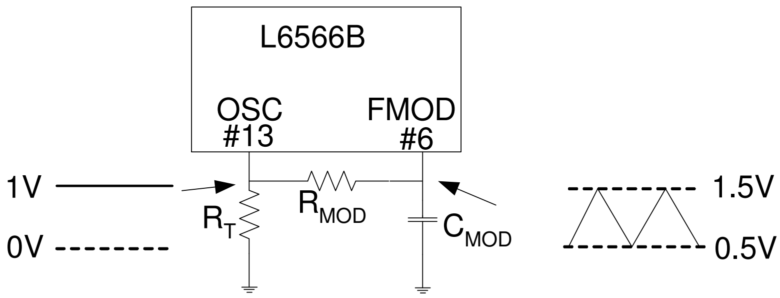

Figure 5.5 Frequency Modulation circuit (ST, 2008).

Hence, the voltage across the capacitor C_{MOD} will be a symmetric triangle, whose frequency f_m is determined by C_{MOD}. By connecting a resistor R_{MOD} between the FMOD and OSC pins, the current sourced by the OSC pin will be modulated according to a triangular profile at a frequency f_m (ST, 2008). If R_{MOD} is considerably higher than R_T, as normally both f_m and the symmetry of the triangle will be little affected. With this arrangement it is possible to set the frequency deviation Δf_c and the modulating frequency f_m, which define the modulation index given by Equation (4.10).

The maximum and minimum values of the switching frequency of the converter which corresponds to the carrier frequency (f_c) in the analysis of Chapter 4 are directly related with the frequency deviation. Minimum switching frequency, $f_{c,min}$, that occurs on the peak of the triangle and the maximum switching frequency, $f_{c,max}$, that occurs on the valley of the triangle will be symmetrically placed around the center value f_c, and so (ST, 2008)

$$f_{c,\min} = f_c - \frac{1}{2}\Delta f_c \tag{5.2}$$

$$f_{c,\max} = f_c + \frac{1}{2}\Delta f_c \tag{5.3}$$

Then, R_T will be found from Equation (5.1) while R_{MOD} and C_{MOD} can be calculated as follows (ST, 2008).

$$R_{MOD} = \frac{2.10^3}{\Delta f_c} \tag{5.4}$$

$$C_{MOD} = \frac{75}{f_m} \tag{5.5}$$

where Δf_c and f_m are in kHz, C_{MOD} is in nF and R_{MOD} is in kΩ. They will be selected by the designer according to circuit performance so to achieve the best compromise between attenuation of peak EMI emissions and clean converter operation (ST, 2008).

In the designed circuit CMOD and RMOD correspond to C36 and R31, respectively. Different resistor and capacitor values resulting different FM parameters are tried in order to get an optimal EMI spectrum. In Figure 5.6, the schematic and component values of the experimental set up are given. The photograph of the designed circuit is shown in Figure 5.7. The schematic and related printed circuit board is designed by using Zuken schematic program.

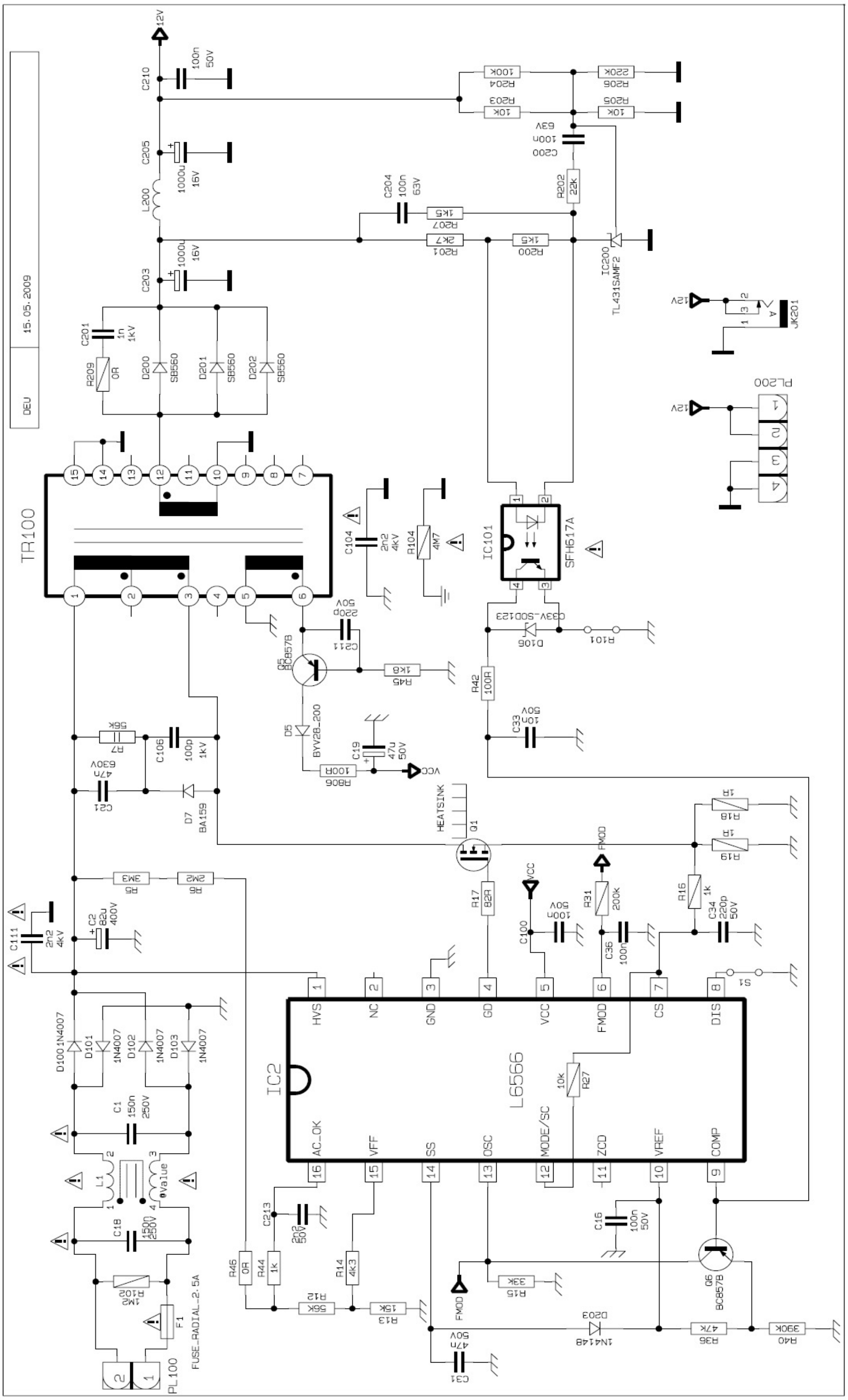

Figure 5.6 Circuit schematic.

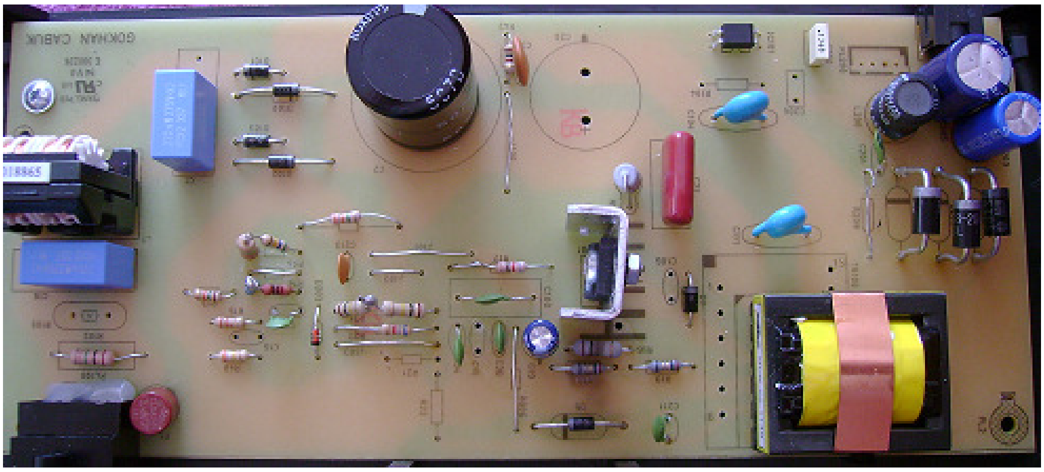

Figure 5.7 A photo of the realized flyback converter.

5.2 Description of Test Platform

Test platform shown in Figure 5.8 has been set up in order to measure the conducted emission, whose test results have been taken between the frequency ranges of 150 kHz – 30 MHz, which is regulated by the CISPR. Figure 5.9 shows the conducted emission test limits for EN55013. A line impedance stabilization network (LISN) has been inserted between the AC power cord of the device under test (DUT) and the mains power supply while testing the flyback converter.

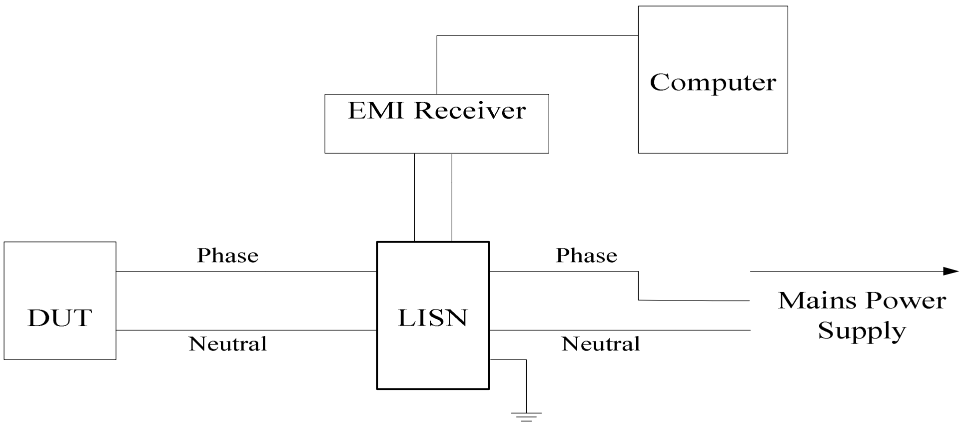

Figure 5.8 Diagram of the test setup used for measuring conducted emission.

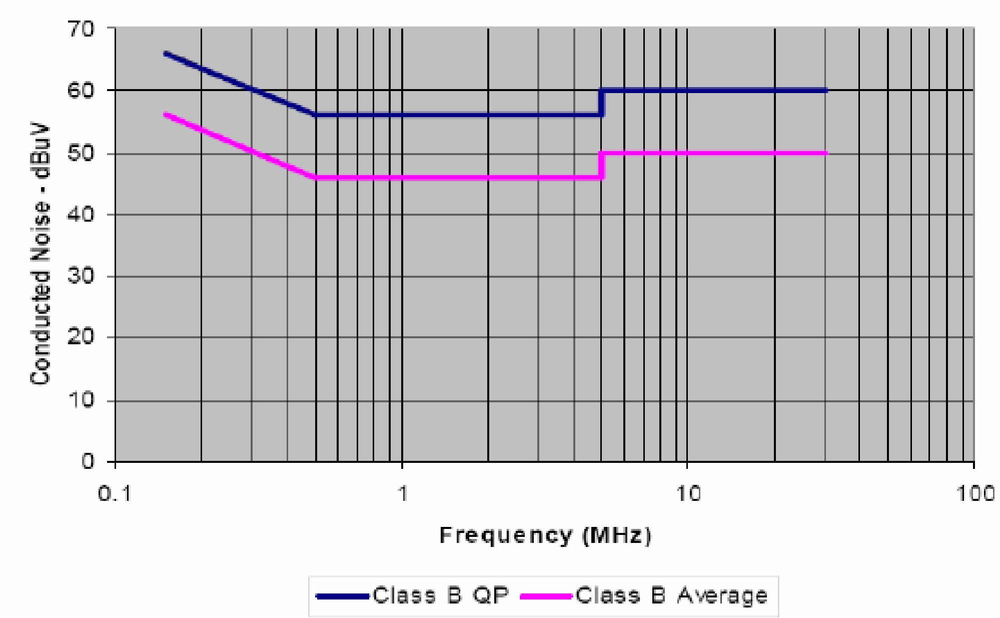

Figure 5.9 EN55013 conducted emission test limits.

Mains power supply is filtered through the LISN, so the device power is provided with unpolluted AC power supply. An EMI receiver is connected to the LISN measuring the conducted emission noises from DUT. EMI receiver has a 9 kHz resolution bandwidth and capable of taking average (AV) and quasi peak (QP) values of the signal spectrum.

5.3 Flyback Converter Operation Results

The waveforms shown in Figures 5.10 and 5.11 are obtained for different load conditions of the flyback converter. From the drain current waveform in Figure 5.10, it is possible to conclude that the converter is working in continuous mode. This operating mode has been chosen in order to optimize the output filter capacitors and the peak-to-rms ratio of the current flowing in the transformer windings (ST, 2008). The measured switching frequency is 63 kHz. As the load increases the switching frequency value remains the same whereas the PWM duty cycle increases.

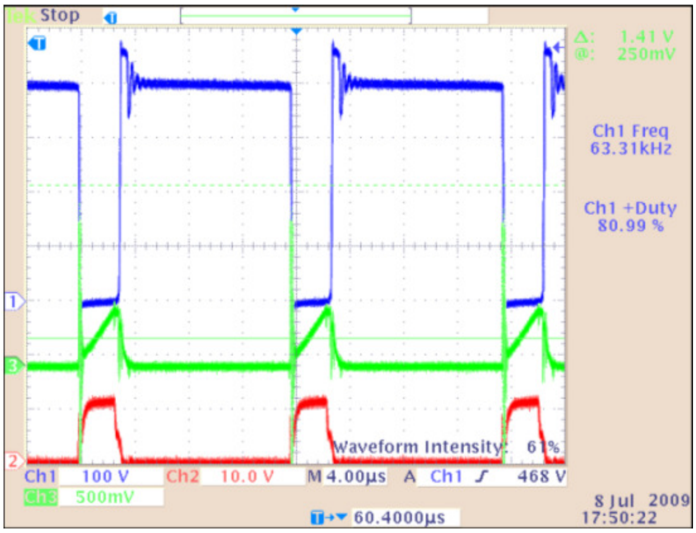

Figure 5.10 Waveform at 220V AC - 50 Hz - full load

CH1: Drain voltage (100V/div), CH2: Gate voltage (10V/div),

CH3: Drain current (500mA/div)

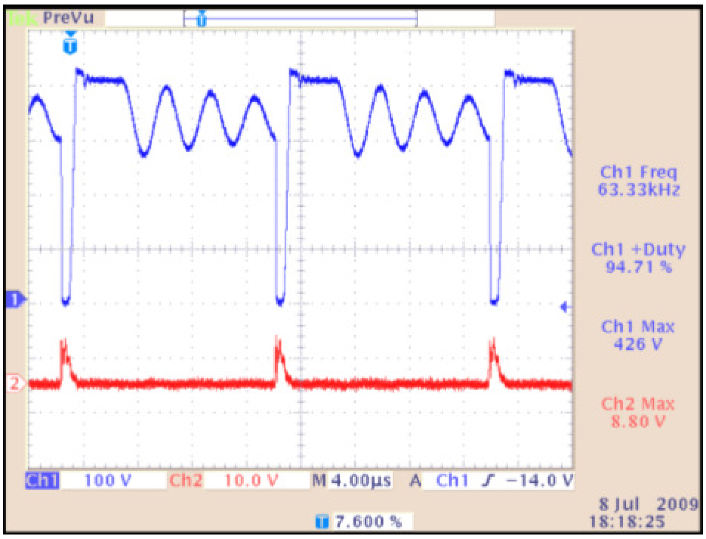

Figure 5.11 Waveform at 220V AC - 50 Hz – 4W

CH1: Drain voltage (100V/div), CH2: Gate voltage (10V/div)

The output voltage and power of the converter measured at 220V AC mains supply and 1.9A output current are 11.83V and 22.47W, respectively. The measured input power of the converter is 28.27W. So the overall efficiency is calculated as 79.47%. The output voltage and power of the converter at the 0.05A load current are 11.99V and 0.6W. The efficiency of the converter is 68.49% at the measured 0.876W input power.

Figures 5.12 and 5.13 show the deviation of the frequency after the FM technique is applied. It is observed in the experimental tests that as the amplitude of the modulating signal increases the deviation of the signals also increases as it is expected.

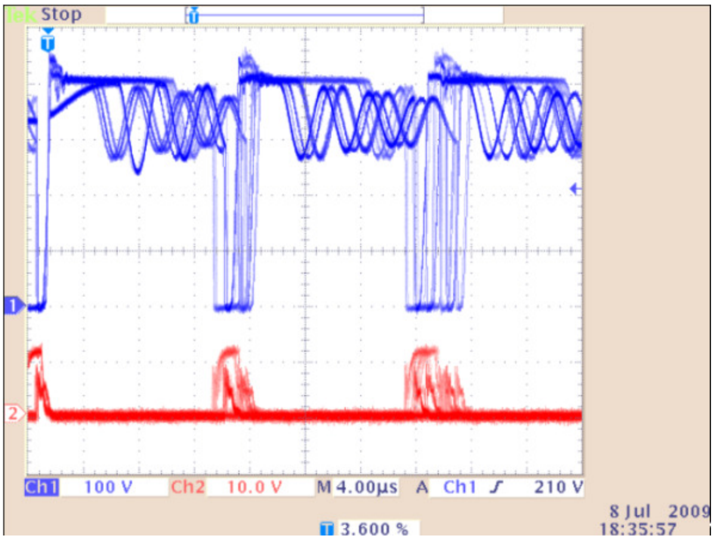

Figure 5.12 Drain and gate signals at light load after applied frequency modulation (time/div: 4 μs) CH1: Drain voltage (100V/div), CH2: Gate voltage (10V/div).

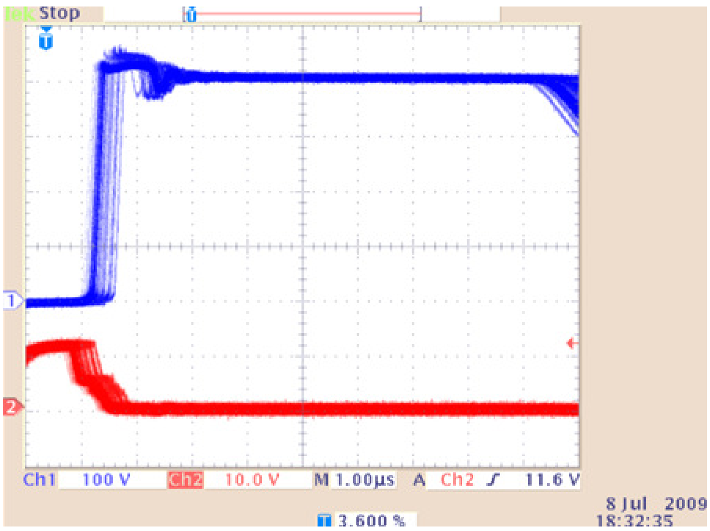

Figure 5.13 Drain and gate signals at light load after applied frequency modulation (time/div: 1 μs) CH1: Drain voltage (100V/div), CH2: Gate voltage (10V/div).

The output voltage and power of the converter measured after modulation at 220V AC mains supply and 1.9A output current are 11.83V and 22.47W, respectively. The measured input power of the converter is 28.30W. So the overall efficiency is 79.38%. The output voltage and power of the converter at the 0.05A load current are 12V and 0.6W after modulation. The efficiency of the converter is 68.65% at the measured 0.874W input power. It is evident from these results that the converter operates properly after the FM technique is implemented and nearly the same efficiency values are obtained. For the continuous mode operation of the flyback converter, input-output relationship can be written as (Lee, 1993)

$$\frac{V_{out}}{V_{in}} = \frac{N_s}{N_p}\frac{D}{1-D} \tag{5.6}$$

where N_p and N_s are the number of turns in the primary and secondary windings, respectively and D is the duty cycle ($D \leq 1$). As it is seen from Equation (5.6), the output voltage depends on the duty cycle of the PWM signal. It has been observed from the experimental results that the duty cycle of the PWM signal remains unchanged after FM method is applied as it is expected. Therefore, there will be no change in the magnitude of the output voltage by implementing the FM technique.

5.3 Flyback Converter Conducted Emission Results

Figure 5.14 shows the conducted noise measurement results at 220 V_{AC} mains voltage. The green solid lines show the EMI measurement before modulation and dashed red lines show the measurements after modulation. The peaks of harmonics of the switching frequency before modulation can be easily seen in this figure.

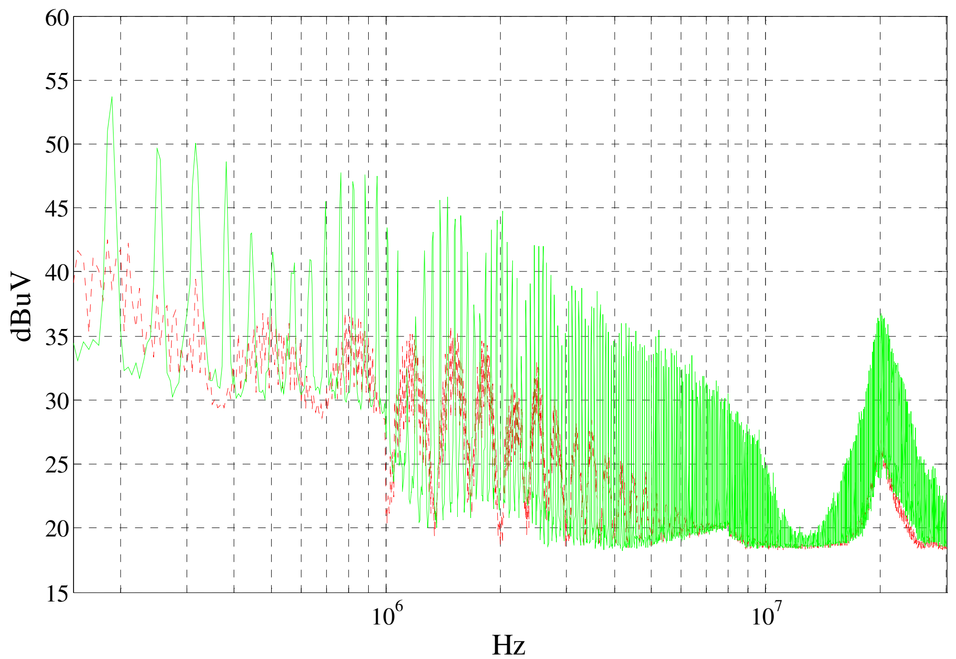

Figure 5.14 Conducted noise figures before and after modulation with R_{MOD}=50kΩ C_{MOD} =100nF green: before modulation; red: R_{MOD}=50kΩ and C_{MOD}=100nF.

Table 5.1 EMI measurement results before FM

Frequency (kHz)	**Level of peaks (dBµV)**
190	53.46
250	49.08
315	50.73
380	47.86
760	47.57
820	47.50
885	48.33
950	47.08

Table 5.2 EMI measurement results after FM

Frequency (kHz)	**Level of peaks (dBµV)**
155	40.04
170	41.91
185	43.19
200	42.16
210	41.22
225	38.86
250	37.33
315	39.84

The reduction in the noise peaks obtained using the FM technique is clearly visible. The results that are taken after modulation show that there is nearly 10dBμV attenuation at the peak values. For an accurate comparison between the EMI measurement results before and after modulation, the values recorded by the EMI receiver are given in Tables 5.1 and 5.2. It is also observed from the table the frequency that has a maximum peak value is not seen after modulation. There are other frequency components with the lower amplitudes due to spread spectrum.

The tests are repeated for different frequency modulation (f_m) and frequency deviation (Δf_c) values and the results are given in Figures 5.15 and 5.16. In order to obtain the best performance on the spectrum, the R_{MOD} and C_{MOD} values are changed. The solid green lines in Figure 5.15 show the measurement with R_{MOD}=100kΩ and C_{MOD}=1nF. The dashed red lines show the measurement with R_{MOD}=100kΩ and C_{MOD}=200nF.

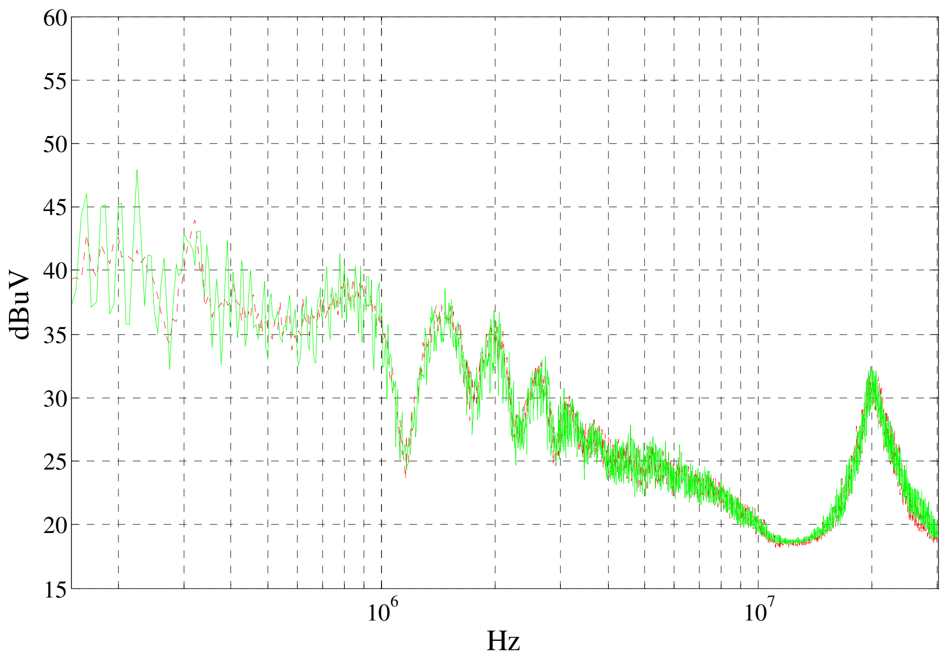

Figure 5.15 Waveform with $\Delta f_{c=}$20 kHz f_m=375Hz and f_m=75 kHz. red: R_{MOD}=100kΩ and C_{MOD}=200nF; green: R_{MOD}=100kΩ and C_{MOD}=1nF ;.

Table 5.3 EMI measurement results with R_{MOD}=100kΩ and C_{MOD}=200nF

Frequency (kHz)	**Level of peaks (dBμV)**
165	40.62
180	39.73
200	40.68
210	41.17
225	41.68
235	41.14
320	44.19
335	39.69

Table 5.4 EMI measurement results with R_{MOD}=100kΩ and C_{MOD}=1nF

Frequency (kHz)	**Level of peaks (dBμV)**
165	46.87
185	45.91
205	44.92
225	48.90
300	41.68
330	44.66
345	41.68
390	43.04

In Figure 5.15, it is observed that while the frequency deviation is constant (without changing R_{MOD}), decreasing the f_m frequency (increment in C_{MOD}) increases the reduction level of the EMI noise's peak levels. The effect of the modulation decreases at the higher frequencies.

The measurements in Figure 5.16 are taken at the constant f_m value and different frequency deviations. The solid green lines show the measurement with R_{MOD}=200kΩ and C_{MOD}=100nF. The dashed red lines show the measurement with R_{MOD}=50kΩ and C_{MOD}=100nF.

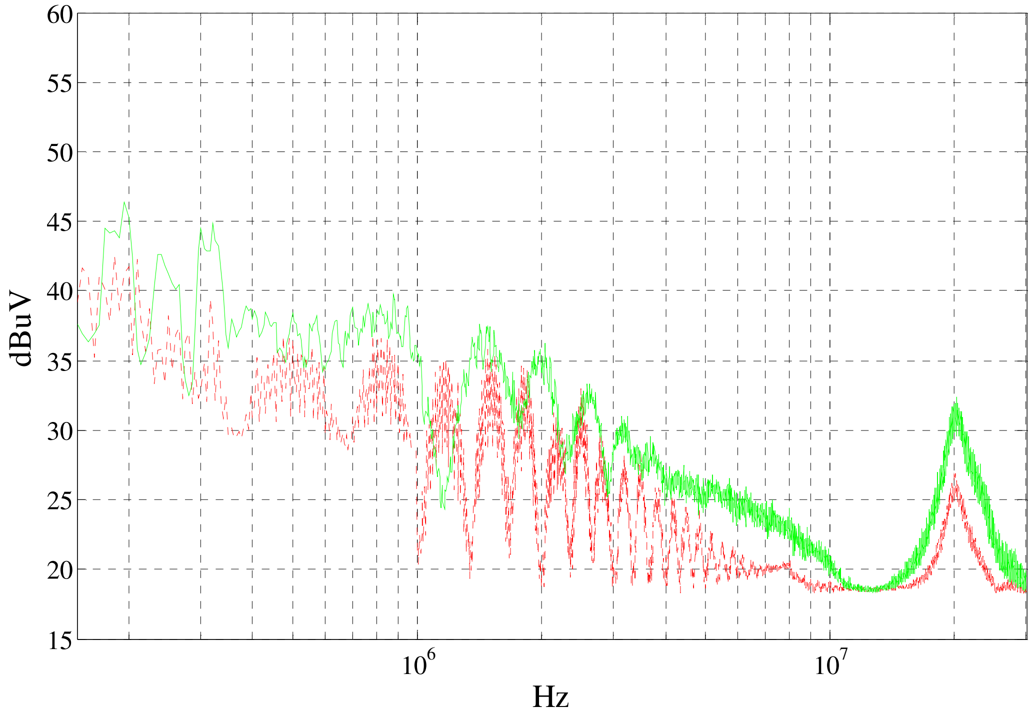

Figure 5.16 Waveform with f_m=750Hz Δf_{c}=10kHz and Δf_{sw}=40kHz, green: R_{MOD}=200kΩ and C_{MOD}=100nF ; red: R_{MOD}=50kΩ and C_{MOD}=100nF.

Table 5.5 EMI measurement results with R_{MOD}=200kΩ and C_{MOD}=100nF

Frequency (kHz)	**Level of peaks (dBµV)**
175	42.48
185	45.33
195	45.61
235	43.11
265	38.31
300	43.59
320	44.12
875	38.94

Table 5.6 EMI measurement results with R_{MOD}=50kΩ and C_{MOD}=100nF

Frequency (kHz)	**Level of peaks (dBµV)**
155	40.04
170	41.91
185	43.19
200	42.16
210	41.22
225	38.86
250	37.33
315	39.84

In Figure 5.16, it is observed that while the f_m frequency is constant (without changing C_{MOD}) the increase of the frequency deviation (reduction in R_{MOD}) attenuates amplitudes of the EMI noises. As the frequency deviation increases the measured peak values of the EMI noise decreases.

CHAPTER SIX
APPLICATION OF FREQUENCY MODULATION TECHNIQUE TO DC-DC FLYBACK CONVERTER

6.1 Description of the Circuit

In this chapter, a 5W flyback converter that is driven by an FM modulated PWM signal has been designed. A signal generator is used in order to modulate the switching signal and the spectral component of the power converter is measured with spectrum analyzer and test results are reported. Block diagram of the converter is given in Figure 6.1.

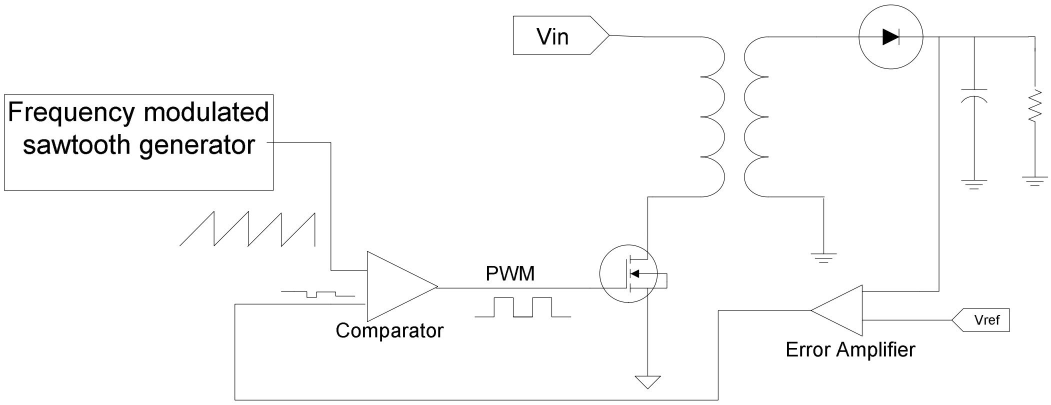

Figure 6.1 Block diagram of the converter.

This is a classical DC-DC converter that accepts a DC input supply voltage between 16V-32V. Nominal working condition is 18V and delivers 5V output voltage with 1A load current. The electrical characteristics are given in Table 6.1.

Table 6.1 Electrical characteristic of the DC-DC converter

Minimum Input Voltage	$16V_{dc}$
Maximum Operating Voltage	$32V_{dc}$
Nominal Output Voltage	5V
Maximum Output Power	5W

6.1.1 Control Mechanism and FM Circuit of the Converter

The most important consideration while building a flyback converter is designing the control mechanism and transformer model in order to satisfy the operation requirements. The required sawtooth signal is generated as discussed in Section 3.2.1.1. The sawtooth signal sets the duty cycle by defining the on time duration of power switch MOSFET with a comparator which compares the error signal coming from the error amplifier and sawtooth signal. In order to obtain required signals, below circuit given in Figure 6.2 is built.

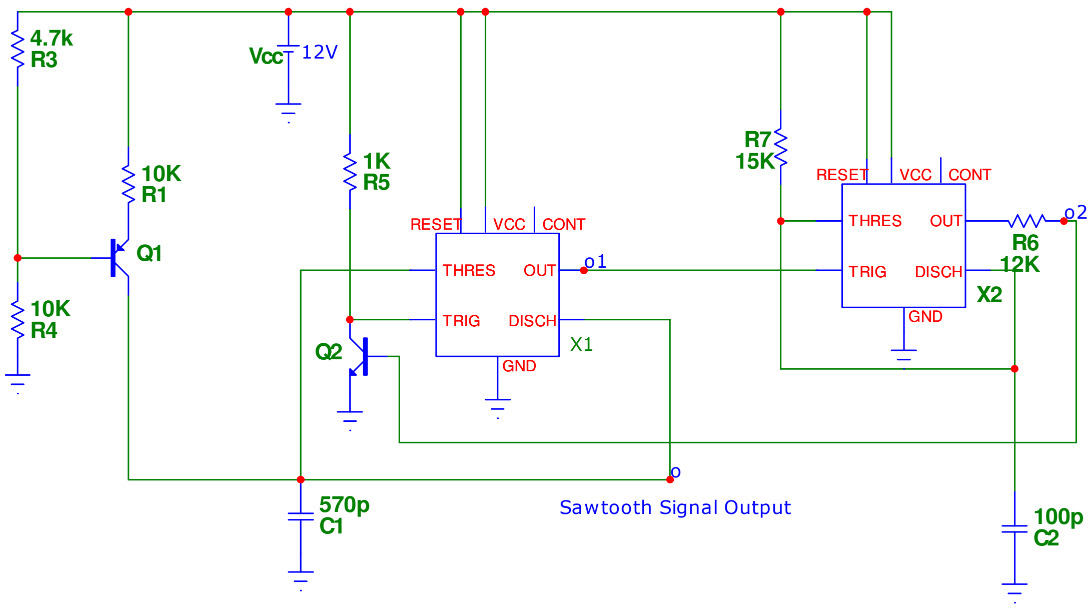

Figure 6.2 Sawtooth generator circuit.

This circuit has two monostable 555 timers that trigger each other. The resistors R1, R3, R4 and the transistor Q1 built a constant current source that charges the capacitor C1 till its voltage reaches the 2/3 of the supply voltage Vcc. During the time that C1 is being charged, the output of X1 remains high. When the threshold voltage on C1 exceeds 2/3 of Vcc the timer's internal discharge transistor turns on, lowering the voltage on C1. During this time, the 555 output is maintained low. If a low signal, which is at least 1/3 of Vcc, is not applied to the trigger pin of X1 then its output remains always low. Hence a second 555 timer, X2, is built to drive the trigger pin of the X1. When the trigger pulse voltage that falls below Vcc/3 is applied to the pin while the output of X1 is low, the timer's internal flip-flop turns the internal discharging transistor off and causes the timer output to become high by charging the capacitor C1. The output of X1 is connected to the trigger input of X2 in order to fulfill the same operation mentioned above. The base and emitter voltages of Q1 are calculated as (neglecting the base current)

$$V_{B1} = \frac{R_4}{R_3 + R_4} Vcc = 8.16V \tag{6.1}$$

$$V_{E1} = V_{EB1} + V_{B1} = 8.86V \tag{6.2}$$

The collector current I_C is found from below equation

$$I_C = \frac{Vcc - V_{E1}}{R_1} = 0.314mA \tag{6.3}$$

The switching frequency, f_c, of the converter is adjusted as 67 kHz. In order to adjust the maximum voltage level of the sawtooth and the value of the capacitor the basic calculation can be made

$$I_C = C_1 \frac{dV_{C1}}{dt} \tag{6.4}$$

$$0.314mA = C_1 \frac{\Delta V_{C1}}{1/67000} \tag{6.5}$$

Since ΔV_{C1}= (2/3)x12=8V, the capacitance value is calculated as 586pF. The closest available capacitor value which is 570pF is used. Since the capacitor is charged with a constant current source, the required sawtooth signal is obtained from the DISH pin where the C1 is also connected. Figure 6.3 shows the simulation results of the circuit obtained from Microcap program.

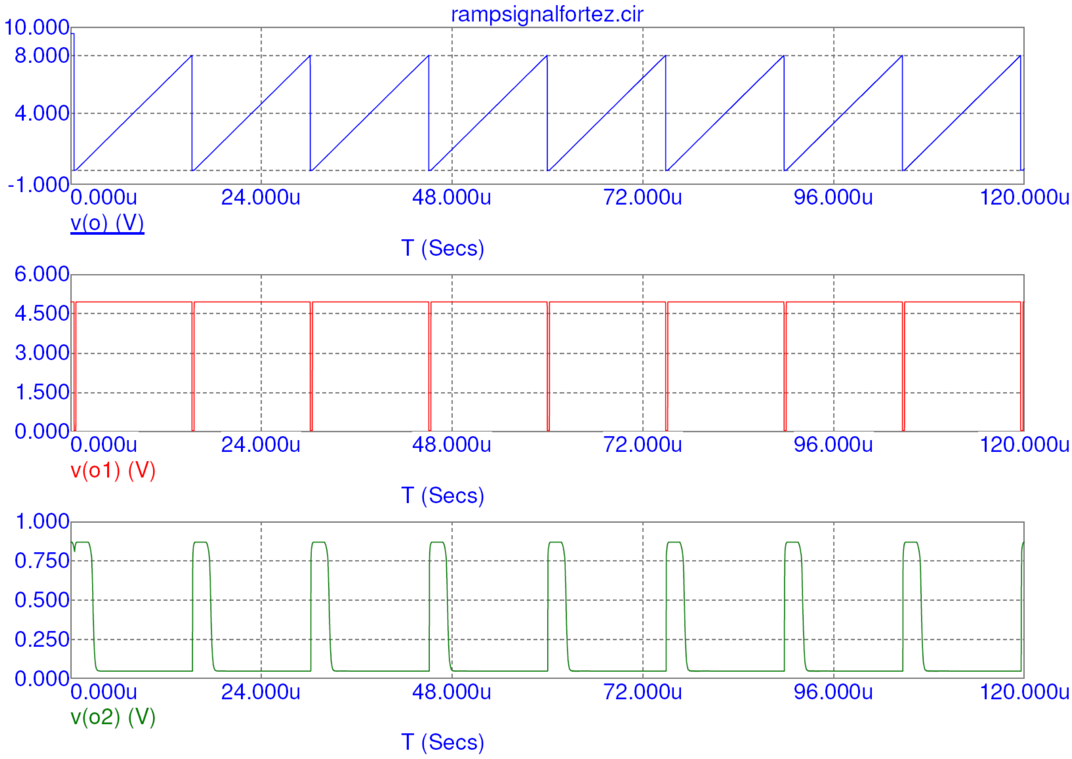

Figure 6.3 Sawtooth generator circuit analysis.

In order to implement a practical spread spectrum FM method, it is necessary to modify the sawtooth generator as a variable frequency signal. For this purpose, the circuit of Figure 6.4 is designed. Signal generator is used to obtain triangular modulating signal. Instead of supplying the emitter side of the transistor Q1 with constant voltage (12V), we use a triangular waveform swinging between two voltage levels with an offset in order to generate FM modulated sawtooth signal. Hence the maximum and minimum value of its frequency is determined by the minimum and maximum amplitudes of the triangular waveform. Figures 6.5 and 6.6 show the simulation results of the circuit with different slopes (s) of the triangular modulating signal.

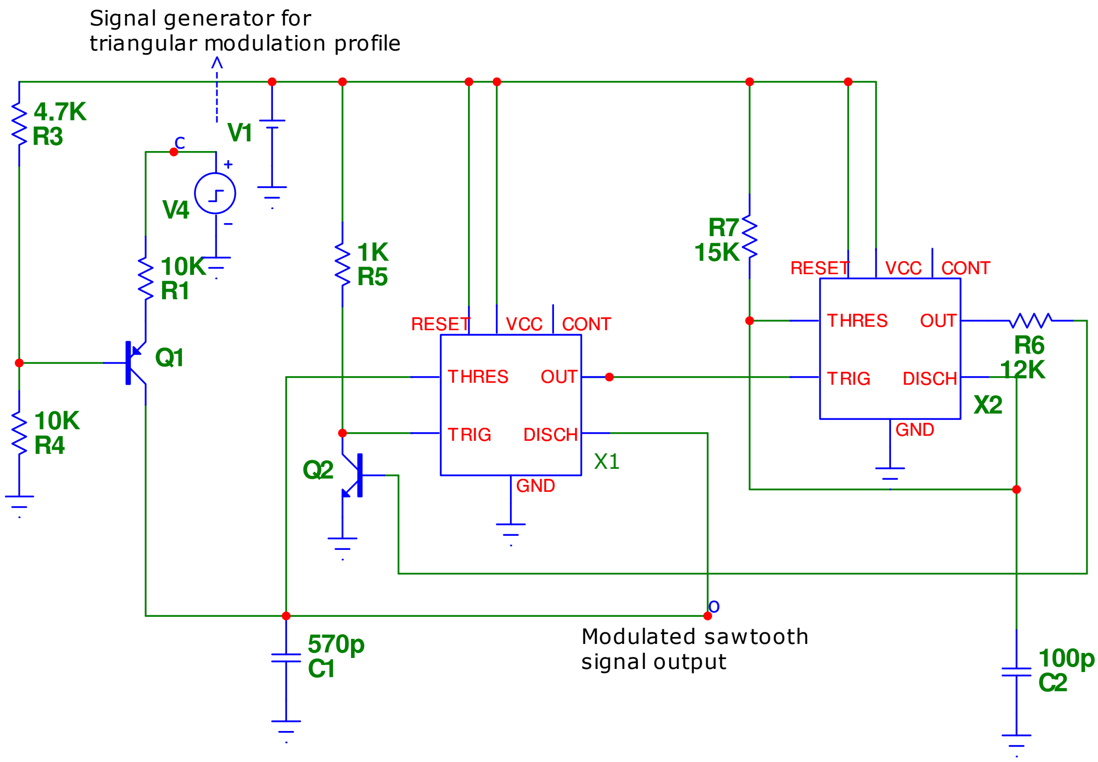

Figure 6.4 Frequency modulated sawtooth waveform.

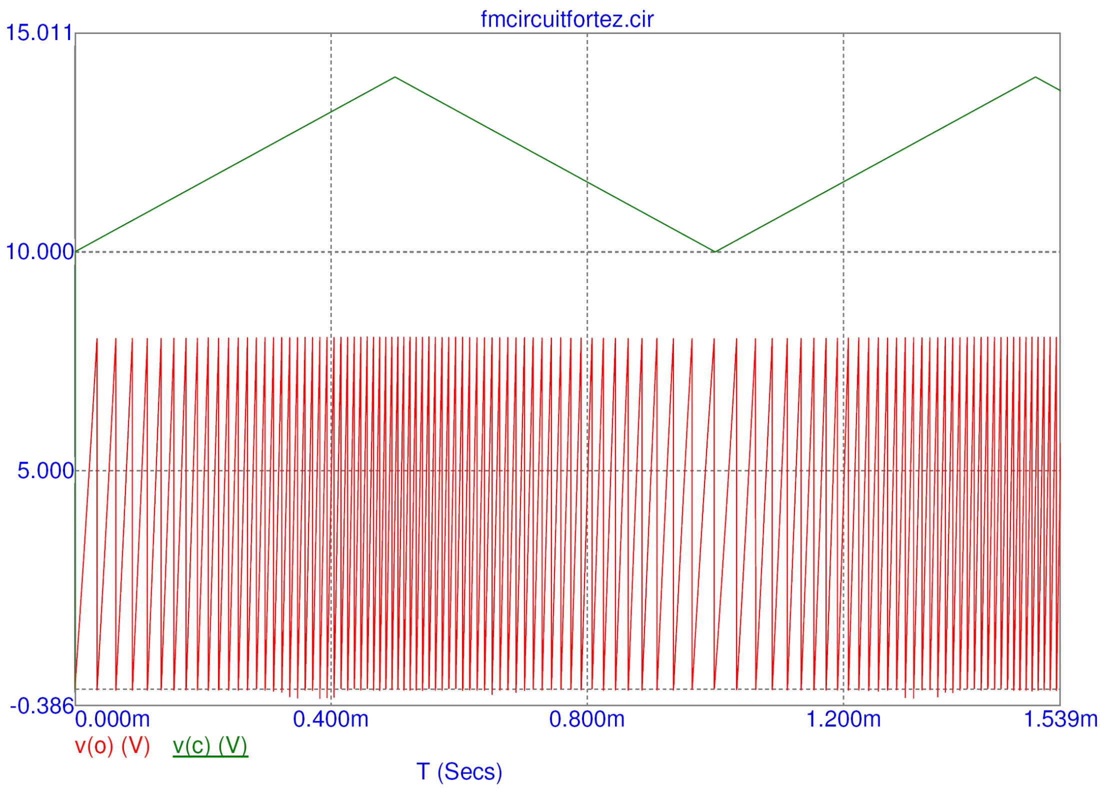

Figure 6.5 Frequency modulated sawtooth waveform with f_m=1 kHz f_c=67 kHz, s=0.5.

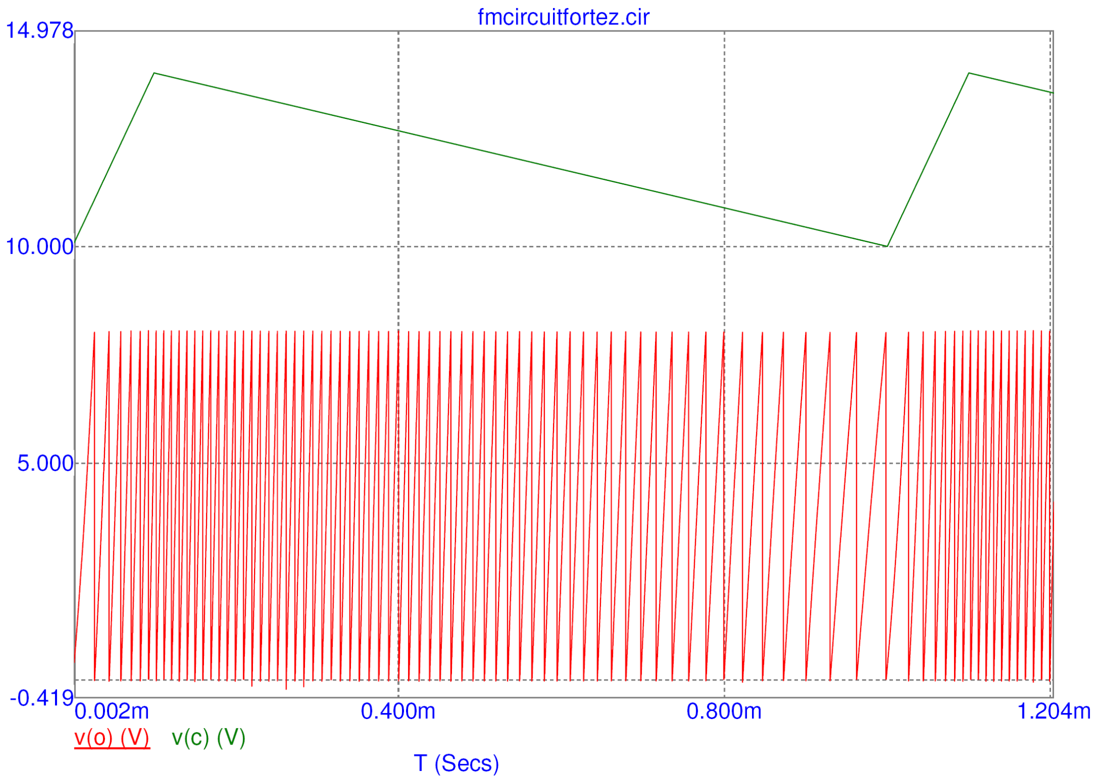

Figure 6.6 Frequency modulated sawtooth waveform with f_m=1 kHz f_c=67 kHz, s=0.125.

In order to obtain PWM signal, generated FM modulated sawtooth signal is compared with the error signal that is coming from the error amplifier circuit at the secondary side of the converter given as a block diagram in Figure 6.1. The output voltage regulation is performed by a feedback sensing the 5V output. The feedback network uses a TL431 shunt regulator as an error amplifier which drives an optocoupler. COSMO1010 ensures the required isolation between the primary and the secondary. The optotransistor gives the required error voltage to the comparator. The related circuit and simulation results are given in Figures 6.7 and 6.8. In Figure 6.7, the output voltage of the secondary side of the converter is simulated with the source V9 which provides a 5V DC voltage, in order to make the analysis simpler. The obtained PWM signal shown in Figure 6.8 has varying frequency but constant duty cycle. Variation of the PWM frequency is dependent on the frequency and amplitude of the triangular modulating signal.

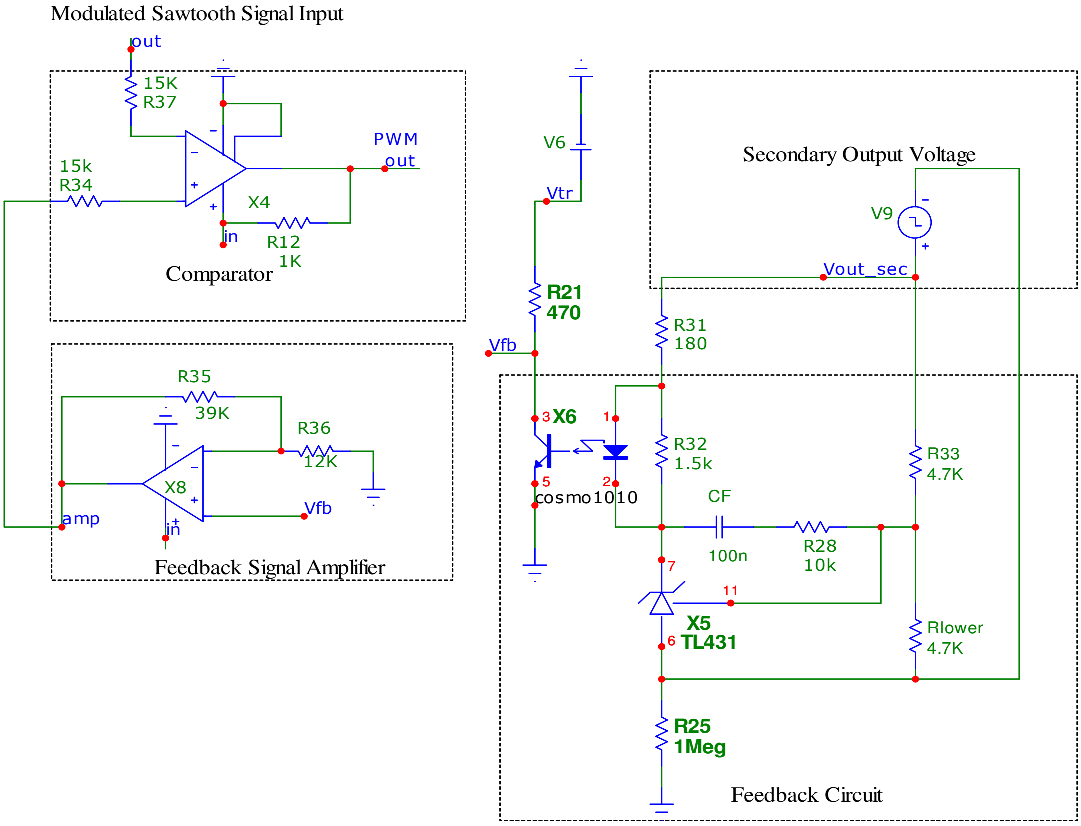

Figure 6.7 The comparator, amplifier and equivalent of the secondary feedback circuit.

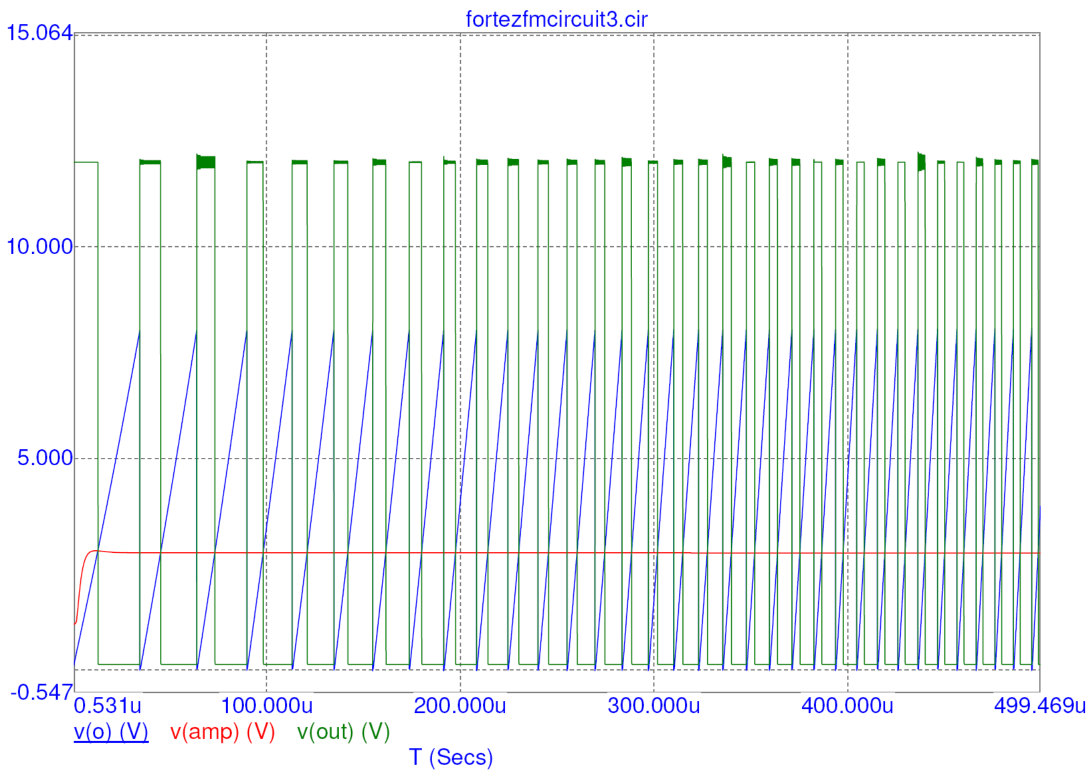

Figure 6.8 Generated PWM waveform.

6.1.2 Transformer Specifications

In this part, the parameters of transformer implemented to the board are given. The parameters are calculated based on the formulations given in Section 3.2.1.2. Table 6.2 shows the system parameters and their values. It is typical to select DC link capacitance as 2-3μF per watt of the output power.

Table 6.2 Defined system specifications

Minimum DC link voltage ($V_{DC,min}$)	16V
Maximum DC link voltage ($V_{DC,max}$)	32V
Maximum output power	5W
Maximum input power (The estimated efficieny is 85%)	5.9W
DC link capacitor	33μF
Reflected output voltage	20V

When designing a converter operating in the continuous mode, the maximum duty cycle is determined as (Hang-Seok, 2004)

$$D_{\max} = \frac{V_{RO}}{V_{RO} + V_{DC,\min}} = 0.56 \tag{6.6}$$

For discontinuous mode of operation, the maximum duty cycle should be chosen smaller than the value obtained in Equation (6.6). In this work, DC-DC flyback converter is designed to operate in the discontinuous mode and the duty cycle is selected as 0.4.

The primary side inductance is calculated from Equation (3.24) as (K_{RF}=1 for discontinuous mode)

$$L_m = \frac{(V_{DC,\min} D_{\max})^2}{2 P_{in} f_s K_{RF}} = 51.8 \mu H \tag{6.7}$$

The related current can also be calculated from Equation (3.27) as

$$I_{EDC} = \frac{P_{in}}{V_{DC,\min} D_{\max}} = 0.92 A \tag{6.8}$$

$$\Delta I = \frac{V_{DC,\min} D_{\max}}{L_m f_s} = 1.84A \quad (6.9)$$

Maximum peak drain current and rms drain currents are

$$I_{ds,peak} = (I_{EDC}) + (\frac{\Delta I}{2}) = 1.842A \quad (6.10)$$

$$I_{ds,rms} = \sqrt{\left[3(I_{EDC})^2 + (\frac{\Delta I}{2})^2\right]\frac{D_{\max}}{3}} = 0.671A \quad (6.11)$$

The proper switching device is chosen by considering the input power and current limits calculated. Table 6.3 shows the current limits of the selected MOSFET device which works properly with the system.

Table 6.3 Current limits of the chosen MOSFET

Minimum current limit of MOSFET	5.28A
Typical current limit of MOSFET	6.00A
Maximum current limit of MOSFET	6.72A
Maximum I_{over}	2.80A

The EFD2020S core is selected for the design. Its cross sectional area is 31mm^2 AL-value is 1370nH/turn^2. B_{sat} is chosen as 0.35T as stated in Chapter 3. To determine the proper core and the minimum primary turns, Equation 3.29 is used as

$$N_{P,\min} = \frac{L_m I_{over}}{B_{sat} A_e} \times 10^6 = 12.7 \text{ turn} \quad (6.12)$$

Determined number of turns for the output at the secondary and auxiliary windings by using Equations (3.30) and (3.32) given in Section 3.2.1.2 is

$$n = \frac{V_{RO}}{V_o + V_{F1}} = \frac{N_P}{N_{s1}} = 3.3 \qquad N_a = \frac{V_{cc} + V_{Fa}}{V_o + V_{F1}} N_{s1} = 13 \quad (6.13)$$

where the forward drop voltage of the diodes are accepted as 1V.

The number of turns for primary, secondary and auxiliary windings is 20, 6 and 13 respectively. The winding diagram of the transformer is shown in Figure 6.9.

With the determined turn number of the primary side winding, the gap length of the core is obtained using Equation (3.33) as

$$G = 40\pi A_e\left(\frac{N_P^2}{1000L_m} - \frac{1}{A_L}\right)(mm) = 0,\,2722 \text{ mm} \qquad (6.14)$$

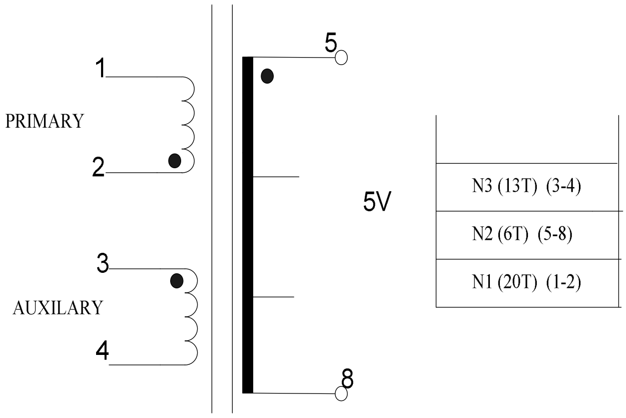

Figure 6.9 Winding diagram of the transformer.

Figure 6.10 shows a photograph of the converter built with discrete components and Figure 6.11 shows the schematic of the DC-DC flyback power converter.

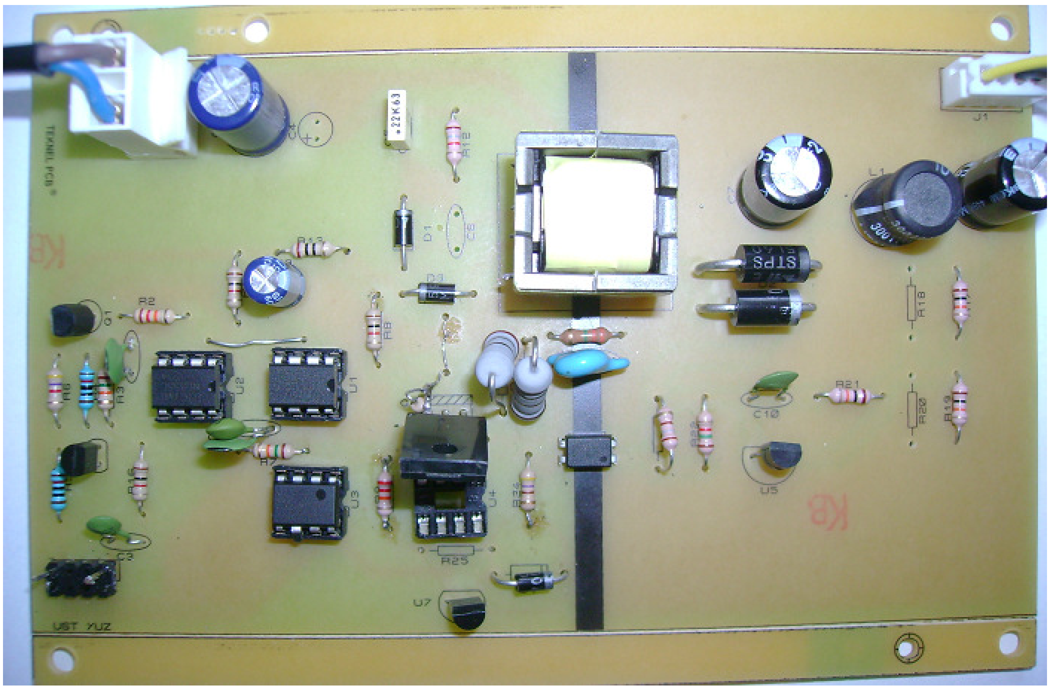

Figure 6.10 Photograph of the designed converter.

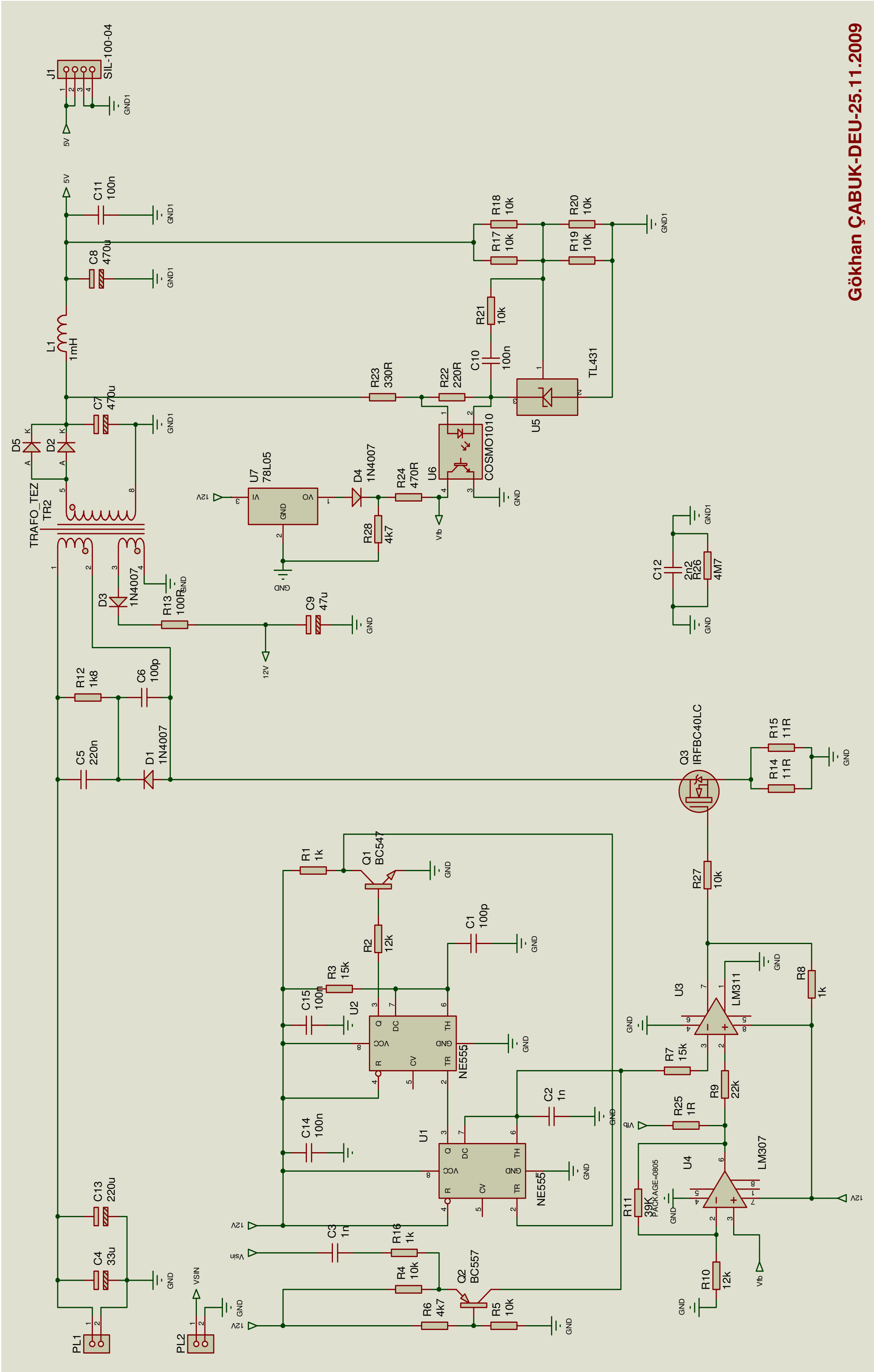

Figure 6.11 Circuit schematic.

6.2 Description of the Test Platform

The designed DC-DC flyback converter is tested for its EMI performance. For this purpose, the test platform shown in Figure 6.12 has been constructed. Modulating signal, obtained from a signal generator, is applied to the controller to generate an FM modulated PWM signal. Then the EMI noise coming from the DC-DC power converter is measured through a LISN which is designed for this work and recorded by the spectrum analyzer. Photograph of the test bench is shown in Figure 6.13.

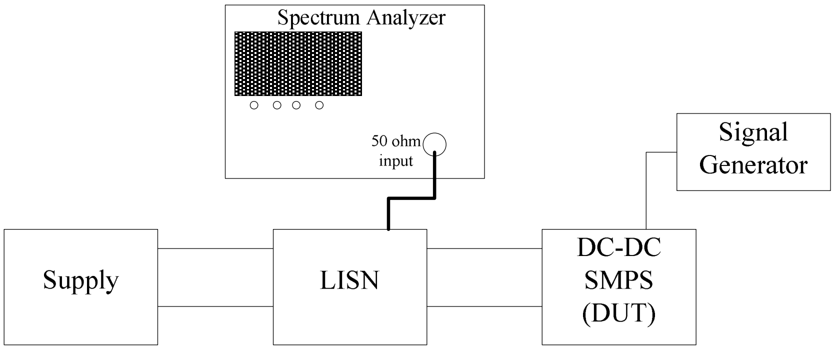

Figure 6.12 Test platform for the EMI analysis of the DC-DC converter.

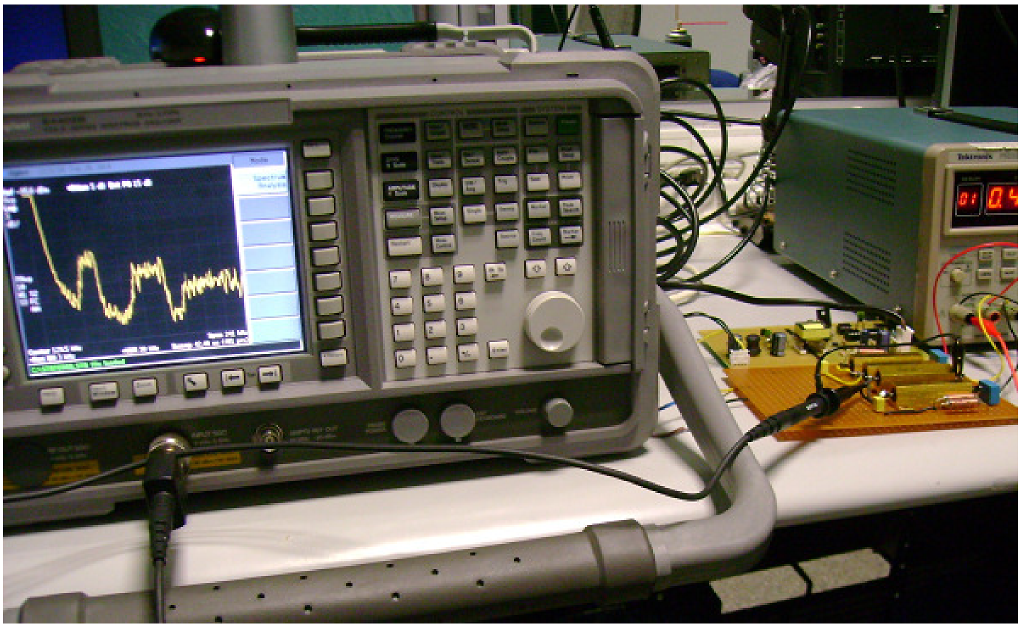

Figure 6.13 Photograph of the test set up.

The schematic diagram and photograph of the constructed LISN are shown in Figure 6 14 and Figure 6.15. The tests are made by inserting the designed LISN in series with the supply and DUT. The noise is measured across the 50Ω resistor which is connected to the 50Ω input of the analyzer.

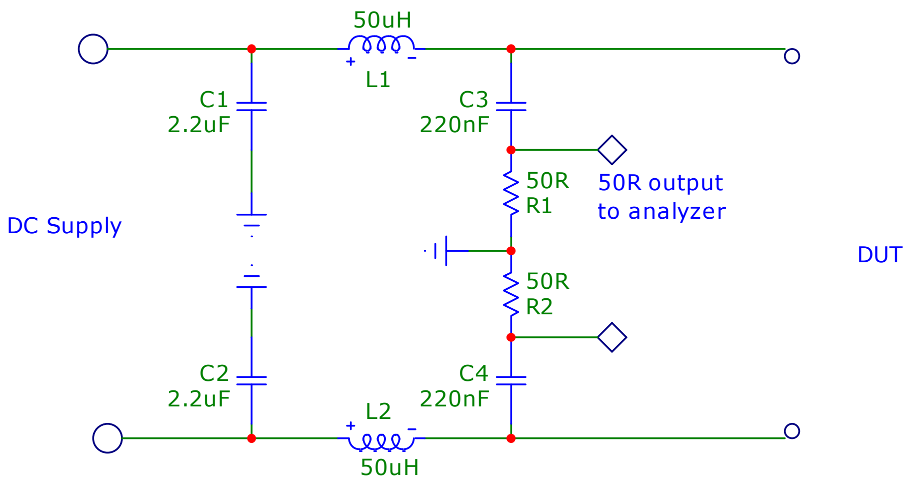

Figure 6.14 The schematic diagram of the designed LISN.

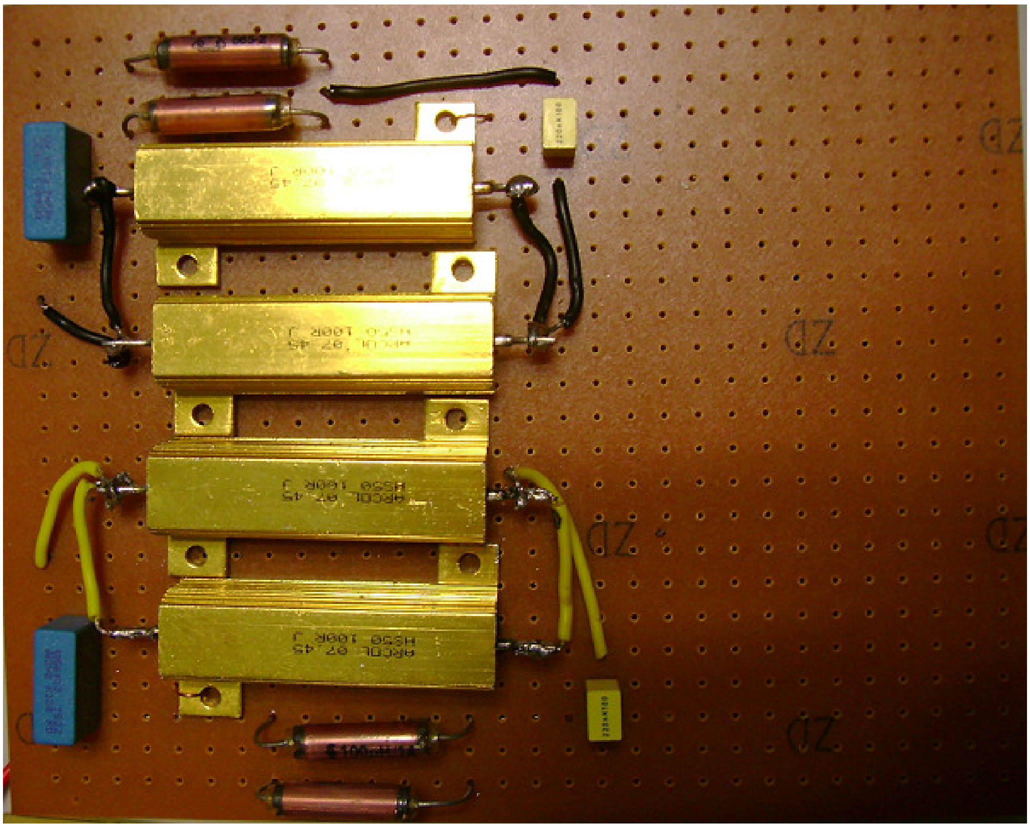

Figure 6.15 Photograph of the LISN.

6.3 Flyback Converter Operation Results

The following figures are taken during the operation of the converter. Figure 6.16 shows the switching PWM signal of the converter. The converter operates at 66.75 kHz switching frequency. The duty cycle of the converter is 48.35% at full load condition. Figure 6.17 shows the PWM duty cycle for the light load conditions. Duty cycle of the PWM is 17.75%.

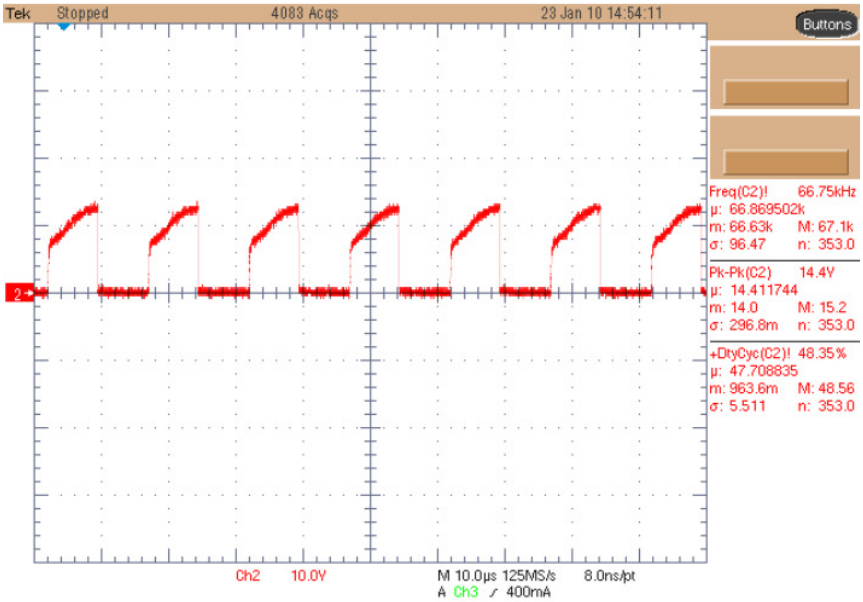

Figure 6.16 PWM signal at full load.

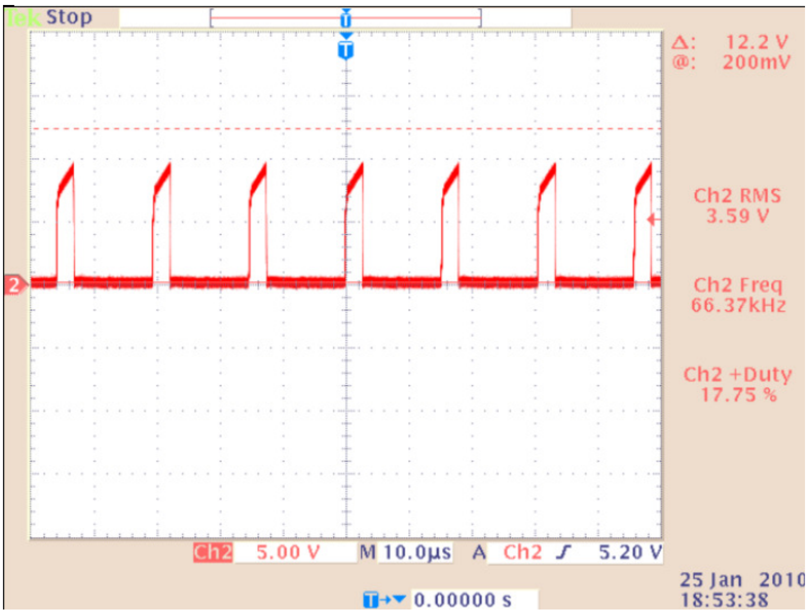

Figure 6.17 PWM signal for the light load condition.

Figure 6.18 shows the sawtooth waveform generated by the 555 timer integrated circuits and the feedback error voltage taken from the secondary side of the converter. These signals are used in order to obtain the PWM signal to drive the switching MOSFET component. Peak amplitude of the sawtooth signal is nearly 8V as explained in the previous section. The amplitude of the feedback signal and hence the PWM duty cycle changes regarding with the output voltage and load for the proper output regulation.

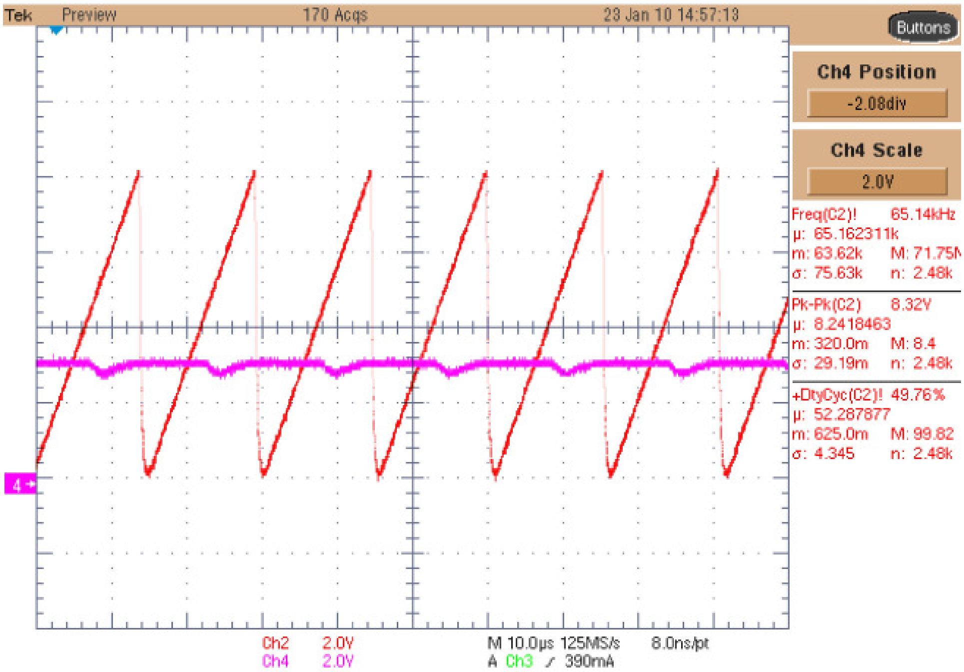

Figure 6.18 Generated sawtooth waveform and feedback signal.

Figure 6.19 depicts the drain current waveform of the converter which shows that the converter works in discontinuous mode.

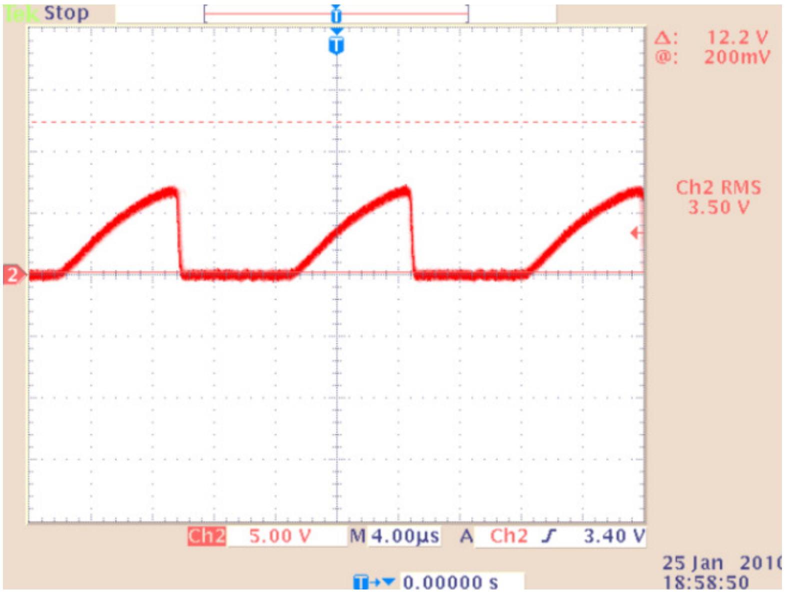

Figure 6.19 Drain current waveform.

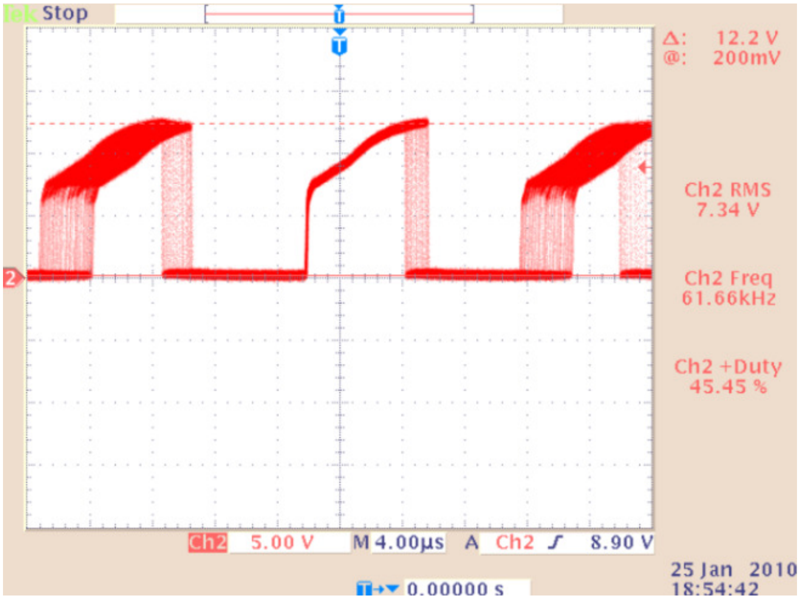

Figure 6.20 FM modulated PWM signal.

Figure 6.20 shows the deviation of the switching frequency after the FM technique is applied. The modulating frequency is 700Hz and the measured deviation is +/-5 kHz.

The output voltage and power of the converter measured at 18V DC input and 0.93A output current are 4.93V and 4.58W, respectively. The measured input power of the converter is 6.84W. So the overall efficiency is calculated as 67%. The output voltage and power of the converter after the application of the FM are 4.93V and 4.58W, respectively. The efficiency of the converter is 66% at the measured 6.96W input power. Two cases have nearly the same efficiency values. The experimental tests show the converter works properly after the modulation. For the discontinuous mode the input and output voltage relation is given in Equation (3.22). As it is seen from Equation (3.22), the output voltage depends on the duty cycle of the PWM signal. It has been observed from the experimental results that the duty cycle of the PWM signal remains unchanged after FM method is applied as it is expected. Therefore, there will be no change in the magnitude of the output voltage by implementing the FM technique.

6.4 Flyback Converter EMI Results

In this section, the spectra of the conducted EMI emissions from the DC-DC power supply taken across the designed LISN are presented. The EMI performance of the converter before and after the implementation of the FM technique is compared. Figures 6.21 and 6.22 show the conducted EMI noises without implementing FM for different frequency ranges and Table 6.4 shows the peak amplitudes of the noises obtained from Figure 6.21.

Table 6.4 Peak amplitudes of EMI emissions

Frequency (kHz)	Peak Amplitude (dBµV)
65.63	53.8
130.63	46.0
195.7	41.3
261.25	39.9
326.25	37.3
391.3	36.1
456.9	34.4

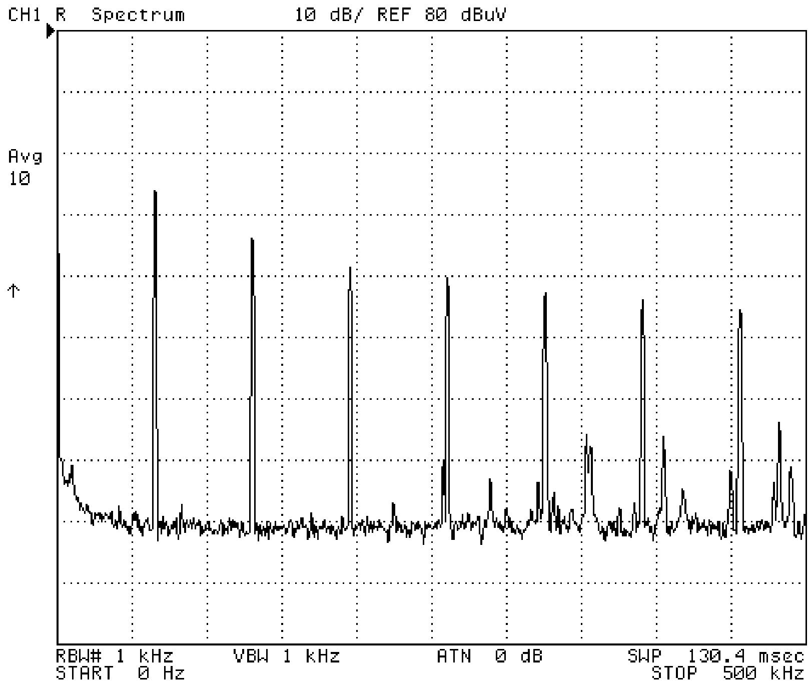

Figure 6.21 Spectrum of conducted EMI before FM, f_{start}-f_{stop}: 0-500kHz.

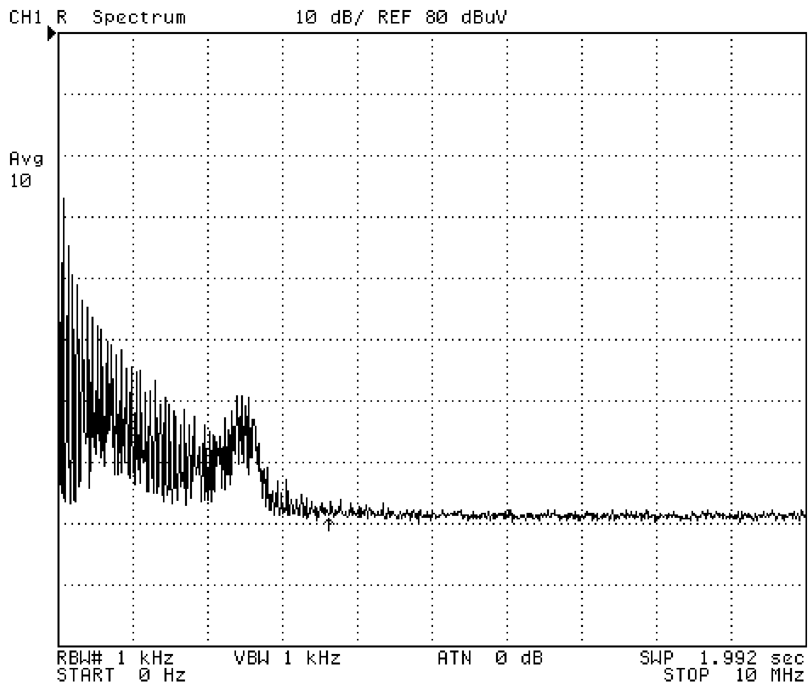

Figure 6.22 Spectrum of conducted EMI before the FM, f_{start}-f_{stop}: 0-10MHz.

As shown in Table 6.4 the maximum peak amplitude 53.8 dBμV and the second harmonic amplitude is 46 dBμV. The amplitude of the harmonic peaks decreases at the higher frequencies as it is seen in Table 6.4 and Figure 6.22.

Figures 6.23 and 6.24 show the comparison of the measurements of the conducted EMI emissions when no modulation is present (blue line) and with FM using triangular modulating signal (red line). The frequency and peak to peak amplitude of the triangular modulating signal is 800Hz and 1V, respectively.

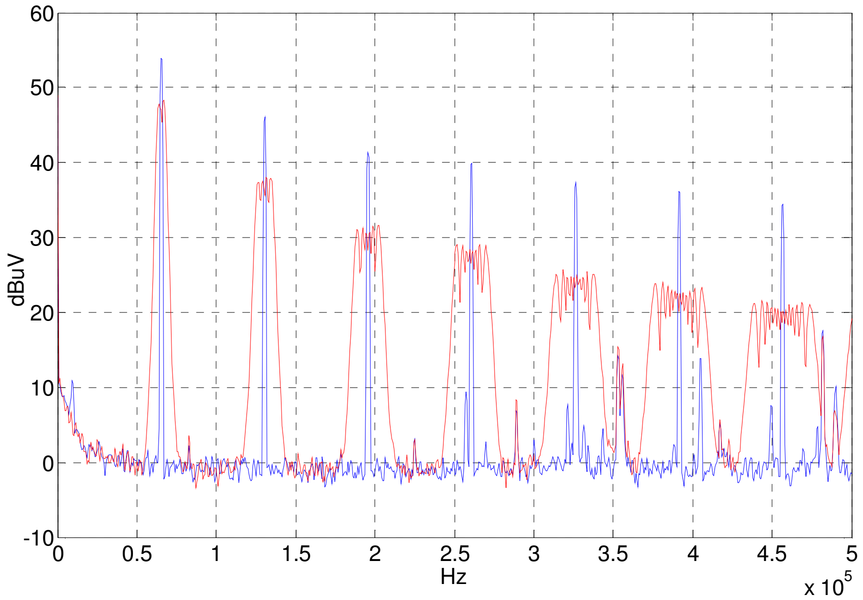

Figure 6.23 Comparison of the EMI performances with no modulation (blue line) and FM (red line).

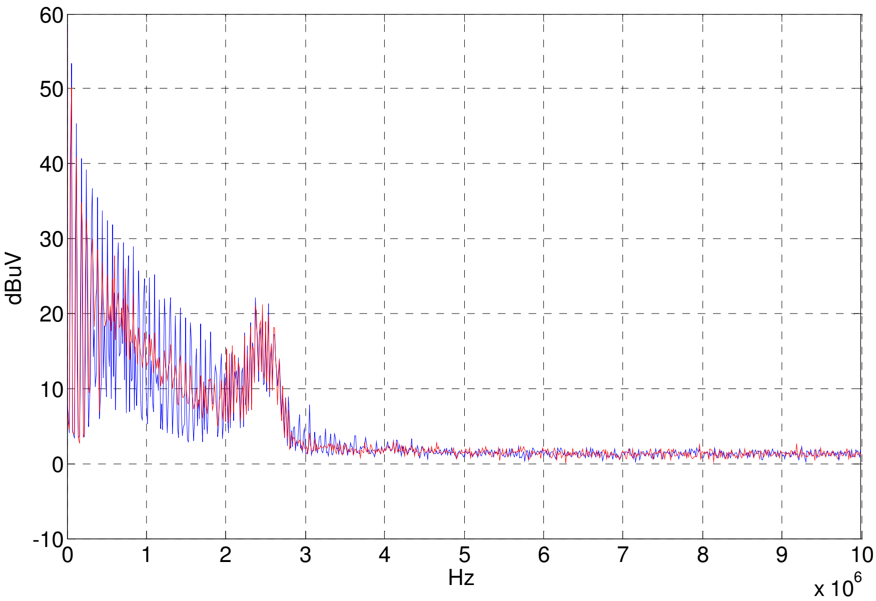

Figure 6.24 Comparison of the EMI performances with no modulation (blue line) and FM (red line) for a wide frequency range (0-10MHz).

It is evident from the experimental results illustrated in Figures 6.23 and 6.24 that very important reductions in the peak values of the frequency components are obtained. The peak amplitude after modulation is 48dBμV at the 63.75 kHz and 38dBμV at the 131.25 kHz. Figure 6.24 shows the reduction of up to 10dBμV in the following frequency range. The peaks at the certain frequencies are spread to the spectrum by generating components around these frequencies but having much lower amplitude.

For an FM signal, the frequency deviation is directly proportional to the amplitude of the applied modulating signal. Hence increasing the amplitude of the modulating signal increases the deviation. In other words, the modulation index increases as the deviation increases. Figure 6.25 shows the effect of the modulation index on the EMI emission spectrum.

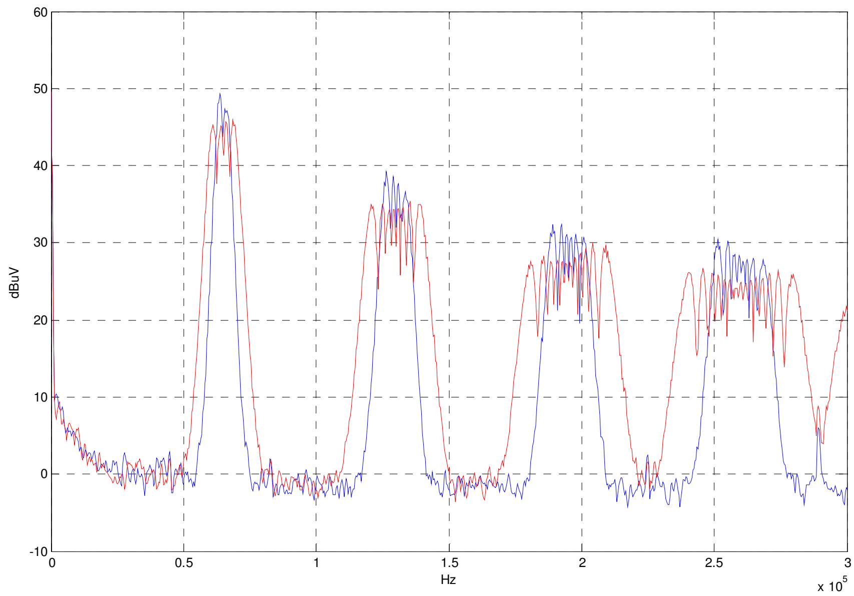

Figure 6.25 EMI spectra with different parameter of triangular modulating signal. Red line: f_m=800Hz, A_m=2$V_{p\text{-}p;}$ blue line: f_m=800Hz, A_m=1$V_{p\text{-}p}$.

Conducted EMI measurements in Figure 6.25 are taken at the constant f_m frequency by varying the amplitude of the modulating signal. It indicates that amplitude suppression is dependent with the value of modulation index and higher values give better results.

In order to see the effect of the frequency, f_m, of the modulating signal, on the conducted EMI spectrum, the Figure 6.26 is taken at the fixed amplitude of the modulating signal by increasing its frequency.

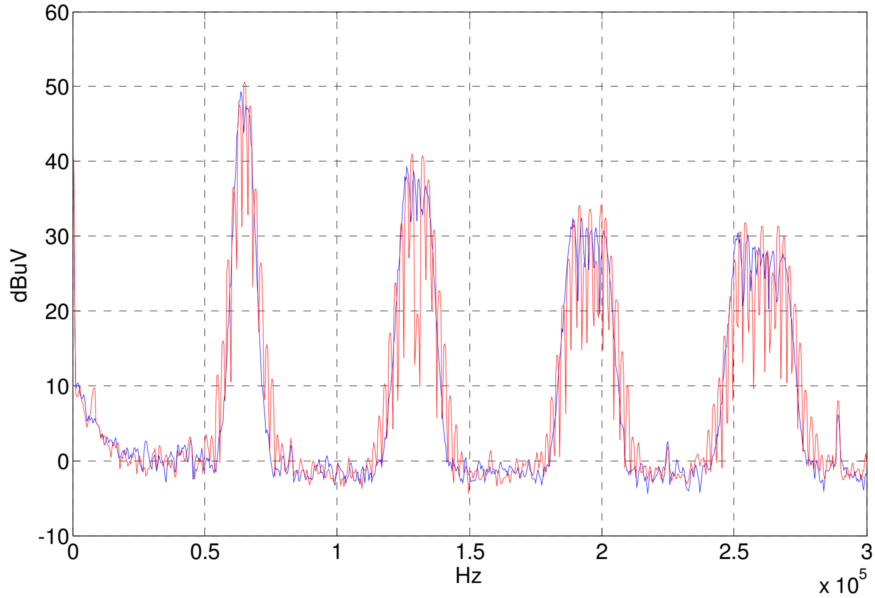

Figure 6.26 EMI spectra with different parameter of triangular modulating signal. Red line: f_m=2kHz, A_m=1V_{p-p}; blue line: f_m=800Hz, A_m=1V_{p-p}.

Figure 6.26 illustrates that the amplitude reduction caused by spread spectrum decreases while f_m increases. In other words, while the value of β decreases less reduction is obtained on the EMI emission amplitudes.

From the previous figures, it is concluded that selecting high values of frequency deviation helps decreasing the amplitude of low order harmonics. But this can produce overlapping at higher frequencies which reduces the benefits of the spread spectrum technique. Figure 6.27 shows the overlapping effect of the FM technique. Also it is seen from this figure that the amplitude of the peaks increases where the overlap occurs. The order of the harmonic at which overlap begins can be expressed by using bandwidth equation given in Chapter 4. So in order not to allow an overlap the below condition must be satisfied.

$$nf_c + \frac{B_n}{2} < (n+1)f_c - \frac{B_{n+1}}{2} \tag{6.15}$$

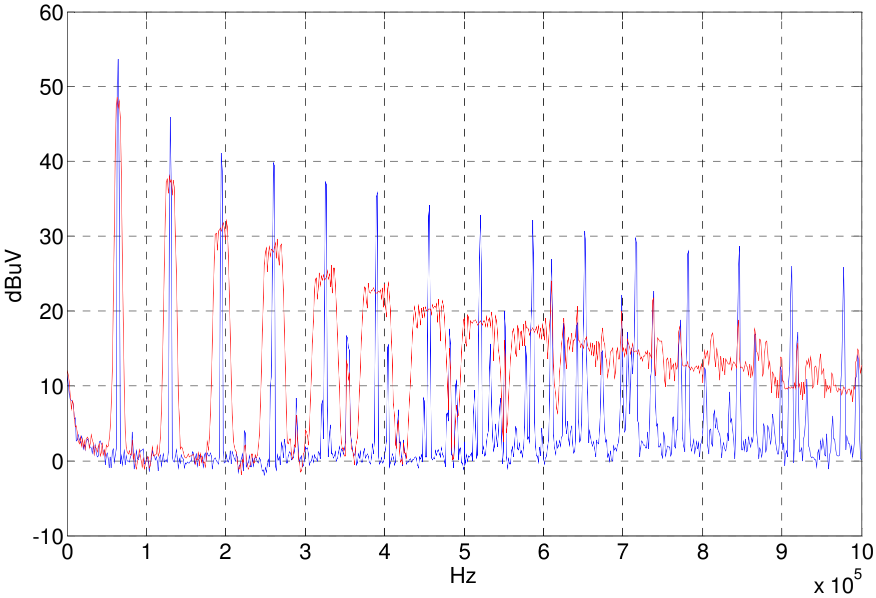

Figure 6.27 Overlap effect on the frequency spectrum. Blue line: no modulation, red line: triangular modulation with f_m=800Hz A_m=1V_{p-p}.

The number of harmonic at which overlap occurs is 8 as seen in Figure 6.27. So the frequency deviation is found nearly as 3.8kHz by using the Equation (4.57). The 1V_{p-p} triangular modulation creates 3.8kHz frequency deviation. Hence in order not to see the overlapping at the lower frequencies, the amplitude of the modulating signal should be adjusted lower than 1V_{p-p}.

Comparative measurements of conducted EMI noises obtained using triangular and sinusoidal modulating signals are given in Figure 6.28. The modulation that uses triangular modulating signal provides more flat and lower amplitudes on the EMI spectrum than the modulation making by the use of sinusoidal modulating signal. The peaks located around the bandwidth limits of the spectrum after the sinusoidal modulation can be seen in Figure 6.28.

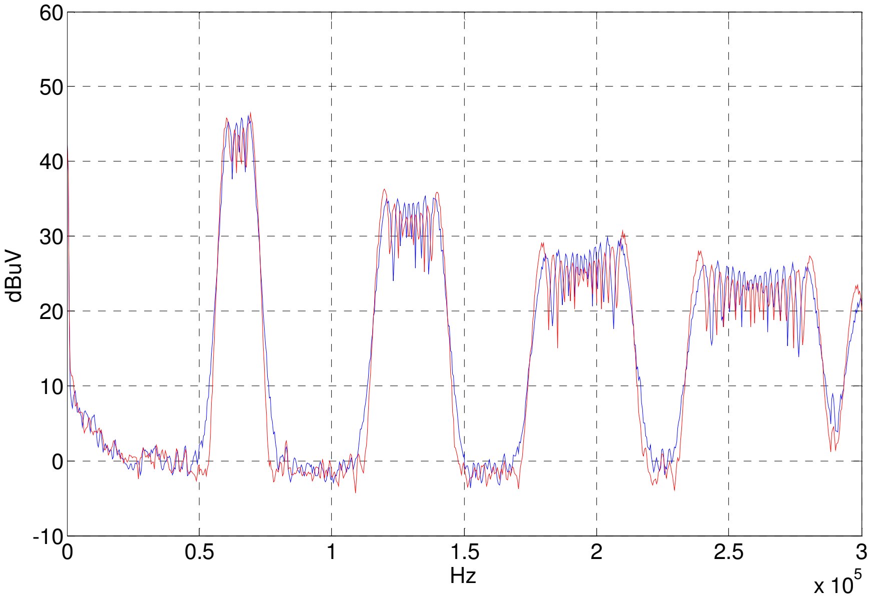

Figure 6.28 Comparison of triangular modulating (blue line, f_m=800Hz and A_m=2V$_{p\text{-}p}$) and sinusoidal modulating signal (red line, f_m=800Hz and A_m=2V$_{p\text{-}p}$).

Figure 6.29 shows the effect of the resolution bandwidth (RBW) of the spectrum analyzer on the EMI measurements.

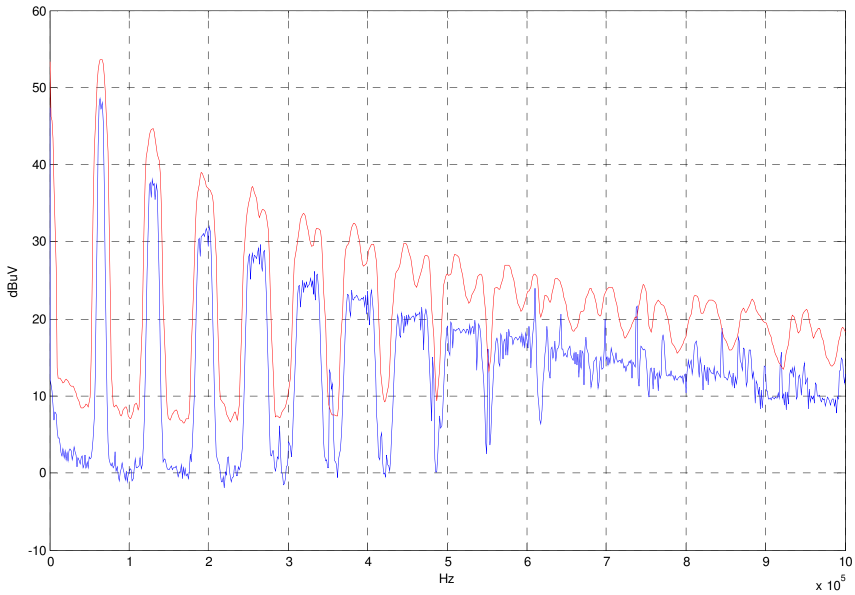

Figure 6.29 Comparison of conducted EMI spectrums taken with different RBW values. Red line: RBW =10kHz, blue line: RBW=1kHz.

RBW is responsible for giving different measured values with same parameters of the modulation. The larger RBW gives higher amplitudes, because more side band frequencies exist in the RBW by adding their amplitudes.

CHAPTER SEVEN
CONCLUSION

7.1 Concluding Remarks and Future Work

EMI is one of the most important problems in SMPS. Since converters emit EMI noise, their design needs more attention at all phases of the development of the systems to comply with the EMC standards used in the regulation of the products. The details of EMI and EMC concepts are given in this thesis. Practical design techniques that are used to decrease the effects of EMI noises in SMPS are mentioned. Flyback converter is analyzed, and sources, causes of conducted emissions are pointed out. The primary current waveform causes primarily DM conducted emission currents to circulate between the supply and the converter input. The drain voltage, diode voltage and secondary current waveforms are mainly responsible for the generation of CM conducted emission currents.

In order to reduce the EMI noise in flyback converters, FM technique was analyzed as an alternative switching technique. This technique spreads the noise energy in the spectrum of the conducted emission. Some conclusions are extracted from the theoretical analysis. Because square wave can be split into a series of sinusoidal waves, the theoretical analysis of FM technique that is applied to PWM signal for controlling the converter is firstly considered for the modulation of a sinusoidal waveform.

The most comprehensive case of FM modulated (variable duty cycle) PWM signal, which is the case in realty, is also considered. The frequency spectrum of an FM modulated PWM signal is derived using Fourier analysis.

After modulation, a single harmonic spread into an amount of side band harmonics with amplitudes smaller than the non modulated harmonic and separated by a modulating frequency. Amplitudes of the side band harmonics changes depending with the profile of the modulating signal. Triangular modulation profile produces nearly flat side band harmonics spectrum compared with the sinusoidal modulating profile. For both modulation profiles, it is observed that amplitude reduction of side band harmonics in spectrum only dependent with the modulation index. Parameters that affect the modulation index are the frequency deviation and modulating signal frequency. From the comparison of the two different modulating signals, triangular profile is the most suitable for the designed flyback converter.

Two experimental circuits, on which the FM technique is applied, are built. For the AC-DC flyback converter, the conducted EMI compliance tests are made according to the standard of EN55013. For DC-DC converter built with discrete components, the EMI noises are measured through a designed LISN by a spectrum analyzer. The effects of the modulation parameters are also observed in these applications. It can be concluded from the measurements that conducted EMI of switching power supply can be reduced by modulation of PWM switching signal. The results that are taken after modulation for both converters shows that there are nearly 10dBμV of attenuation on the peak values. The effects of the FM technique decrease ay higher frequencies.

The tests repeated with different frequency of modulating signal and frequency deviation values showed that while the frequency deviation is constant, decreasing the f_m frequency decrease the amplitude of the side band harmonics values. It was also observed that while the f_m frequency is constant, increasing the frequency deviation decrease the amplitude of the side band harmonics values.

As the modulation index increases the attenuation increases. But in the applications, overlaps are observed at high frequencies as it is expected. Modulation index with the frequency deviation and modulation ratio are responsible for the overlap at higher orders. Since the bandwidth of the sideband harmonic grow after the FM. Overlap causes lower attenuation than expected.

Using higher modulating signal frequency may affect the operation of the flyback converter. So, for proper modulating frequency, modulation index value must be selected considering the operation of the converter. The parameters of the modulation process must be decided carefully in order to have effective EMI reduction and EMI test result.

From measured values it was observed that there was no influence of the modulation on the output voltage and efficiency of the converter.

In terms of conducted EMI suppression, this study demonstrates that FM switching is better than the fixed frequency switching and it might be applied to the other power converters taking into account their operation principle.

The FM technique in this thesis uses a periodic function as the modulating signal. It is either a sinusoidal waveform or a triangular one. Other periodic functions can also be tried as the modulating signal. Also, some non-periodic waveforms such as random and chaotic signals can also be used as the modulating signal.

In this thesis, the effect of the FM technique on the EMI performance of the SMPS is considered only. The cleanness of the output voltage is also an important issue in SMPS. Therefore, the effect of the implemented spread spectrum FM technique on the output voltage is an open subject.

EMI consists of conducted and radiated emissions. We only consider the mitigation of the conducted emission noises from the SMPS. The reduction techniques for the radiated emission might also be studied.

REFERENCES

Akpınar, E., Lecture Notes. *DC-DC converters.* Dokuz Eylül University,Turkey.

Antonini, G., Cristina, S., & Orlandi, A.(1996). EMC characterization of SMPS devices: circuit and radiated emissions model. *IEEE Transactions on Electromagnetic Compatibility, 38* (3), 300-309.

Balcells, J., Gonzalez, D., Gago, J., Santolaria, A., Le Bunetel, J.C., Magnon, D., & Brehaut, S. (2005). Frequency modulation techniques for EMI reduction in SMPS. *European Conference on Power Electronics and Applications*, 8-10.

Bera, R., Bera, J., Sen, A.K., & Dasgupta, P. R. (1999). Reduction of EMI from SMPS (switched mode power supplies) by resonance technique and its utilities in industrial process control instruments. *Proceedings of the International Conference on Electromagnetic Interference and Compatibility,* 445-448.

Boys, J. T. (1993). Theoretical spectra for narrow-band random PWM waveforms. *Proc. Inst. Electr. Eng., B*, *140* (6), 393–400.

Brown, M. (1990). *Practical switching power supply design*. California: Academic Press.

Carlson, A.B., Crilly P.B., & Rutledge, J.C. (2002). *Communication Systems*. New York: McGraw-Hill Education Publisher.

Carson, J.R. (1922). Notes on the theory of modulation. *Proc. IRE, 10* (1), 57-54.

Chen.,W., & Qian., Z. (2004). A Novel and simple approach to suppress common mode EM1 in power converters. *26th Annual International Telecommunications Energy Conference,* 589-592.

Chung, H., Hui, S. Y. R., & Tse, K. K. (1998). Reduction of power converter EMI emission using soft-switching technique. *IEEE Transactions on Electromagnetic Compatibility, 40* (3), 282-287.

Çadirci, I., Saka,B., & Eristiren, Y. (2005). Practical EMI-filter-design procedure for high-power high-frequency SMPS according to MIL-STD 461. *Electric Power Applications, IEE Proceedings, 152* (4), 775-782.

Feng, B., Zhong-Xia, N., & Dong-Fang, Z. (2006). Modeling and simulation of radiated emissions in switched mode power supply. *IEEE International Symposium on Industrial Electronics, 2,* 903-907.

Haykin, S. (2000).*Communication systems.* (4th ed.). Newyork, USA: John Wiley and Sons.

Ham, N.J., Hammerton, C.J., & Sharples, D. (1994). *Power semiconductor applications* (103-239). Philips Semiconductor.

Hang-Seok, C. (2003). Transformer design consideration for off-line flyback converters using FPS. *Application Note AN4140.*Fairchild Semiconductor Corporation.

Hang-Seok, C. (2004). Design consideration for battery charger using green mode FPS. *Application Note AN4138.* Fairchild Semiconductor Corporation.

Holmes, G.D., & Lipo, T.A. (2003). *Pulse width modulation for power converters.* Hoboken, NJ: Wiley Interscience.

Kaboli, S., & Mahdavi, J. (2007). Application of random PWM technique for reducing the conducted electromagnetic emissions in active filters. *IEEE Transactions on Industrial Electronics,54*, (4), 2333-2343.

Katrai, C., & Arcus, C. (1998). EMI reduction techniques. *Application notes* (59-64). California: Pericom Semiconductor Corporation.

Katzir, L., & Singer, S. (2006). Reduction of common-mode electromagnetic interference in isolated converters using negative feedback. *2006 IEEE 24th Convention of Electrical and Electronics Engineers in Israel,* 180-183.

Kaewchai, J., Khangern, W., & Nitta, S. (2002). Controlling conducted EMI emission on a buck-boost converter using gate controlled circuit. *3rd International Symposium on Electromagnetic Compatibility, Beijing (China)*, 541-544.

Kchikach, M., WU Xin, Qian, Z.M., & Pang, M. X. (2001). Study of the effectiveness of anti-phase technique for common mode noise suppression. *Journal of Zhejiang University, 2* (4), 401-405.

Lecture Notes. *Flyback type switched mode power supply.* Indian Institute of Technology (IIT), Kharagpur.

Lee, Y.S. (1993). *Computer-aided analysis and design of switch-mode power supplies*. New York: Marcel-Dekker.

Mweene, H. L. (2006). How to ease EMI compliance in power converters. *National Semiconductor, India.*

Montrose, I. M., & Nakauchi, E. M. (2004). *Testing for EMC compliance cpproaches and techniques.* Hoboken, NJ: Wiley Interscience.

McLyman, C. T. (1988) *Transformer and inductor design handbook* (2nd ed). New York: Marcel Dekker.

Nagrial, M. H., & Hellany, A. (2001). Radiated and conducted EMI emissions in switch mode power supplies (SMPS): sources, causes and predictions. *Multi Topic Conference, IEEE INMIC 2001,* 54-61.

Ott, H.W., (1988). *Noise reduction techniques in electronic system.* (2^{nd} ed.) Newyork: John Wiley and Sons.

Paramesh, J., & Von Jouanne, A. (2001). Use of sigma-delta modulation to control EMI from switch-mode power supplies. *IEEE Transactions on Industrial Electronics, 48* (1), 111-117.

Patel, H.K. (2008). Flyback power supply EMI signature and suppression techniques. *Joint International Conference on Power System Technology and IEEE Power India Conference,* 1-6.

Power Integraions (2005). Power supply design techniques for EMI and safety. *Application note An-15*. Power Integration,Inc.

See, K. Y., & Deng, J. (2003). Measurement of noise source impedance of SMPS using a two probes approach. *IEEE Transactions on Power Electronics, 19*, (4), 862-868.

Sheng, Y., & Qian, Z.(2002). Dynamic nodes potential balance suppression technique for common mode EM in power electronics. *EEE EMC 2002*, 40-43.

Son, Y. C., & Seung-Ki, S. (2006). Generalization of active filters for EMI reduction and harmonics compensation. *IEEE Transactions on Industry Applications, 42* (2), 545-551.

ST Microelectronics (2008). L6566B Multi-mode controller for SMPS. *STMicroelectronics*.

Tran, E. (1999). Environment/EMC/EMI. *18-849b Dependable Embedded Systems, Carnegie Mellon University.*

Williams, T., (1996). *EMC for product designer.* (2nd ed.), UK: Newnes.